

AD-A210 252

STIC FILE COPY

DTIC

JUN 29 1989

2

UNCLASSIFIED


SECURITY CLASSIFICATION OF THIS PAGE

REPORT DOCUMENTATION PAGE

1. REPORT SECURITY CLASSIFICATION Unclassified		10. RESTRICTION MARKINGS	
2. SECURITY CLASSIFICATION AUTHORITY		3. DISTRIBUTION STATEMENT Approved for public release, distribution unlimited	
3. DECLASSIFICATION/DOWNGRADING SCHEDULE		5. MONITORING ORGANIZATION REPORT NUMBER(S) AFOSR-TR. 89-0780	
4. PERFORMING ORGANIZATION REPORT NUMBER(S)		7a. NAME OF MONITORING ORGANIZATION Division of Aerospace Sciences AFOSR	
6a. NAME OF PERFORMING ORGANIZATION Department of Mechanical Eng. Florida State University		7b. ADDRESS (City, State and ZIP Code) Bldg 410 Bolling AFB, Washington, D.C 20332	
6b. ADDRESS (City, State and ZIP Code) Tallahassee, Florida 32306		8a. NAME OF FUNDING/SPONSORING ORGANIZATION AFOSR/NA Bolling AFB, DC 20332	
8b. ADDRESS (City, State and ZIP Code) AFOSR/NA Bolling AFB, DC 20332		9. PROCUREMENT INSTRUMENT IDENTIFICATION NUMBER AFOSR-86-0243	
11. TITLE (Include Security Classification) Basic Studies of the Unsteady Flow Past High Angle of Attack Airfoils		10. SOURCE OF FUNDING NOS.	
12. PERSONAL AUTHOR(S) Krothapalli, Anjaneyulu; Lourenco, Luiz; and Van Dommelen, Leon		PROGRAM ELEMENT NO 61102F	PROJECT NO 2307
13a. TYPE OF REPORT Final		TASK NO 43	WORK UNIT NO
13b. TIME COVERED FROM 10/1/86. to 10/30/88		14. DATE OF REPORT (Yr, Mo, Day) May 15, 1989	
15. PAGE COUNT 132		16. SUPPLEMENTARY NOTATION	
17. COSATI CODES		18. SUBJECT TERMS (Continue on reverse if necessary and identify by block number)	
FIELD	GROUP	Unsteady Flows; High Angle of Attack Airfoils; Particle Image Velocimetry; Vortex Calculations	
19. ABSTRACT (Continue on reverse if necessary and identify by block number)			
<p>An experimental and numerical simulations have been carried out to study the unsteady flow past an impulsively started NACA 0012 airfoil at different angles of attack ($0 < \alpha < 45^\circ$). A novel experimental technique, commonly referred to as Particle Image Displacement Velocimetry (PIDV), is successfully implemented to measure the instantaneous velocity fields. The velocity field is measured with sufficient accuracy so that the distribution of vorticity can be calculated. The Unsteady separated flow fields generated by the these airfoils contain large scale vortical structures such as; a primary vortex generated at the leading edge of the airfoil with secondary vortices upstream of it; a trailing vortex, and a vortex sheet type structure. The origins and time evolution of these structures are clearly depicted by the instantaneous velocity and vorticity fields. A random-walk vortex simulations of the full Navier-Stokes equations were performed as comparison.</p>			
20. DISTRIBUTION AVAILABILITY OF ABSTRACT UNCLASSIFIED/UNLIMITED <input checked="" type="checkbox"/> SAME AS PRT <input type="checkbox"/> DT USERS <input type="checkbox"/>		21. ABSTRACT SECURITY CLASSIFICATION	
22a. NAME OF RESPONSIBLE INDIVIDUAL H. HELIN		22b. TELEPHONE NUMBER (Include Area Code) 202 767 0471	22c. OFFICE SYMBOL AFOSR/NA

TABLE OF CONTENTS

1. Introduction	1
2. Status of the Research Effort	2
3. Professional Personnel	17
4. Presentations & Seminar	18
5. Publications	19
6. Appendices	20

Accession For	
NTIS GRA&I	<input checked="" type="checkbox"/>
DTIC TAB	<input type="checkbox"/>
Unannounced	<input type="checkbox"/>
Justification	
By _____	
Distribution/	
Availability Codes	
Dist	Special
A-1	



INTRODUCTION

A research program of basic experimental and computational studies on the unsteady flow generated by a pitching airfoil was initiated in October 1986 under grant no. AFOSR-86-0243. This report is being written to describe the work carried out during the period October 1986 - October 1988. It is of interest to note that the work is being continued under a separate contract AFOSR F49620-89-C-0014.

The present study has the following objectives to the general problem of unsteady flow past a NACA 0012 airfoil undergoing large amplitude incidence variation.

1. Investigate the unsteady flow structure generated by an impulsively started airfoil from rest, at different angles of attack.
2. Investigate the transient flow characteristics of an NACA 0012 airfoil undergoing a stepwise varying angle of attack.
3. Investigate the unsteady flow structure of an accelerating NACA 0012 airfoil at different fixed angles of attack.
4. Investigate the transient flow characteristics of an accelerating airfoil undergoing a stepwise incidence variation.

In all these studies attention was directed to the basic understanding of the unsteady flow phenomena. A unique experimental technique, known as Particle Image Displacement Velocimetry, developed in our laboratory, is successfully implemented to study, in detail, the unsteady large scale vortical motions that occur in these flows. A parallel effort was devoted to study the experimentally observed features using numerical simulations. In an attempt to expand the parameter range, in consultation with AFOSR, a new larger towing tank facility has been designed and constructed.

In the following, the status of the research effort is given along with some of the most important conclusions arrived from this study. The details of various investigations are given in reports and papers, which are included here as appendices.

STATUS OF THE RESEARCH EFFORT

In the following, major conclusions on the various facets of the research program are given.

a) *Impulsively started airfoil.*

A systematic investigation has been carried out to understand the basic flow structure generated by an impulsively started NACA 0012 airfoil, of finite aspect ratio, at different angles of attack, and at a fixed Reynolds number of 1400.

A novel experimental technique known as "Particle Image Displacement Velocimetry" was used to measure the instantaneous two dimensional velocity field. The velocity field was measured with sufficient accuracy and spatial resolution that the vorticity field and pressure field can be computed accurately, a unique capability of the technique. The detailed description of this technique is given in the Appendix I.

A parallel computational study was conducted to augment the above mentioned experimental study. In this study, a new algorithm was developed to solve the Navier-Stokes equations using the discrete vortex method. The new fast velocity summation algorithm enables the flow to be computed with much more resolution than previously possible in vortex methods. The details of the algorithm is given in Appendix II.

The main features of the unsteady large scale separated flow about an impulsively started airfoil are as follows:

The multiple exposure photographs of the flow field about the airfoil at 10° or less incidence showed that the flow is well behaved and attached to the airfoil over the period of observation. However, at large angles of attack $\alpha \geq 20^\circ$, the flow separates on the upper surface of the airfoil and generates large scale vortices. The following scenario develops in time on the upper surface of the airfoil. At the start of the airfoil, a starting vortex develops at the trailing edge and is carried away downstream of the airfoil. Concomitant with is the generation of a separation bubble at the leading edge of the airfoil. At a later time, the separation bubble grows into an isolated primary vortex with secondary vortices following behind it. This multiple vortex structure continues to grow together and move along the upper surface until it reaches the trailing edge. At this point, the primary vortex induces a vortex at the trailing edge with the sense opposite to that of the primary vortex. Finally, the primary vortex and the induced trailing edge vortex interact and generate a complex flow field. However, for finite aspect ratio airfoils or wings, a different type of flow field seems to emerge at later stages of development. The various events described above

occur at different times, depending upon the angle of attack and free stream Reynolds number.

Typical PIDV measurements of the instantaneous velocity field, at different times, for an airfoil at $\alpha = 30^\circ$ are shown in figure 1. The aspect ratio of the wing was about 3. The airfoil travels from right to left. The data is presented in the body fixed reference frame. The length of the velocity vector corresponds to its magnitude. The dimensionless time t^* is defined as $\frac{tU}{C}$, where U is the free stream velocity and C is the airfoil chord. The starting vortex (at the far right of the picture) and the initial separation bubble at the leading edge can be seen in the figure corresponding to $t^* = 0.68$. The primary vortex with secondary vortices following behind it can be seen in the figure at $t^* = 2.02$. The trailing edge vortex can be seen in the figure at $t^* = 3.02$. At $t^* > 3$, the primary vortex abruptly moves away from the upper surface leaving behind a vortex sheet type like structure. Such a behavior is attributed to the interference of tip vortices which are generated due to the finite aspect ratio of the airfoil. At later times, for example at $t^* = 4.85$, the tip vortices interact with the separated flow on the upper surface and generate a complicated three-dimensional flow field. The nature of this interaction and parameters that govern such a flow field is not yet known. The current experiments with a larger aspect ratio (10) airfoil will help us in the interpretation of these results.

Typical two-dimensional computational results from random-walk vortex simulations of the full Navier-Stokes equations are shown in figure 2. The angle of attack and the Reynolds number are the same as those in the experiment; the results of which are shown in figure 1. The stream line pattern, along with vorticity, which is represented in bit-mapped graphics as half tones are shown in the figure. Except for the effect of the finite aspect ratio of the airfoil, the stream line pattern looks very much similar to those found in figure 1. To further evaluate these results, the locus of the primary vortex as it develops in time is shown in figure 3. The computational results agree well with the experiment for $t^* \leq 2$. Beyond $t^* = 2$, it is expected that the experimental flow field was influenced by the tip vortices making it to be three-dimensional. The coefficients of lift and drag as obtained from the computations are shown in figure 4. As expected, the coefficient of lift increases with t^* up to a point where the primary vortex is attached to the upper surface. For later times, where the primary vortex leaves the upper surface, the coefficient of lift drops significantly. In order to have a proper comparisons, the experiment is being conducted at this time with a larger aspect ratio airfoil, where the flow can remain two-dimensional!

beyond $t^* > 2$.

Similar observations are also made for the airfoil at $\alpha = 20^\circ$, and the results are shown in figures 5 and 6. Figure 5 shows typical flow field measurements at four different times. The drop out regions are a result of the blockage of the laser light by the airfoil. The new optical set up explained later will avoid such regions. The various stages of the development of the separated flow, as explained above, can be seen in these instantaneous flow fields. The dynamics of these vortices and their role on the surface pressures are being investigated at this time. The corresponding computational results are shown in figure 6. From these results, it appears that the numerical simulation depicts clearly the various stages of the flow development observed in the experiment.

b) Pitching Airfoil.

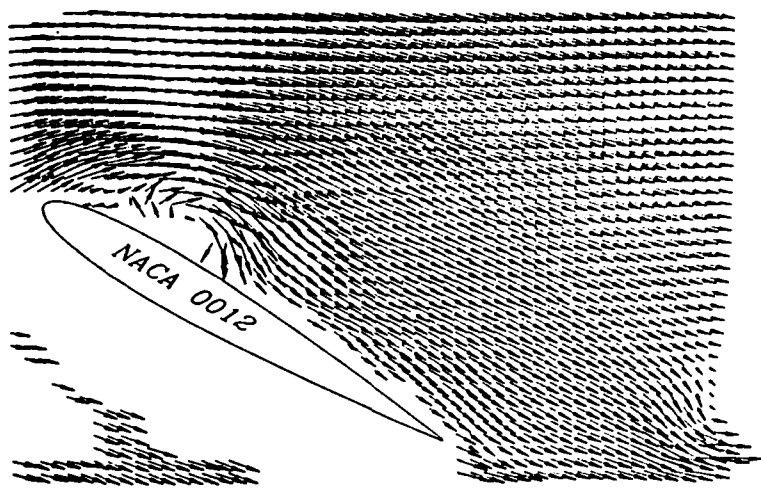
The experimental facility to investigate the transient flow characteristics of an airfoil with stepwise varying angle of attack has been built and the details are given in the next section. However, numerical simulations have been carried out on a typical case of a NACA 0012 airfoil undergoing a rapid variation in its angle of attack as shown in figure 7. In the simulation, the airfoil initially translates at zero angle of attack during a time interval $0 < t^* < 1$; in the interval $1 < t^* < 2.3$ the angle of attack increases linearly from 0° to 30° ; beyond this time the angle of attack is held fixed at 30° . The numerical procedure is summarized in appendix III. The results of this numerical simulation are shown in figure 8. The results clearly shows the various stages of the transient flow development and associated vortical flow field. These results are still being analyzed.

c) Towing Tank Facility.

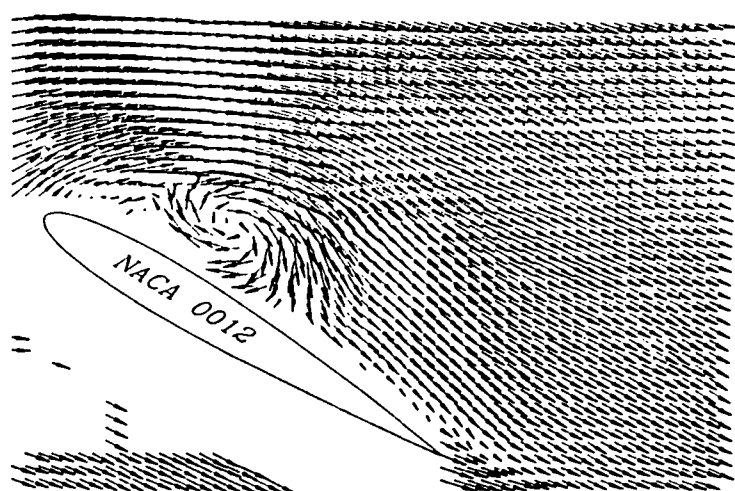
A computer controlled towing tank facility has been designed, and constructed. A schematic of the facility is shown in figure 9. The various components of the facility are indicated in the figure. The significant improvement in this facility, over other traditional towing tanks, is the ability to vary the velocity rapidly without encountering any vibration of the model. Which is accomplished by the use of "Anorail" linear motor system controlled by an intelligent axis controller with a speed range from 3mm/sec to 0.3m/sec. Impulsive or continuous airfoil pitching motion is controlled by "Klinger" stepping motor system. A new optical arrangement has been incorporated in to this facility, which has the capability of steering the laser sheet in several directions. This capability will enable us to illuminate the entire flow field around the airfoil.

The laser source and the camera are synchronously controlled by an electronic system

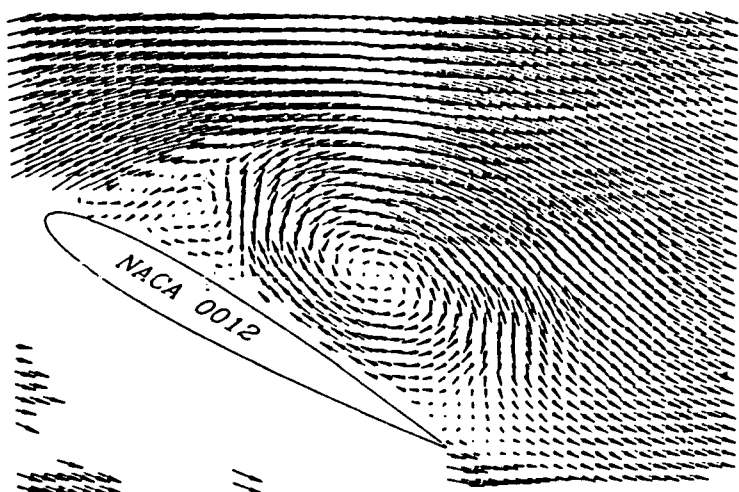
which is activated by a computer. A schematic of the arrangement is shown in figure 10. The entire operation is monitored by DEC Vax Station II computer.



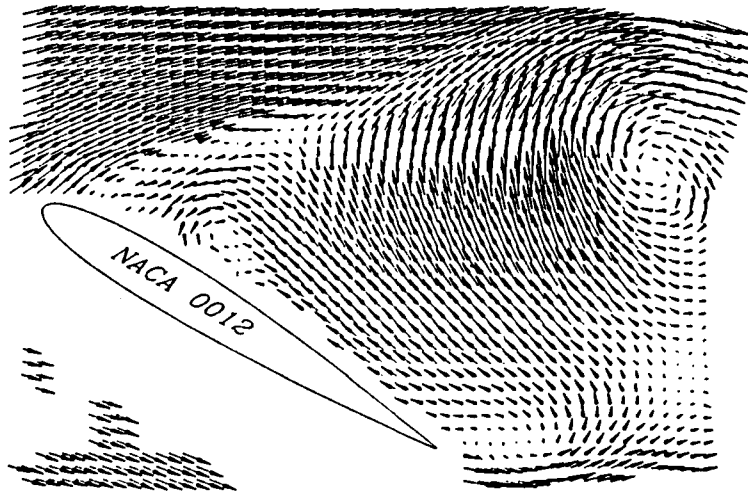
$t^* = 0.68$



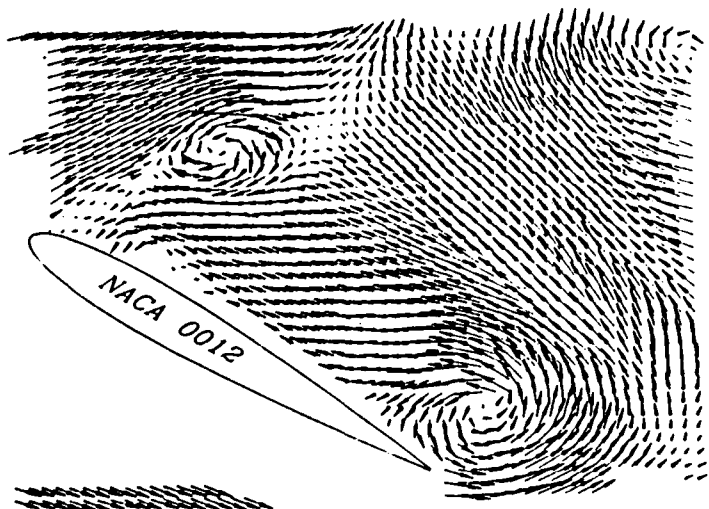
$t^* = 1.02$



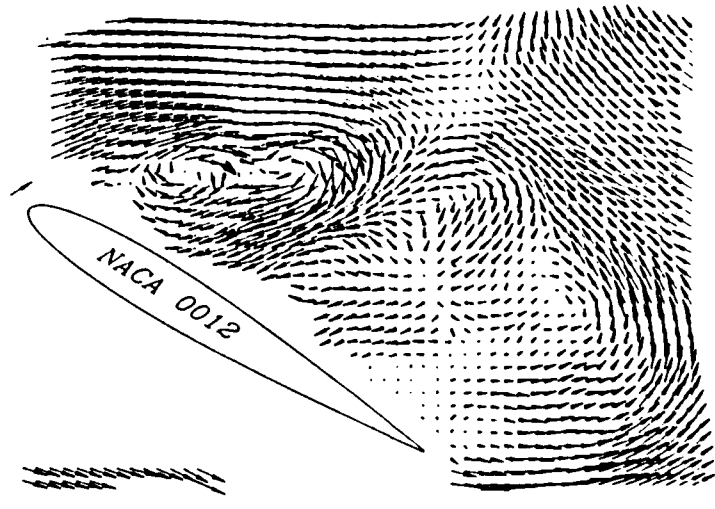
$t^* = 2.02$



$t^* = 3.02$



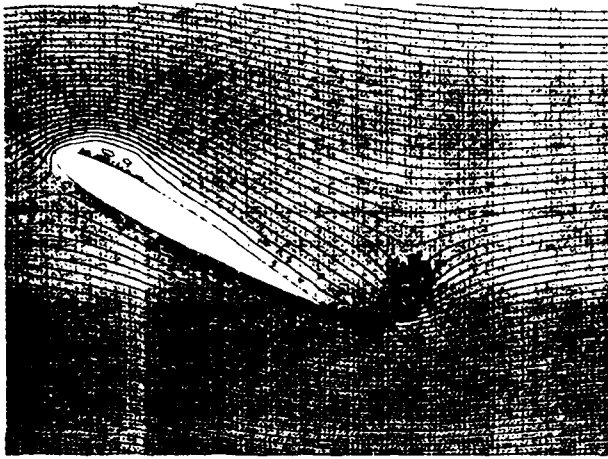
$t^* = 4.02$



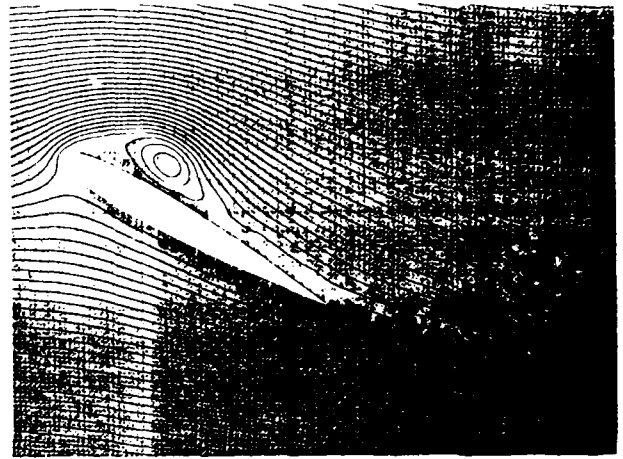
$t^* = 4.85$

Figure 1. Time evolution of the instantaneous velocity field in the central plane of the wing obtained using PIDV. $Re = 1400$. angle of attack = 30 degrees.

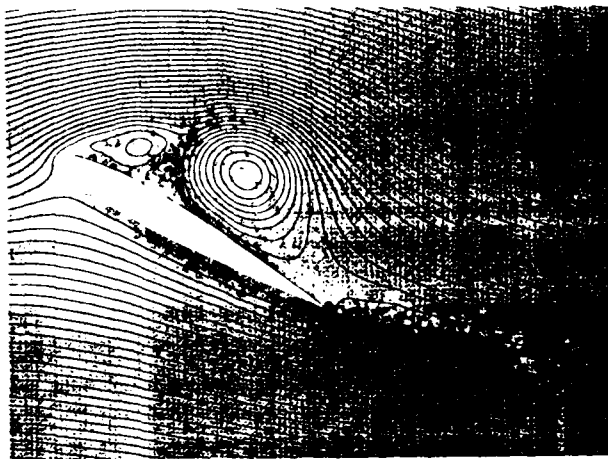
6



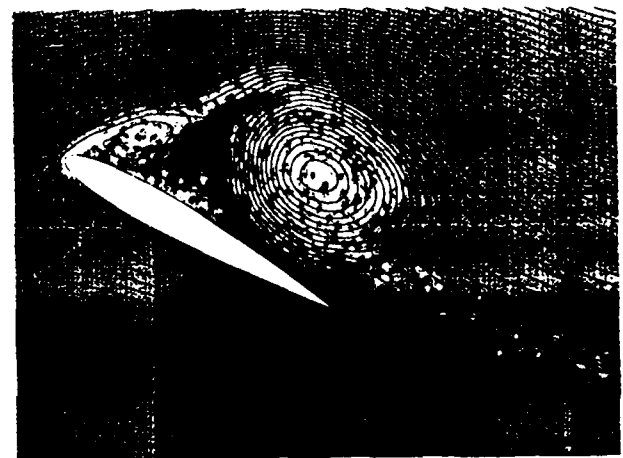
$t^* = 0.5$



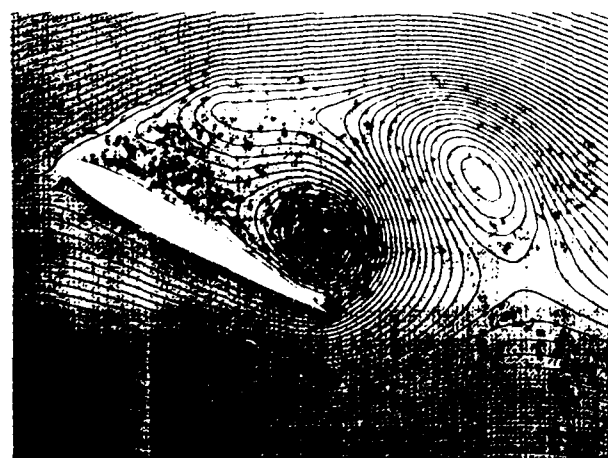
$t^* = 1.0$



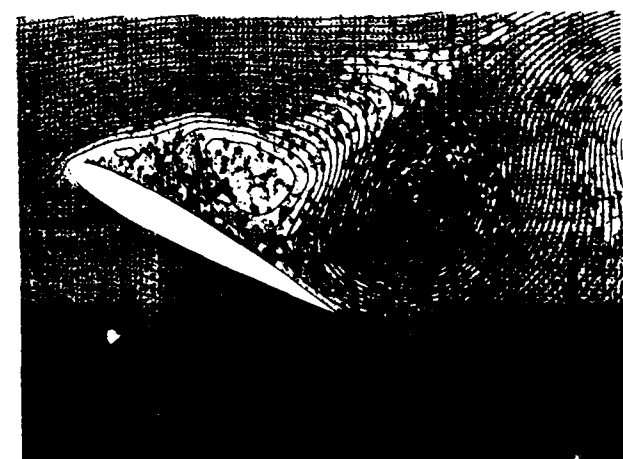
$t^* = 2.0$



$t^* = 3.0$



$t^* = 4.0$



$t^* = 5.0$

Figure 2. Two-dimensional computational results of the flow field about an NACA 0012 airfoil. $Re = 1400$.

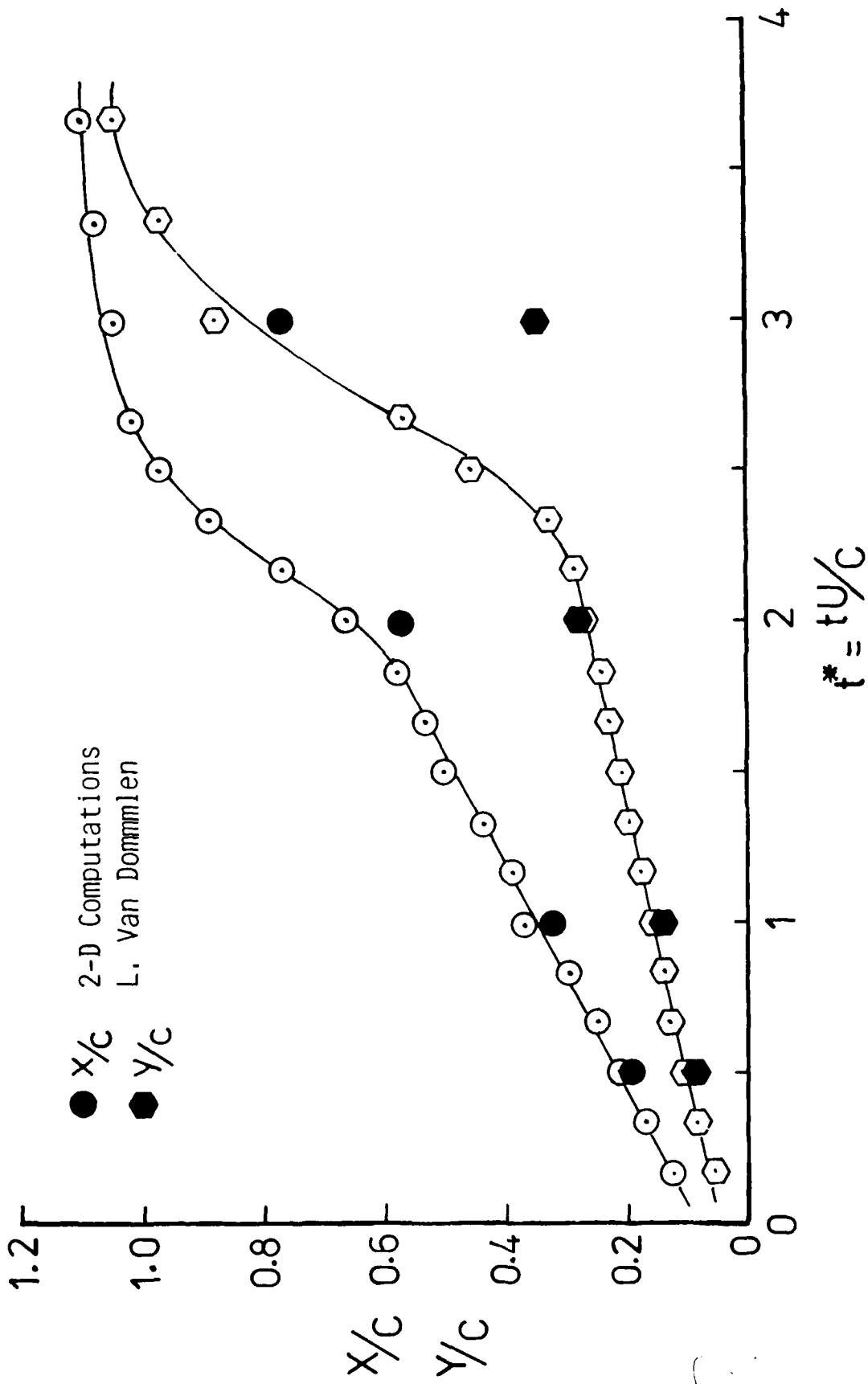


Figure 3. The variation of the primary vortex location with time.
Angle of attack ≈ 30 degrees, $Re = 1400$.

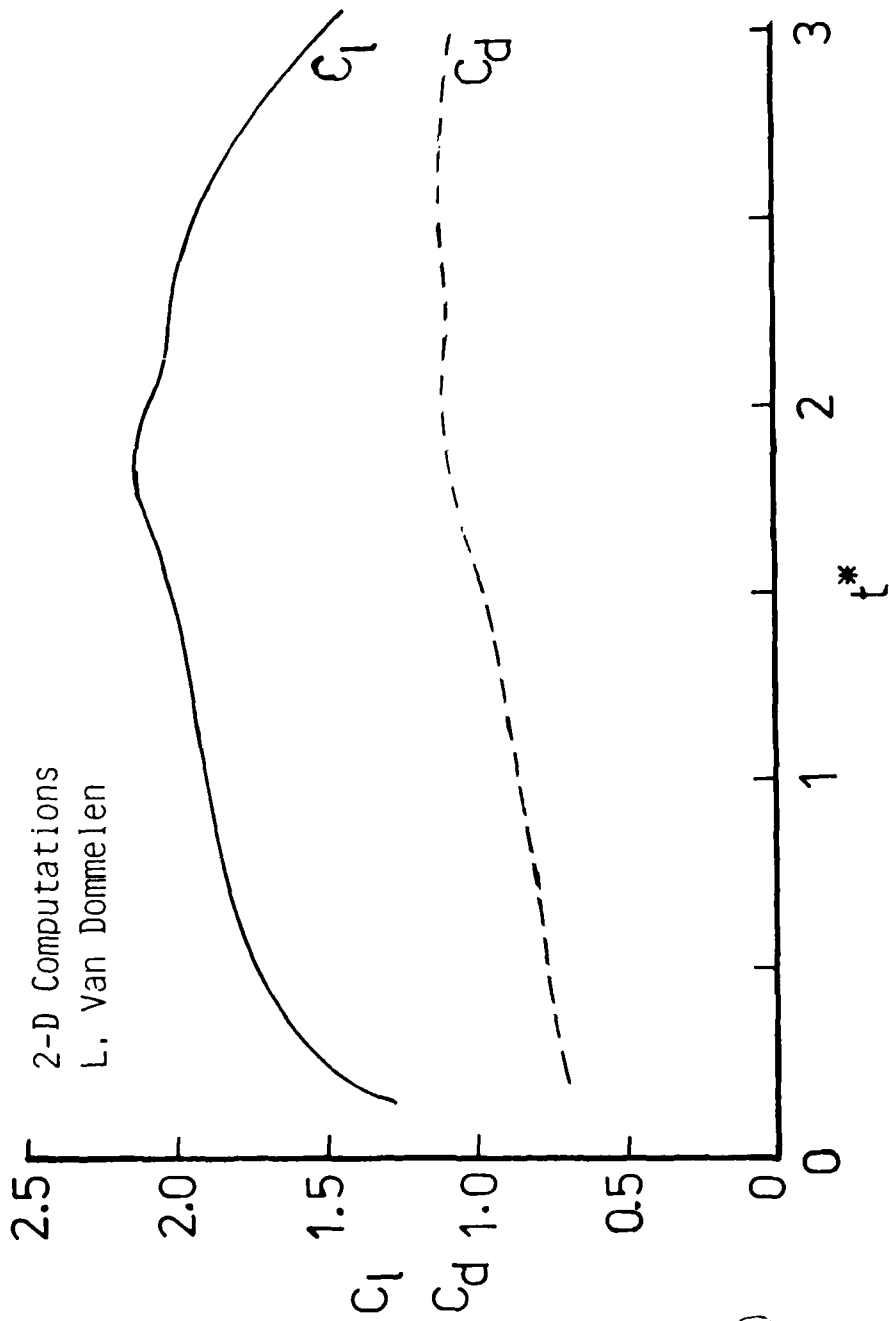


Figure 4. The variation of the computed lift and drag with time.
 C_l and C_d are nondimensional lift and drag coefficients.
 $Re = 1400$, angle of attack = 30 degrees.

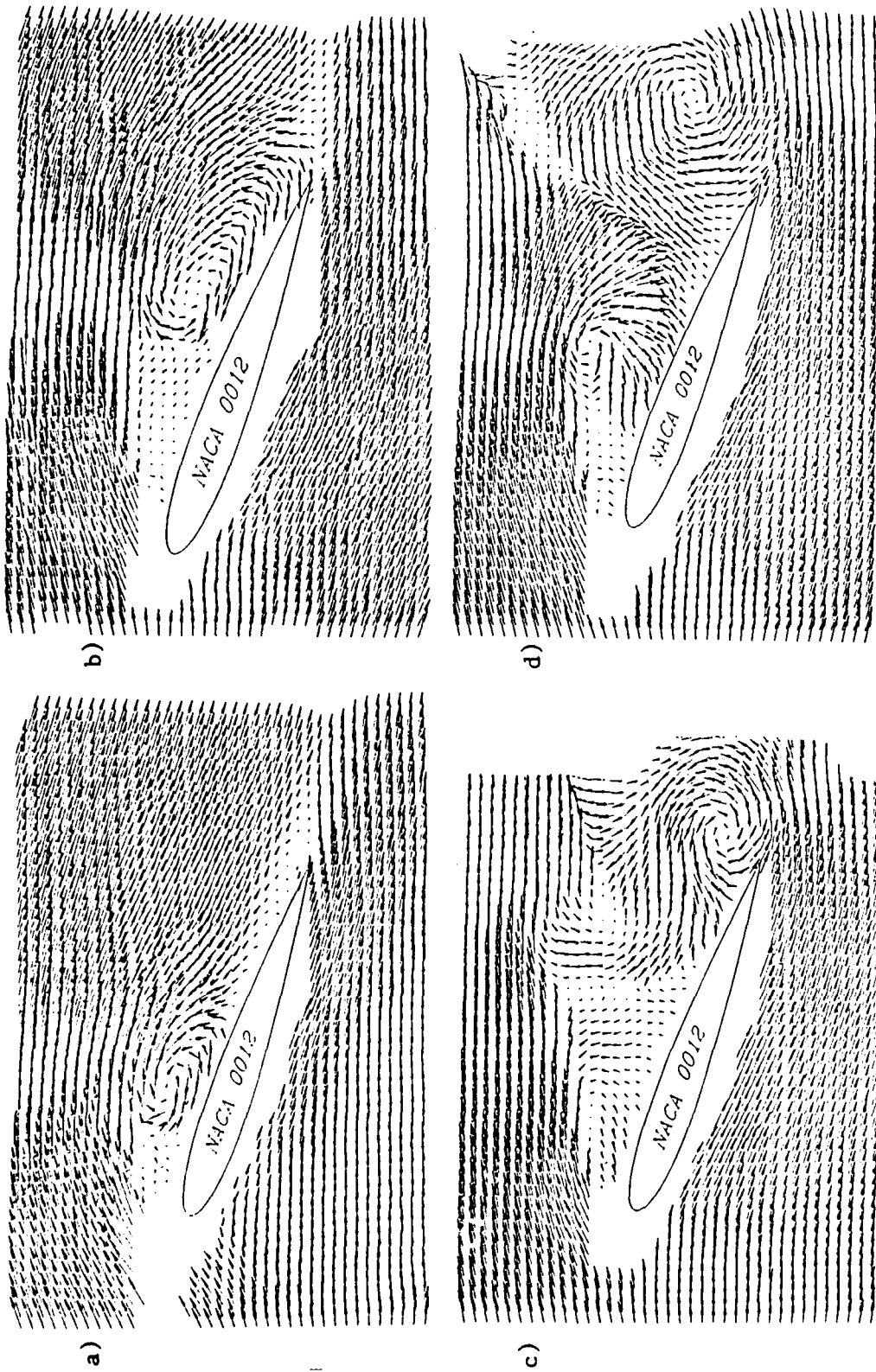


Figure 5. Instantaneous velocity fields in the central plane; $Re = 1400$; angle of attack = 20° ; a) $t^* = 1.5$; b) $t^* = 2.5$; c) $t^* = 3.5$; d) $t^* = 4.5$.

10

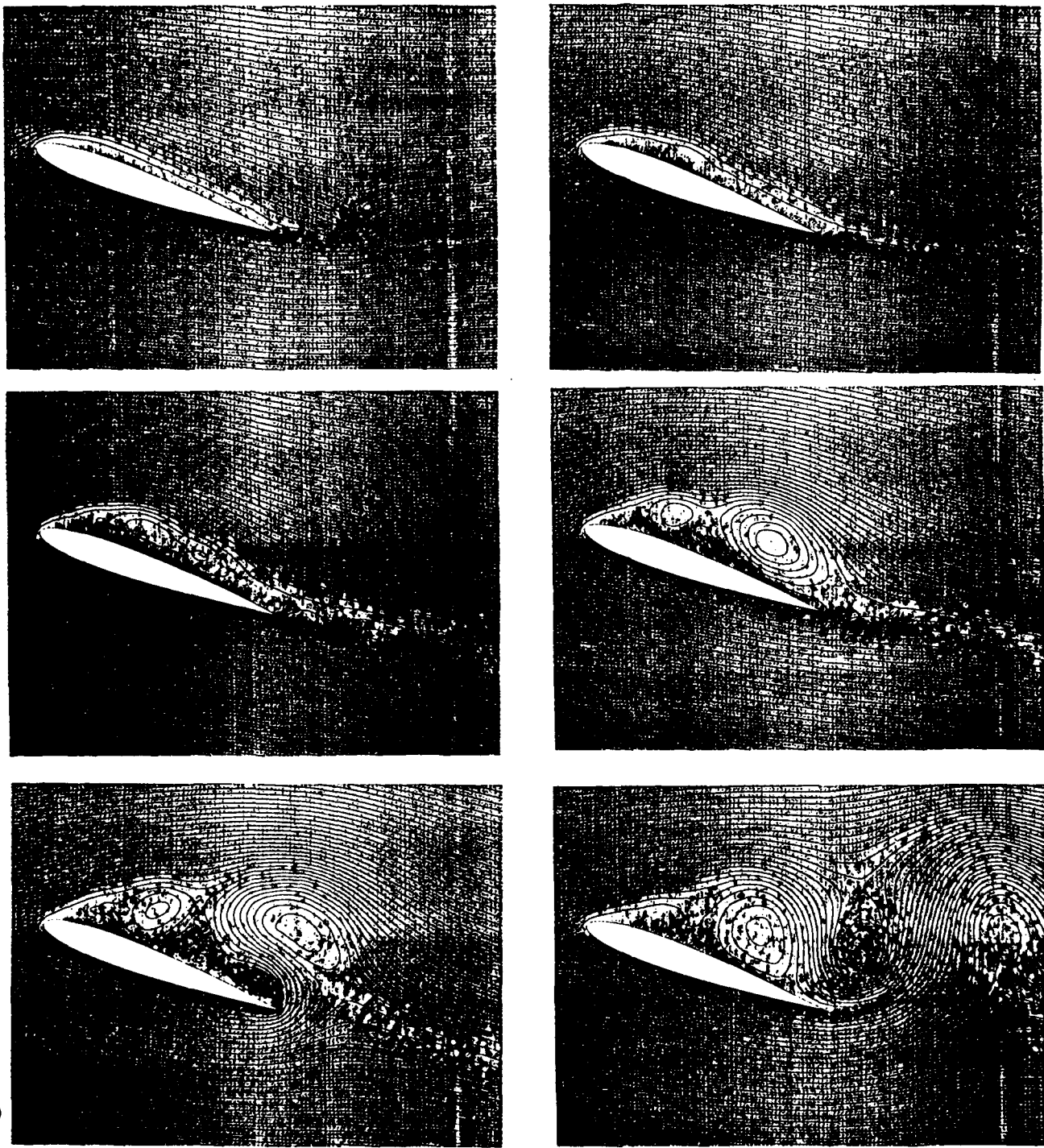


Figure 6. Numerical simulation of the flow past an impulsively started airfoil at -20° ; $Re = 1400$; a) $t^* = 0.5$; b) $t^* = 1.0$; c) $t^* = 2.0$; d) $t^* = 3.0$; e) $t^* = 4.0$; f) $t^* = 5.0$.

//

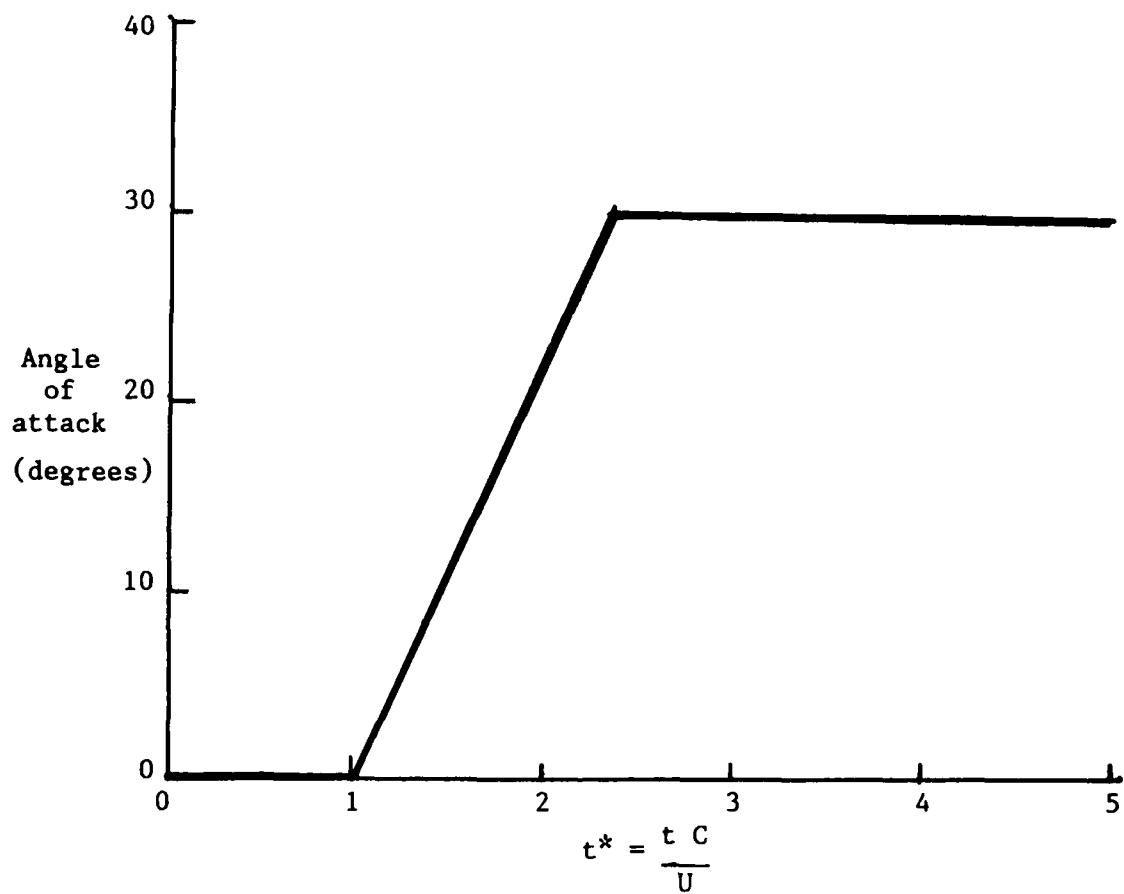


Figure 7. The variation of the angle of attack with time for the computational study.

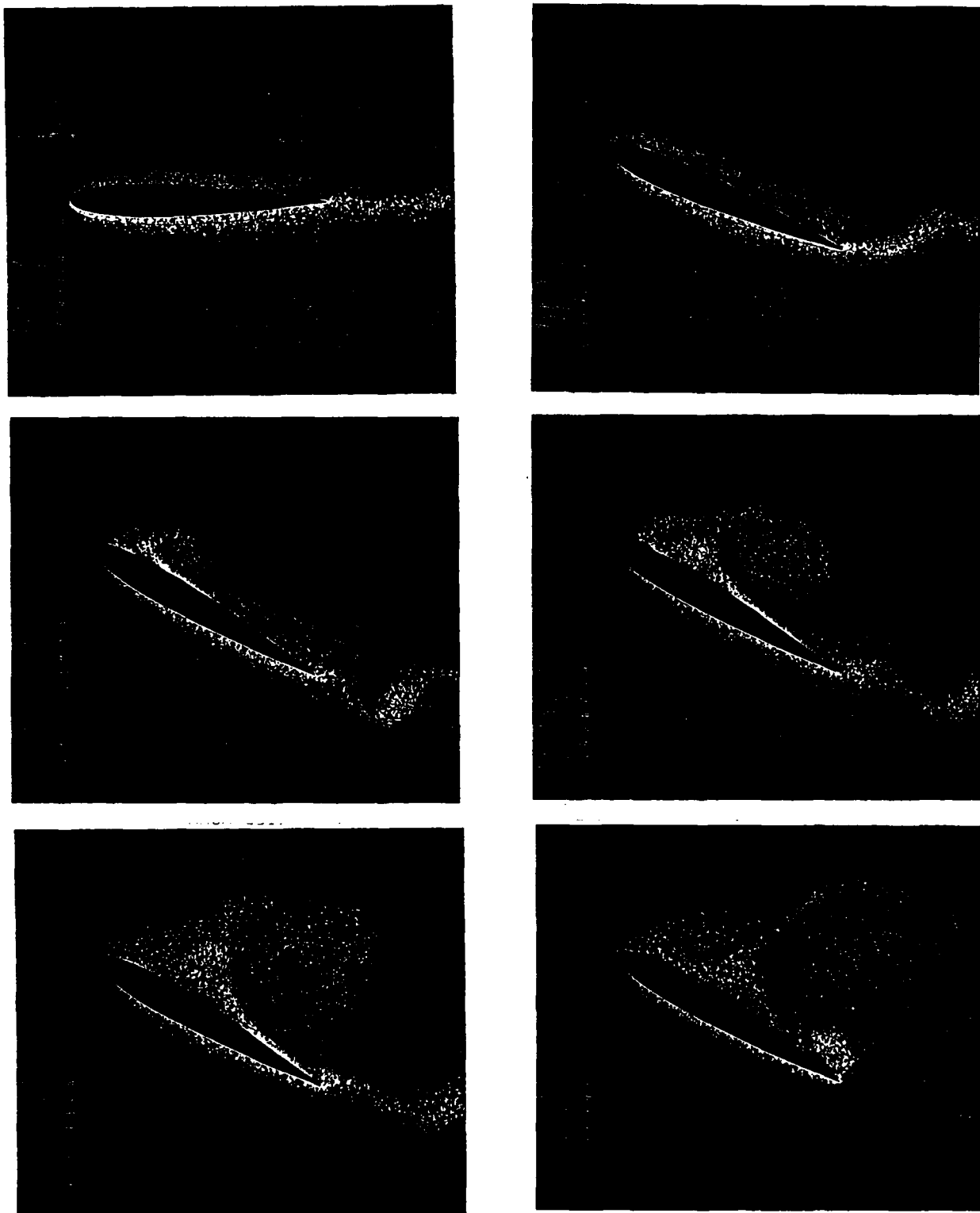
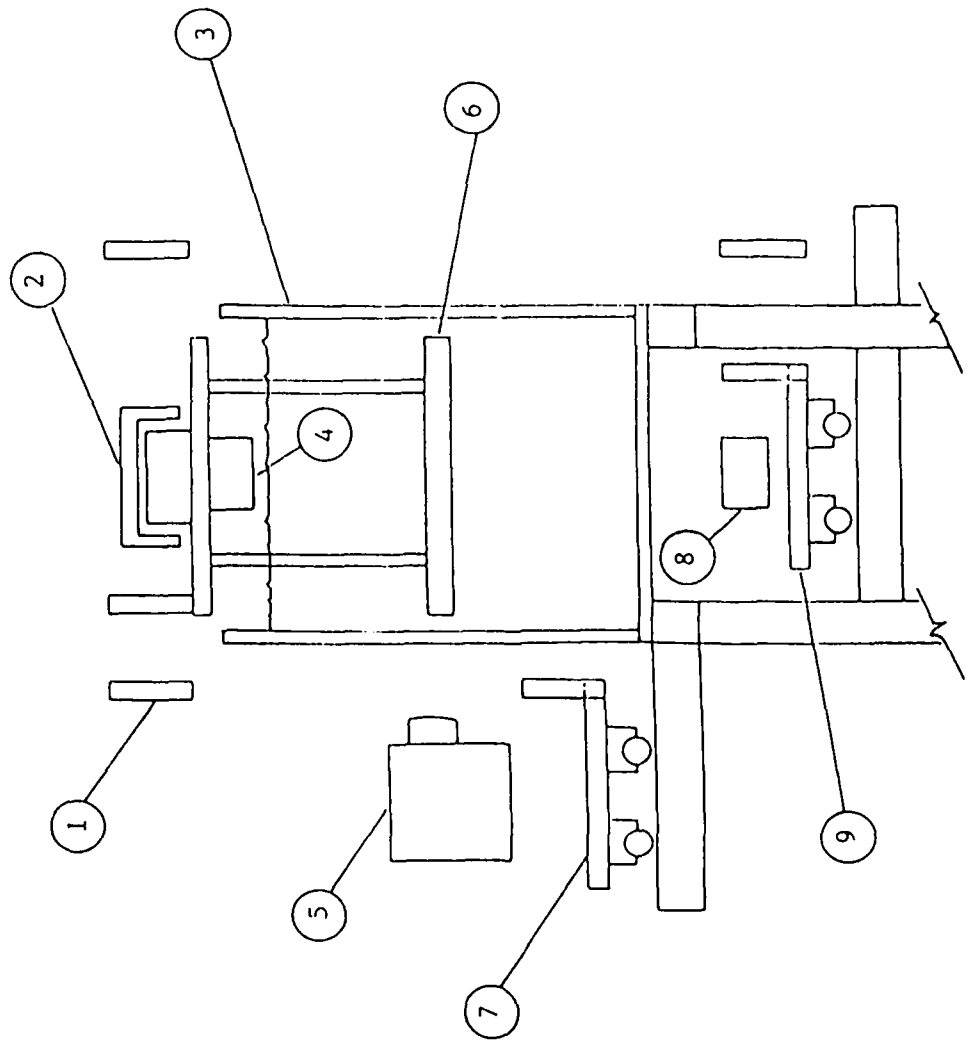


Figure 8. Time evolution of the flow past a NACA 0012 airfoil undergoing the motion shown in figure 7;
a) $t^* = 1.0$; b) $t^* = 2.0$; c) $t^* = 2.7$; d) $t^* = 3.7$; e) $t^* = 4.5$; f) $t^* = 5.0$; $Re = 1400$.



1. Gear belt pulley, 6 places
2. Linear motor
3. Tank
4. Laser mirror
5. Camera
6. Airfoil
7. Camera carriage
8. Laser mirror
9. Laser mirror carriage

(b) Front view

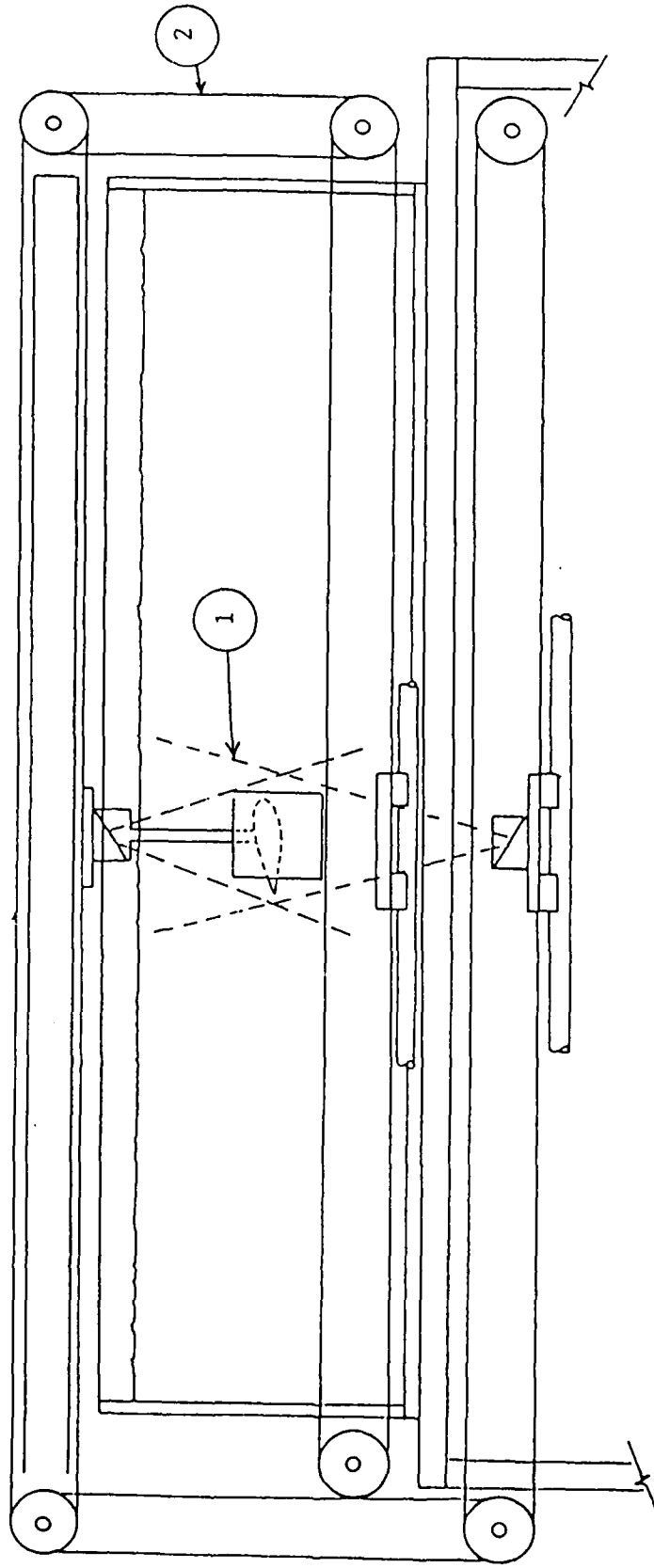
Figure 9 (Continued)

14

← 25cm →

Scale: 1 in = 25cm

- 1. Laser sheet
- 2. Gear belt



(a) Side view

Figure 9 A schematic of the towing tank arrangement

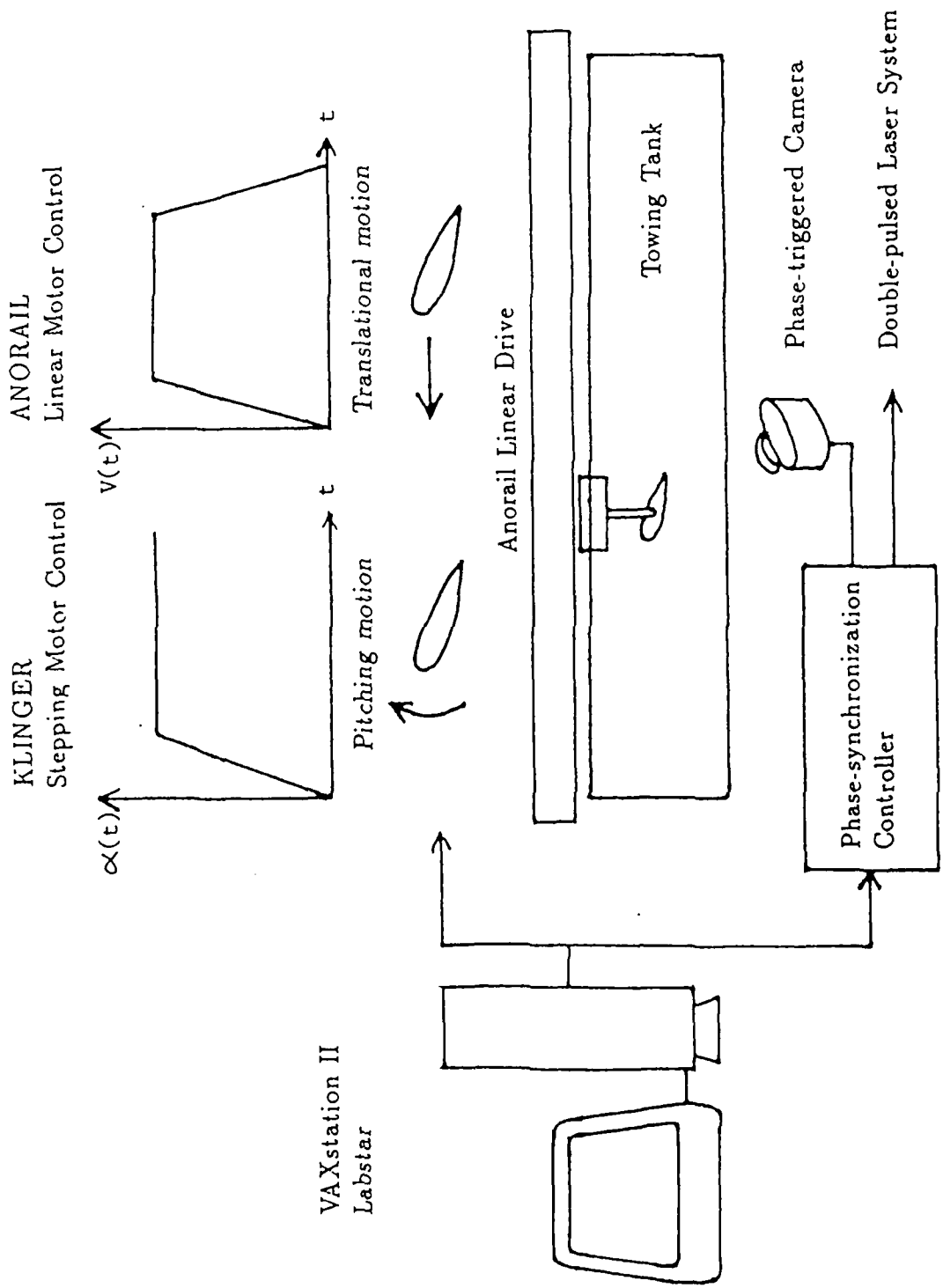


Figure 10 A schematic of the Computer-interfaced control loop

16

PROFESSIONAL PERSONNEL

1. Faculty:

- . Professor Anjaneyulu Krothapalli
- . Professor Luiz M. Lourenco
- . Professor Leon Van Dommelen

2. Post Doctoral Fellow:

- . Dr. M. S. Chandrasekhara

3. Graduate Students:

- . Mr. Ramesh Arjunji, M.S (August 1988)
- . Mr. S. P. Gogineni, M.S (June 1989)

PRESENTATIONS AND SEMINARS

1. Prof. A. Krothapalli

- . Aerospace Engineering Seminar, V.P.I and State University, July 1987.
- . Unsteady Aerodynamics Seminar, NASA Langley Research Center, July 1987.
- . Poster session, 26th Aerospace Sciences Meeting, January 1988

2. Prof. L. Lourenco

- . Aerospace Engineering Seminar, University of Southern California, October 1987.
- . ASME Winter annual Meeting (Panel Member), December 1987.
- . Lecture Series, Von Karman Institute for Fluid Dynamics, Belgium, March 1988.

3. Prof. L. Van Dommelen

- . ICOM Seminar, NASA Lewis Research Center, June 1987.
- . Applied Mathematics Seminar, Courant Institute for Mathematical Sciences, April 1988.

PUBLICATIONS

1. A. Krothapalli, and L.Lourenco., "Unsteady Separated Flows: A Novel Experimental Approach", AIAA Paper No. 87-0459, 25th Aerospace Sciences Meeting, January 1987.
2. L. Lourenco, M.S. Chandrasekhara, and A. Krothapalli, "On the Unsteady Flow Past an Impulsively Started Airfoil at High angles of Attack", ASME Applied Mechanics and Fluids Conference, June 1987, FED, Vol. 52, P. 199.
3. L. Van Dommelen, "Unsteady Separation from Lagrangian Point of View", ASME Applied Mechanics and Fluids Conference, June 1987, FED, Vol. 52, P. 81.
4. L. Van Dommelen, and E. A. Rundensteiner, "Fast Solutions of the Two-Dimensional Poisson Equation with Point-Wise Forcing" to appear in *Journal of Computational Physics*, 1989.
5. L. Van Dommelen, "On the Lagrangian Description of Unsteady Boundary-Layer Separation. Part I: General Theory", Submitted to the *Journal of Fluid Mechanics*.
6. L. Lourenco, A. Krothapalli, J. M. Buchlin, and M. L. Riethmuller, "A Non-Invasive Experimental Technique for the Measurement of Unsteady Velocity and Vorticity Fields", in *Aerodynamic and Related Hydrodynamic Studies Using Water Facilities*", AGARD CP 413, 1988.

Appendices

1. AIAA Paper 87-0459: Unsteady Separated Flows: A Novel Experimental Approach.
2. Fast, Adaptive Summation of Point Forces in the Two-Dimensional Poisson Equation, Journal of Computational Physics Paper.
3. Summary of the Computational Scheme.
4. On the Lagrangian Description of Unsteady Boundary-Layer Separation. Part I: General Theory, Journal of Fluid Mechanics Paper.

APPENDIX I

AIAA Paper 87-0459: *Unsteady Separated Flows: A Novel Experimental Approach.*

AIAA'87

AIAA 87-0459

**Unsteady Separated Flows: A Novel
Experimental Approach**

A. Krothapalli and L. Lourenco

The Florida State University, Tallahassee, FL

AIAA 25th Aerospace Sciences Meeting

January 12-15, 1987/Reno, Nevada

For permission to copy or republish, contact the American Institute of Aeronautics and Astronautics
1633 Broadway, New York, NY 10019

24

UNSTEADY SEPARATED FLOWS: A NOVEL EXPERIMENTAL APPROACH

A. Krothapalli¹ and L. Lourenco²

Department of Mechanical Engineering
FAMU/FSU College of Engineering
The Florida State University, Tallahassee, FL 32306

Abstract

A novel experimental technique, commonly referred to as Laser Speckle Velocimetry (LSV) or Particle Image Displacement Velocimetry (PIDV), is developed for the measurement of instantaneous velocity fields in unsteady and steady flows. The main advantage of this technique is that the velocity field is measured with sufficient accuracy so that the distribution of vorticity can be calculated with accuracy.

The PIDV technique, which is ideally suited for the study of unsteady separated flows, has been utilized to measure the development of the separated flow field generated by an high angle of attack ($\alpha=30^\circ$) NACA 0012 airfoil started impulsively from rest.

1. Introduction

For the solution of many problems that occur in high angle of attack aerodynamics, it is a necessary to have a thorough understanding of the behavior of unsteady separated flows. Although much progress has been made in predicting the steady flow phenomenon with the use of numerical methods, it is still difficult to predict unsteady flows which contain flow separation. The difficulty mainly arises from the fact that these flows are extremely complex and are not amenable to standard experimental and numerical techniques. In view of this, a novel experimental technique is being developed for the measurement of instantaneous velocity fields in unsteady and steady fluid flows. This paper provides a description of this technique along with its successful application to the study of an unsteady separated flow generated by an high angle of attack airfoil.

In an unsteady flow, a single photograph of the flow pattern at a given instant does not generally provide any meaningful information. In order to understand the unsteady flow phenomena, it is necessary to obtain both spatial and temporal information of the entire flow field. With this in mind, optical techniques have been widely used to observe and measure properties of flow fields such as velocities and densities. Many of these techniques are qualitative in nature, but of great value in guiding intuition and in suggesting ways to investigate the problem by quantitative means. An admirable review of the modern optical techniques in fluid mechanics is

given by Lauterborn and Vogel¹, and the reader is referred to this article for details. A quantitative flow visualization technique would be very helpful in the study of these flow fields. Attempts to accomplish this task by tracing the streaklines of injected particles^{2,3} usually can not provide the spatial resolution that is required and a large amount of labor is necessary to reduce the data.

In unsteady separated flows, as will be shown later, it is often desirable to obtain the vorticity field, in addition to the velocity field. However, measurement of the vorticity exceed the present experimental capability. This difficulty arises from the fact that vorticity is a quantity defined in terms of local velocity gradients. In contrast, the currently available measurement techniques, such as hot-wire anemometry or laser velocimetry, are sensitive only to the local velocity. Hence, measurements must be made over several points and the resulting velocity components are then analyzed by finite difference schemes. However, the errors produced by the necessary differentiations limit the accuracy and spectral range. In addition, the spatial resolution of this method is often not sufficient to measure small-scale fluid motions or rapidly changing velocity gradients. As a consequence, the measured vorticity field is a type of spatially averaged estimate of the actual vorticity field. Finally, this method provides information at only a single point. If information on the entire flow field is required, measurements must be carried out sequentially one point at a time. This sequential method, although laborious, is straightforward in applications involving steady flows. However, the method becomes very difficult, if not impossible to implement, when studying unsteady flows. Direct measurement of vorticity has been tried, for instance, by injection of spherical particles which rotate in the flow with an angular velocity proportional to the local vorticity⁴. Such methods suffer the same drawback of insufficient spatial resolution just mentioned and also can be quite complex.

Recently, a novel velocity measurement technique, commonly referred to as Laser Speckle Velocimetry (LSV) or Particle Image Displacement Velocimetry (PIDV) has become available. This technique provides the simultaneous visualization of the two-dimensional streamline pattern in unsteady flows as well as the quantification of the velocity field over an entire plane. The advantage of this technique is that the velocity field can be measured over an

¹ Associate Professor and member of AIAA
² Assistant Professor and member of AIAA

entire plane of the flow field simultaneously, with accuracy and spatial resolution. From this the instantaneous vorticity field can be easily obtained. This constitutes a great asset for the study of a variety of flows that evolve stochastically in both space and time, such as the unsteady vortical flows that occur in rotorcraft and high-angle-of-attack aerodynamics. For the background of this present technique, the reader is referred to reference 5.

The principle of the technique is given in the next section followed by the description of the apparatus, instrumentation and procedures. Section 4 provides the results and their description for the flow over an high angle of attack NACA 0012 airfoil.

2. Principle of the Technique

The application of LSV or PIDV to fluid flow measurement involves several steps. First, it is necessary to "create" a selected plane or surface within the flow field. This is accomplished by seeding the flow with small tracer particles, similarly to LDV applications, and illuminating it with a sheet of coherent light, as shown in Figure 1. A pulsed laser such as a Ruby or a NdYag laser, or a CW laser with a shutter is normally used as the light source. The laser sheet is formed, for example, by focusing the laser beam first with a long focal length spherical lens, to obtain minimum thickness, and then diverging the beam in one dimension with a cylindrical lens. The light scattered by the seeding particles in the illuminated plane provides a moving pattern. When the seeding concentration is low, the pattern consists of resolved diffraction limited images of the particles. When their concentration increases, the images overlap and interfere to produce a random speckle pattern. A multiple exposure photograph records this moving pattern. The lower particle concentration originates a mode of operation of the technique referred to as Particle Image Displacement Velocimetry, reserving the term Laser Speckle Velocimetry for the high particle concentration levels where a random speckle pattern is actually formed (reference 6). In a second step the local fluid velocity is derived from the ratio of the measured spacing between the images of the same tracer, or speckle grain, and the time between exposures.

Several methods exist to convert the information contained in the multiple-exposed photograph, or specklegram, to flow field data such as velocity or vorticity. The recorded image, whether formed by isolated disks, in the case of low particle concentration, or speckle grains for high particle concentration is a complicated random pattern. It would be very difficult to measure the local displacements by visual or computer-aided inspection. However, it is important to realize that the multiple exposure photograph results in a periodic random image from which the periodicity information can

be retrieved using Fourier or Auto-correlation analysis. Basically, the multiple-exposed photographs or specklegrams can be analyzed either on a point-by-point basis, which yields measurements of the local displacements (velocity), (refs. 7-8) or with a whole field filtering technique, which yields isovelocity contours (ref. 9). The method, which has been selected and implemented by the Fluid Mechanics Research Laboratory at the Florida State University, is the Young's fringes method. The local displacement is determined using a focused laser beam to interrogate a small area of the multiple exposed photograph transparency. The diffraction produced by coherent illumination of the multiple images in the negative generates Young's fringes, in the Fourier plane of a lens, provided that the particle images correlate. This is shown schematically in Figure 2. These fringes have an orientation which is perpendicular to the direction of the local displacement and a spacing inversely proportional to the displacement. The use of Young's fringes eliminates the difficulties of finding the individual image pairs in the photograph. The basis of the Young's fringe method is described in reference 8.

The photographic recording method discussed above has the disadvantage that the photograph consists of particle pairs which have a 180 degree ambiguity in the direction of the velocity vector. In addition, it has been shown (reference 10) that the velocity dynamic range of the technique is limited to a maximum value of about 10. In most flows of interest (e.g. boundary layers and separated flows), this dynamic range is not sufficient to capture the flow field in its entirety. These limitations are critical when measuring complex flows having flow reversals and stagnation areas.

A method to resolve both the ambiguity of the velocity vector as well as to improve the technique's velocity range is incorporated in this experiment. This method, proposed by Lourenco¹¹ and Adrian¹², commonly known as "velocity bias technique", consists of recording the flow field in a moving reference frame, thus superposing a known velocity bias to the actual flow velocity. This effect may be accomplished in several ways, in particular, using a moving camera during the photographic recording or by optical means using scanning or rotating mirrors. For the data presented here, a rotating mirror was used to displace the image during the exposure with a pre-determined velocity. A schematic of the rotating mirror arrangement is shown in figure 3. Consider two particle pairs $A_0 B_0$ and $C_0 D_0$ having equal displacements in opposite directions in the object plane. By introducing a 45° mirror between the camera lens and the object plane, the corresponding displacements appear in the film plane as AB and CD with equal magnitudes. When the mirror is rotated by an angle of $\Delta\theta$ between exposures, the displacements corresponding to $A_0 B_0$ and $C_0 D_0$ appear in

the film plane as AB¹ and CD¹ with different magnitudes. The correct displacement or velocity with its direction can now be obtained upon removal of the velocity bias. An example of the flow field obtained with and without the velocity bias can be seen in figure 4. This flow represent a typical separated flow field containing flow reversal and stagnation areas (a discussion of this flow field is given later).

3. Apparatus, Instrumentation and Procedures

The time-space development of the unsteady separated flow generated by an high angle of attack ($\alpha=30^\circ$) NACA 0012 airfoil impulsively started from rest is examined using Particle Displacement Velocimetry. The flow is created by towing the airfoil in the reduced scale Fluid Mechanics Research Laboratory towing tank facility. The tank is 300 x 200 x 600 mm. A detailed examination showed that the motion of the towing carriage is smooth and vibration free. The towing carriage is driven by a variable D.C. motor, and the towing velocity can vary from 0 to 100 mm/sec. For the photography, a 35mm camera (Nikon F-3) is used. To photograph the flow at regular time intervals, the photographic camera has a electric winding device. The photographic time interval available with this camera can be continuously varied up to a maximum of 6 frames per second. Two options are available to fix the camera; one by attaching it to the towing carriage, which means an observation point fixed in relation to the model, and the other by attaching it to the frame of the water tank, which means an observation point fixed in relation to the fluid. The selection of these two depends upon the flow field being photographed.

In this experiment the airfoil chord is 60mm and is towed with a velocity of 22mm/sec. The corresponding Reynolds number was 1400. The fluid used in this experiment was water seeded with 4 μ m metallic coated particles (TSI model 10087). For the illumination, a laser beam from a 5 Watt Argon-Ion Laser (Spectra-Physics series 2000) is steered and focused to a diameter of .3mm using an inverse telescope lens arrangement. A cylindrical lens, with a focal length of -6.34mm, is used to diverge the focused beam in one dimension, creating a light sheet. The laser sheet is 70mm wide and illuminates the mid-span section of the airfoil. For the multiple exposure, the CW laser beam is modulated using a Bragg cell. In this experiment, the laser power density, I_0 , of the sheet was .27 W/mm². In order to record the time development of the flow field, the camera was attached to the towing carriage and the frequency of which the multiple exposures were taken was set at 2.0Hz. The aperture of the lens with a focal length of 50mm and a spacer of 12mm, was set at F#5.6 and the resulting magnification factor was 0.40. For the multiple exposure, the time between exposures, T, and the exposure

time, t, are chosen according to the criteria discussed in reference 6. The time between exposures was 10msec. For optimum exposure, the exposure time was 1msec, which corresponded roughly to (d_p/MV_{max}) , where D is the analyzing beam diameter, V is the maximum expected velocity plus the shift velocity in the field and d_p is the particle image diameter expressed in terms of

$$d_i = (d_p^2 + d_s^2)^{1/2}$$

with d_p the particle diameter and d_s the edge spread caused by the limited response of the recording optics (ref. 6).

Data Processing

The fringe images were acquired and analyzed using the digital image analysis system of the Florida State University FMRL (Fig. 5). This system consists of the following components: a DEC LSI-11/73 host computer, Gould IP-8500 Digital image processor which includes four memory tiles for storage of image data in a 512 x 512 format with a resolution of 8 bit per pixel, a frame digitizer, a pipeline processor and a video output controller to convert digital to analog information for display on a color monitor. The system also includes a two-dimensional Klinger traversing mechanism with a controller for the purpose of automatically scanning the film transparencies. Two methods are available and used for fringe analysis (ref. 10). The first one is an interactive method in the sense that it requires the assistance of an operator.

The inconvenience of the one-dimensional averaging method is the need for an external adjustment of the angle of the fringes by an operator. This problem can be by passed by computing the velocity components along independent directions. Because each line of the fringe frame can be considered as a noisy periodic signal with variable phase, the automatic determination of a velocity component can be performed only by averaging over a quantity independent of the phase. The autocorrelation for each line or its Fourier transform for the power spectrum satisfies this requirement. The m velocity component can be computed from:

$$g(u) = \sum_{n=0}^{511} \left[\frac{\sum_m \{I(m,n)I(m+u,n)\}}{\sum_m \{I(m,n)\}^2} \right] - 511 < u < 511$$

This algorithm has been implemented using the pipeline processor of the Gould IP-8500 image processor to perform simultaneously the autocorrelation for all the lines of a frame. For an accurate estimate of the velocity magnitude and directions, four of such full image operations, yielding four autocorrelation functions, are required. From these the velocity vector is determined by selecting the values of the components which have been computed from autocorrelations having the

highest SNR, and visibility. (The computation, which includes the determination of the fringe angle and position updating of the film transparency scanning mechanism, is completed in a few seconds, typically 4-5 sec, using the PDP 11-73 computer.)

The overall accuracy of the technique was evaluated using a method described in reference 10. A uniform flow field is created by producing a multiple exposure photograph of the still seeded water, in the water tank, with a camera moving at constant speed. For the multiple exposure photograph a number of time between exposures are used, thus resulting in photographs with particle pairs at different known distances.

In the absence of a systematic bias, the standard deviation of the obtained velocity distribution is an estimate of the mean measurement error. From the error analysis, it is believed that the velocity data is obtained with an accuracy of 2 percent or better.

4. Results and Discussion

Typical multiple exposure photographs of the flow generated by the impulsively started NACA 0012 from rest for different times are shown in figure 6. The photographic arrangement was purposely adjusted to enhance the view of the flow field on the upper surface of the airfoil rather than to show the entire flow around the airfoil. Consequently, the details of the flow under the airfoil can not be seen clearly in these photographs. The angle of attack of the airfoil is set at 30° . These pictures display the flow field from the leading edge to a downstream location of about 1.5 chords. Photographs were taken at a frequency of 2Hz. A total of 34 pictures were obtained covering the range of t^* from 0.1 to 5. The non-dimensional time, t^* ($= Ut/c$, where U is the free stream velocity, t is the time between two successive pictures, and c is the chord of the airfoil) between successive pictures was 0.167. However, in figure 6, only a limited number of pictures are included. The quadruple exposed photographs shown here increase the SNR (signal to noise ratio), the fringe visibility, and provide an excellent flow visualization. The added advantage of providing a good flow visualization is an asset of the PIDV technique.

From the flow visualization pictures shown in figure 6, the following observations are made. At the start of the airfoil a vortex, at the trailing edge, commonly known as "starting vortex", is generated and is carried away from the body. concomitant with this is the generation of a separation bubble at the leading edge of the airfoil (figure 4a). At a later time, for example at $t^* = 1.2$ (figure 4b), the separation bubble grows into an isolated primary vortex with "secondary vortices" following behind it. Similar type of vortex structure was also observed¹⁰ in the flow behind a circular

cylinder. This multiple vortex structure continue to grow together until the t^* reaches a value of about 2.5 (figure 4c and 4d). At $t^* = 2.5$ (figure 4d), because of the close proximity of the primary vortex, a trailing edge vortex is generated. At $t^* = 2.75$ the primary vortex abruptly moves away from the surface of the airfoil leaving behind a "vortex sheet" like structure (figure 4e). For $t^* > 3.0$, this "vortex sheet" rolls up into distinct vortices and they grow in size with time as shown in figure 4f - 4g. During this process, the trailing edge vortex also grows and as a result the whole flow field becomes very complex. Close to the surface of the airfoil, a small vortex remain present for $t^* > 3.0$. This vortex has the same sign of rotation as the trailing edge vortex. A similar vortex structure was observed by Ho¹¹, who calls it an "induced vortex" and associates it with unsteady separation phenomenon.

The velocity data is acquired in a Cartesian mesh by digital processing of the Young's fringes, produced by point-by-point scanning of the positive contact copy of the photograph. The scanning step size and the dimension of the analyzing beam are 0.5mm, which corresponds to a spatial resolution of about 1.25mm in the object plane or about 0.02c. The fringes were processed using the method described in the previous section. The resultant two-dimensional velocity fields, corresponding to figure 6a - 6h, are shown in figure 7. The length of each vector is proportional to the local velocity at that point. The color code superimposed on the velocity data represents the vorticity level, the magnitude of which is given by the color bar at the bottom of the picture. The red and green colors represent the peak positive and negative vorticity regions respectively. This type of display clearly depict the various regions of vorticity and its strength. As discussed above, the presence of primary vortex, secondary vortices, vortex sheet trailing edge vortex and the induced vortex on the surface of the airfoil are clearly depicted along with their time-space development. The detailed analysis of this data is being conducted at this time and will be reported later.

5. Conclusions

A recently developed velocity measurement technique, known as Particle Image Displacement Velocimetry (PIDV), has been briefly described. Using this technique, the time-space evolution of the flow generated by an impulsively started high angle of attack ($\alpha=30^\circ$) NACA 0012 airfoil is presented. This experiment illustrated the technique's capabilities to record with accuracy the complex unsteady separated flow.

The technique has been shown to provide both flow visualization and quantitative measurements, which include the velocity and vorticity fields.

The unsteady separated flow field generated by an high angle of attack airfoil contains many large scale vortical structures such as; primary vortex generated at the leading edge with secondary vortices upstream of it, trailing edge vortex, vortex sheet and an induced vortex in the upper surface of the airfoil. The origins and time development of these are clearly depicted by the instantaneous velocity and vorticity fields obtained using PIDV.

Acknowledgments

The development of the PIDV is generously supported by the Aeromechanics branch of NASA Ames Research Center under grant no. NAG 2-314. While the study of the unsteady flow past high angle of attack airfoils is supported by the Air Force Office of Scientific Research under grant no. AFOSR-86-0243.

References

1. Lauterborn, W., and Voget, A., "Modern Optical Technique in Fluid Mechanics", Annual Review of Fluid Mechanics, vol. 16, 1984, pp 223-244.
2. Gharib, M., Herman, M.A., Yavrouian, A.H., and Sarohia, V., "Flow Velocity Measurement by Image Processing of Optically Activated Traces", AIAA paper no. 85-0172, 1985.
3. Dimotakis, P.E., Debussy D., and Koochesfahani, M.M., "Particle streak Velocity Field Measurements in a Two-dimensional Mixing Layer", Physics of Fluids, vol. 24, 1981, pp 995-999.
4. Fish, M.B., and Webb, W.W., "Direct Measurement of Vorticity by Optical Probe", Journal of Fluid Mechanics, vol. 107, 1981, pp 173-200.
5. Smith, C.A., Lourenco, L.M., and Krothapalli, A., "The development of laser speckle velocimetry for the measurement of vortical flow fields", AIAA paper no. 86-0768-CP, 1986.
6. Lourenco, L., and Krothapalli, K., "The role of photographic parameters in laser speckle or particle image displacement velocimetry", Experiments in Fluids, vol. 5, 1986, pp 29-32.
7. Yao, C.S., and Adrian, R.J., "Orthogonal Compression and 1-D Analysis Technique for Measurement of 2-D Particle Displacements in Pulsed Laser Velocimetry", Applied Optics, vol. 23, 1984, pp 1687-1689.
8. Lourenco, L., and Whiffen, M.C., "Laser Speckle Methods in Fluid Dynamic Applications", Laser Anemometry in Fluid Mechanics, Ladoan, Portugal, 1984, pp 51-68.
9. Collicott, S.H., and Hesselink, L., "Anamorphic Optical Processing of Laser Speckle Anemometry Data", Bull, Amer. Phys. Soc., 10, 1985. pp 1928.
10. Lourenco, L., and Krothapalli, A., "Application of PIDV to the Study of the Temporal Evolution of the Flow Past a Circular Cylinder", Proc. of Intn. Symp. on Laser Anemometry Application in Fluid Mechanics, Lisbon, Portugal, July 1986.
11. Lourenco, L., "Application of Laser Speckle and Particle Image Velocimetry in Flows with Velocity Reversal", Bull. Amer. Phys. Soc., vol. 31, no. 10, 1986, p. 1723.
12. Adrian, R.J., "Image Shifting to Determine the Polarity of Velocity Vectors Measured by Pulsed Laser Anemometry", Bull, Amer. Phys. Soc., vol. 31, no. 10, 1986, p. 1722.
13. Ho, C.M., "An Alternative Look at the Unsteady Separation Phenomenon", Recent Advances in Aerodynamics, Springer-Verlag, 1986, pp 165-178.

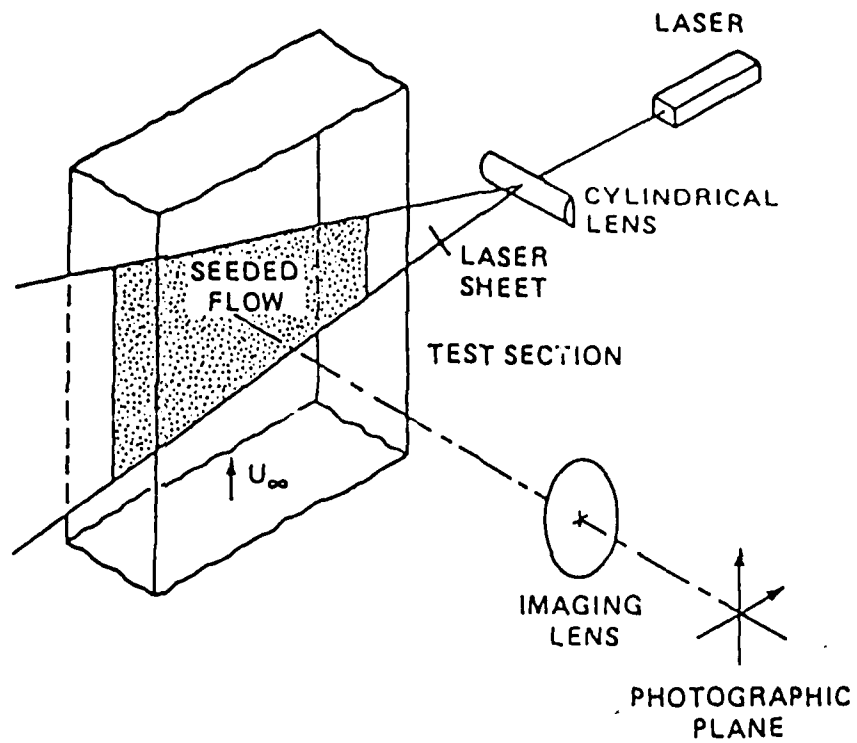


Figure 1. Schematic arrangement for the photographic recording.

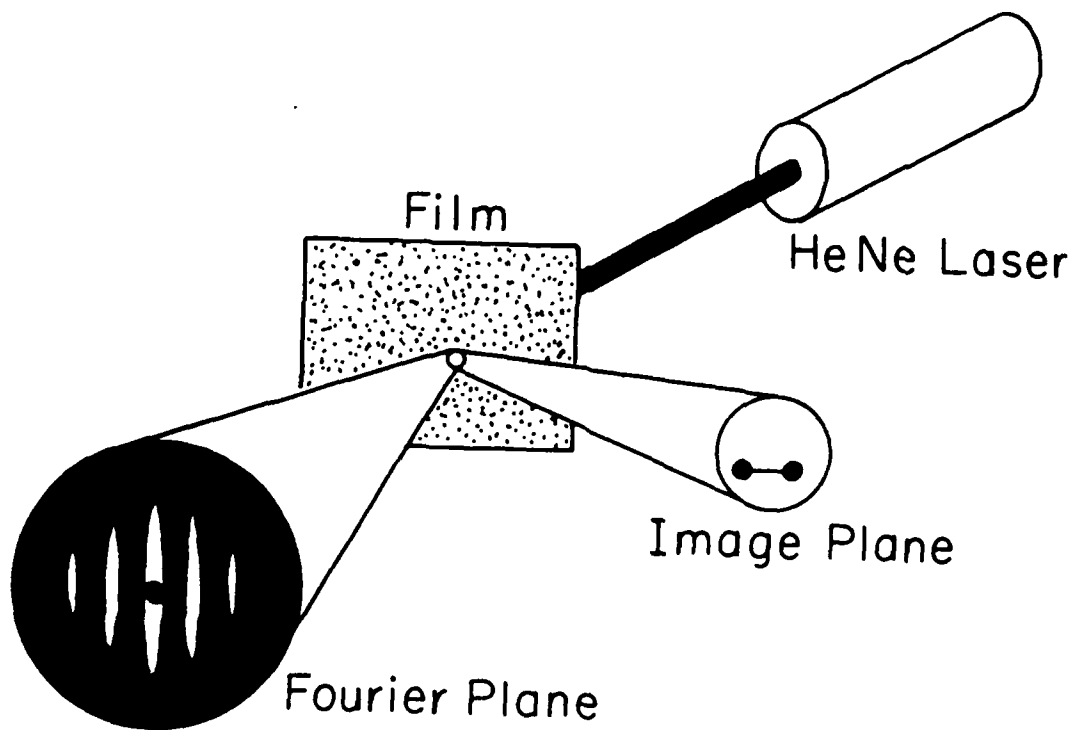


Figure 2. Schematic arrangement for obtaining Young's fringes.

6

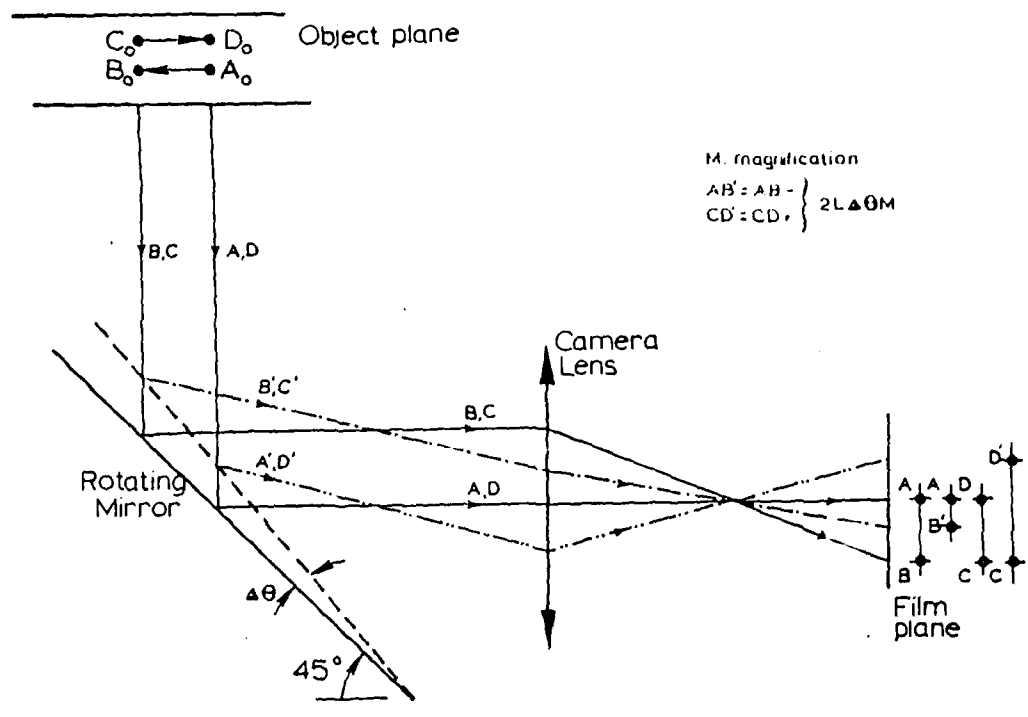


Figure 3. Rotating Mirror arrangement for the Velocity Bias Technique

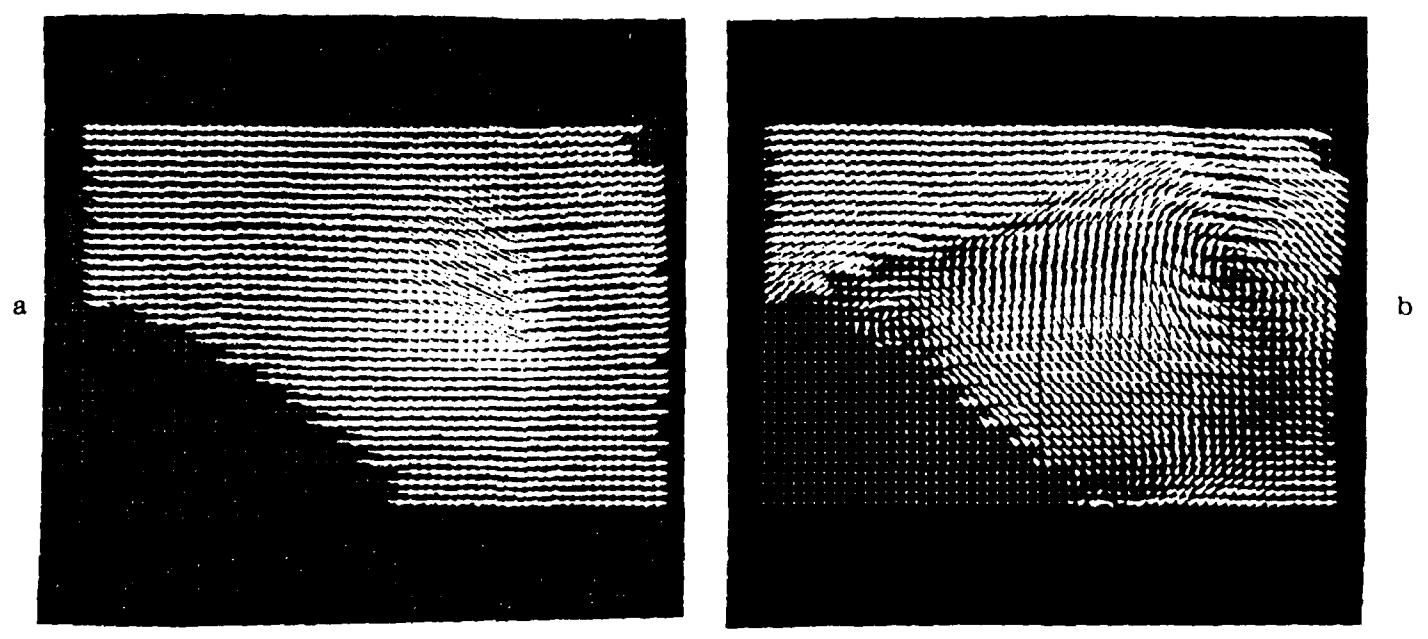


Figure 4. Instantaneous Velocity Field a) Before removal of velocity bias b) after removal of the velocity bias.

7

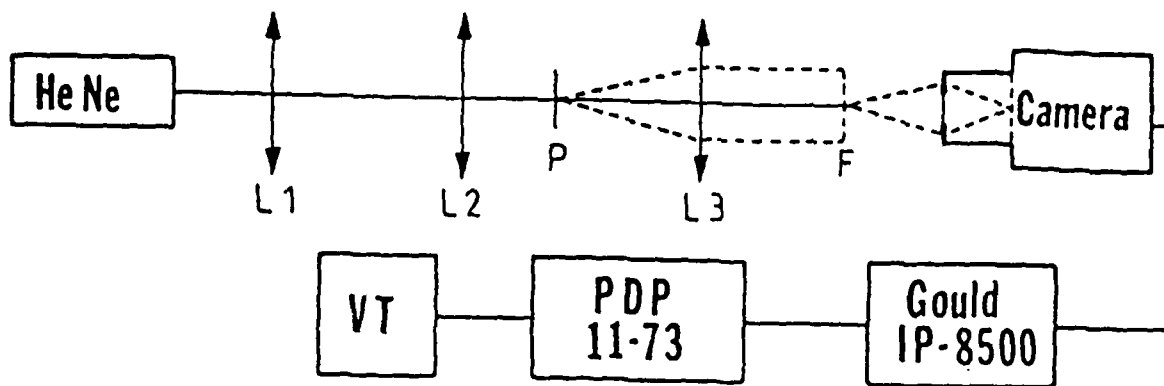
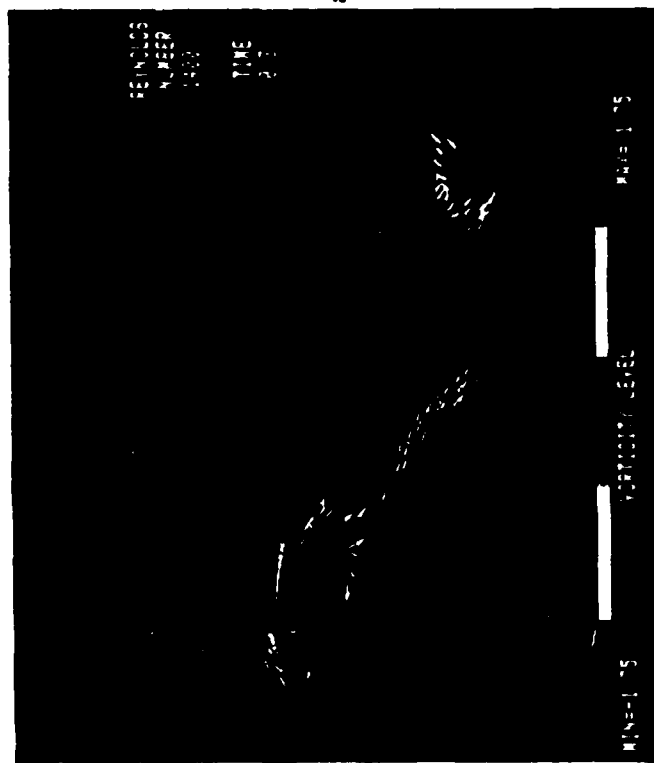
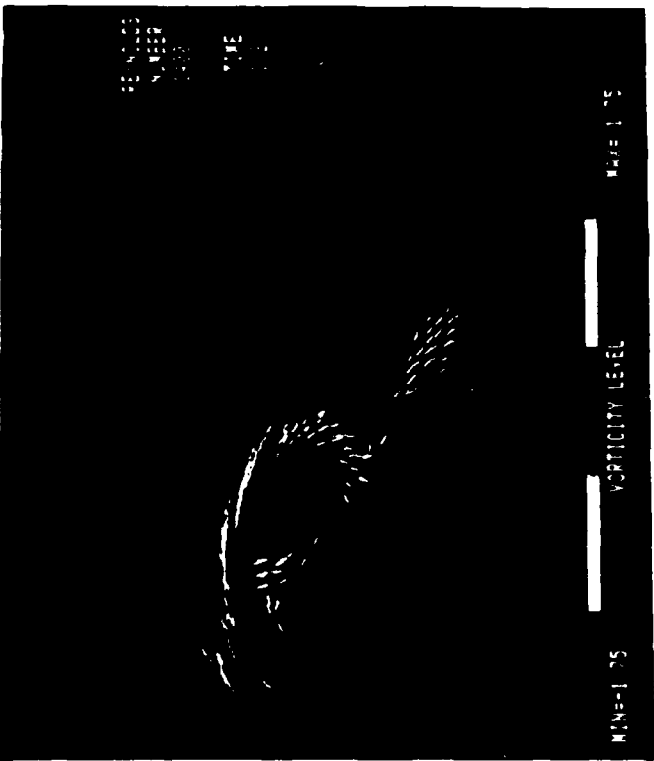


Figure 5. Schematic of the data analysis system

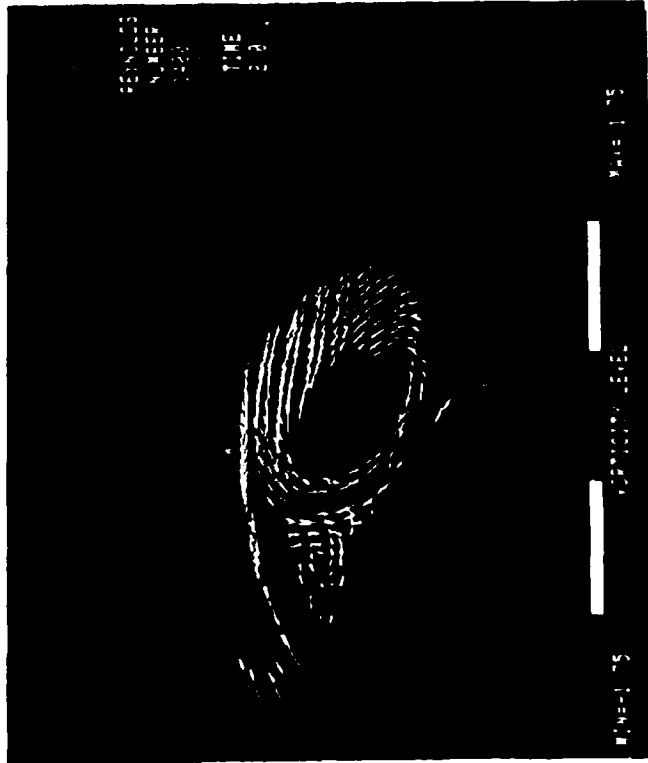
S



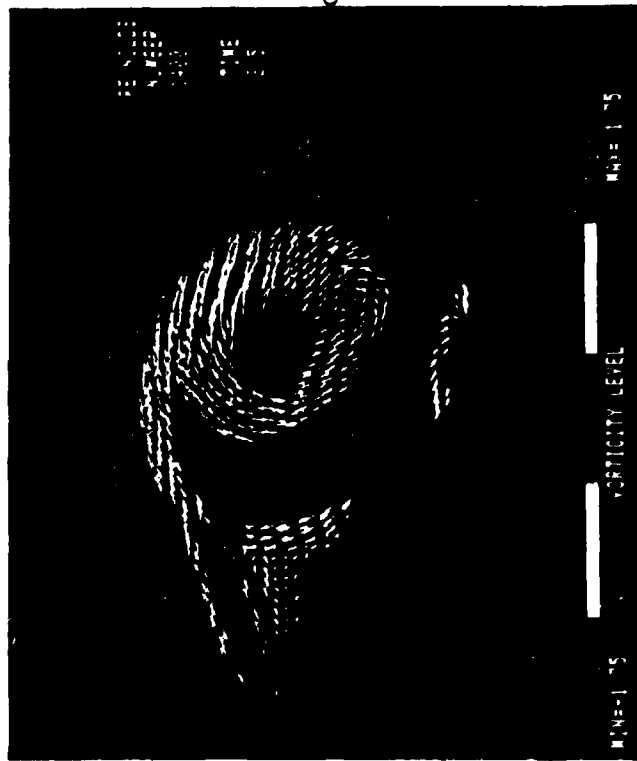
a



b



c



d

Figure 7. Continued

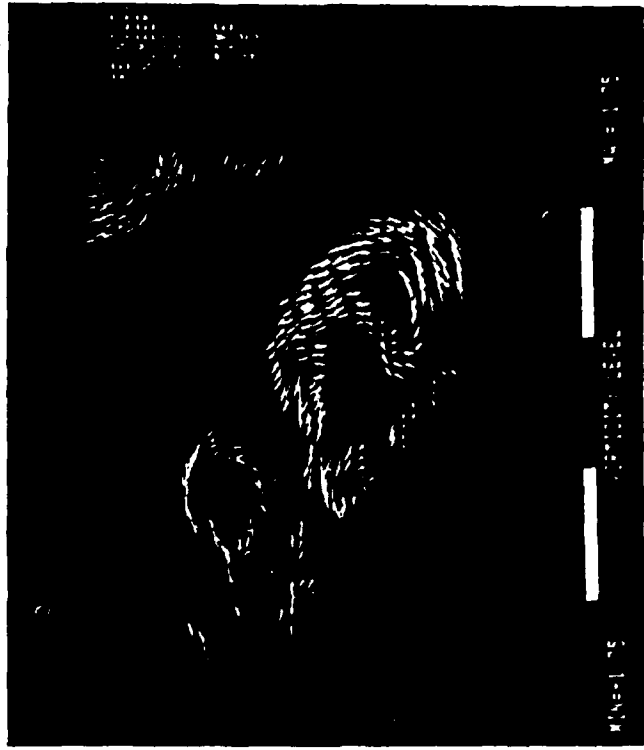
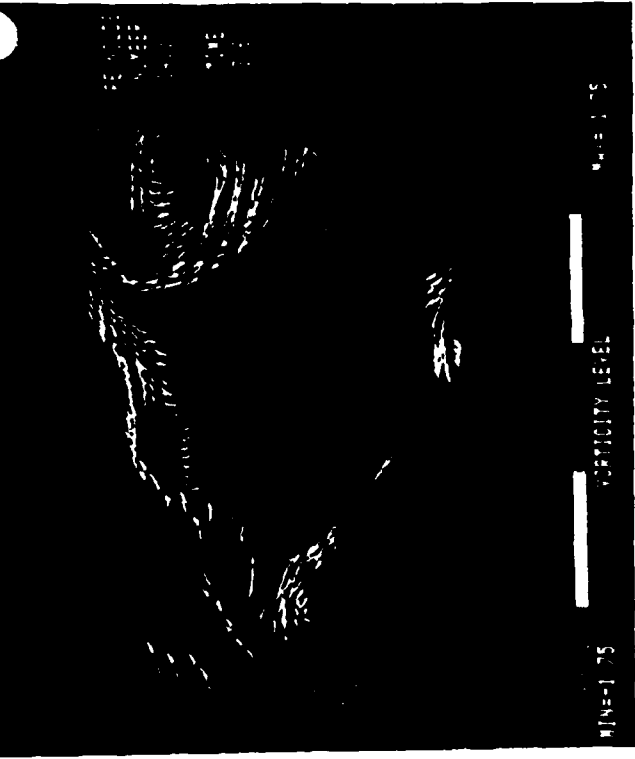
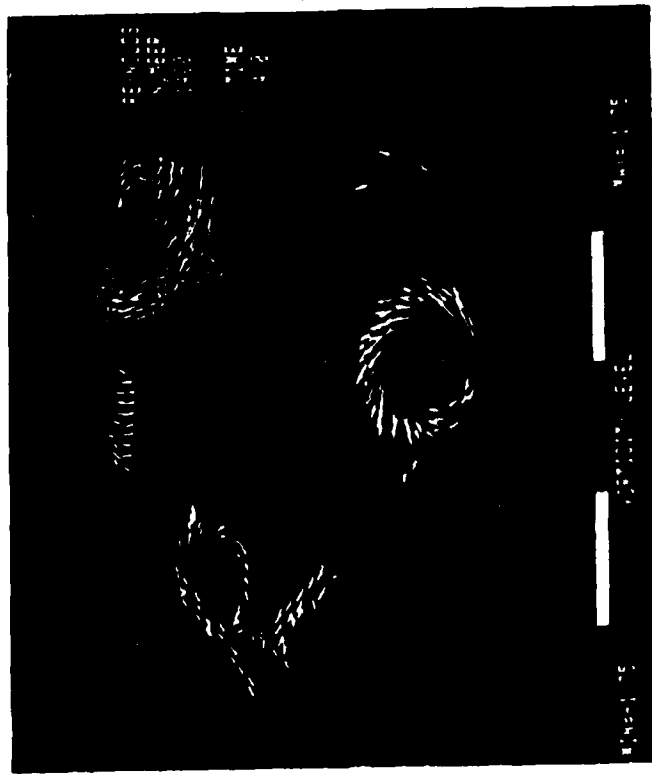
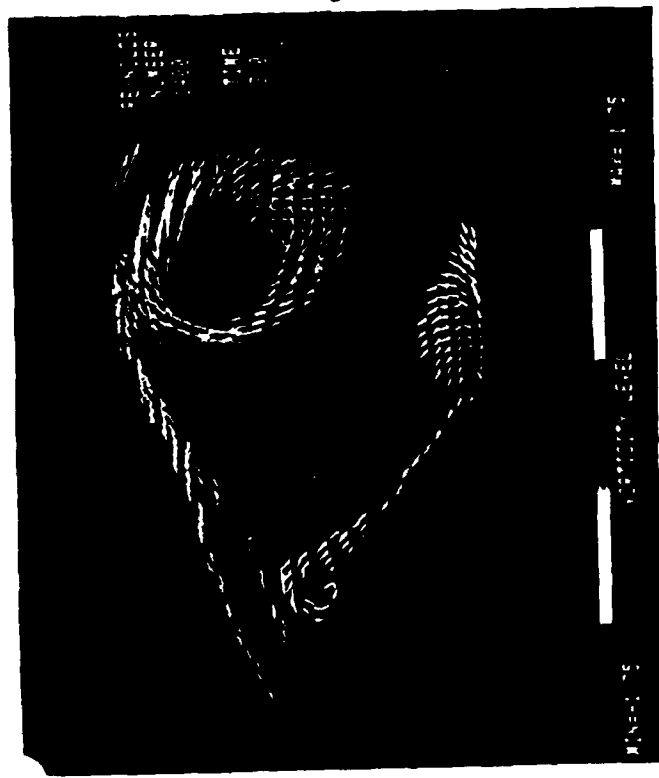


Figure 7. Instantaneous * velocity and vorticity * fields; a) $t^* = 0.3$; b) $t^* = 1.2$; c) $t^* = 2.0$
 d) $t = 2.5$; e) $t = 3.0$; f) $t = 3.6$; g) $t = 4.0$; h) $t = 4.5$

10

APPENDIX II

Fast, Adaptive Summation of Point Forces in the Two-Dimensional Poisson Equation,
Journal of Computational Physics Paper.

5/27/10

~~10~~ 1.

ORIGINAL
20Fast, Adaptive Summation of Point Forces in
the Two-Dimensional Poisson Equation

LEON VAN DOMMELEN

*Department of Mechanical Engineering,
FAMU/FSU College of Engineering & Supercomputer Computations Research Institute,
Florida State University, Tallahassee, Florida 32306*

AND

ELKE A. RUNDENSTEINER

*Department of Computer Science,
Florida State University, Tallahassee, Florida 32306*

Received June 2, 1987; revised September 30, 1988

Direct summation of the velocity field introduced by point vortices tends to be time consuming since the velocity of each vortex is found as a sum over all other vortices. The resulting number of numerical operations is proportional to the square of the number of vortices. Here a relatively simple procedure is outlined which significantly reduces the number of operations by replacing selected partial sums by asymptotic series. The resulting number of operations appears to vary roughly in proportion to the number of unknowns, corresponding to a "fast" solver. © 1989 Academic Press, Inc.

1. INTRODUCTION

Incompressible flow at high Reynolds number with large-scale separation can be difficult to compute since the vorticity tends to concentrate in limited parts of the flow field. Vortex methods [1] attempt to reduce the number of variables needed for the computation by describing only the vorticity, in its simplest form, by a series of delta-functions or point vortices:

$$\omega = \sum_{i=1}^N \Gamma_i \cdot \delta(\mathbf{x} - \mathbf{x}_i). \quad (1)$$

The flow velocity is related to the vorticity by the solution of a Poisson equation, with the vorticity as forcing function, resulting in the stream function. The flow velocity is found by taking the curl of the stream function. The solution for a series

001

0021-9991/89 \$3.00

Copyright © 1989 by Academic Press, Inc.
All rights of reproduction in any form reserved.

0021-9991/89 \$3.00

Copyright © 1989 by Academic Press, Inc.
All rights of reproduction in any form reserved.

FAST ADAPTIVE SUMMATION

001

002

VAN DOMMELEN AND RUNDENSTEINER

of delta functions can be found and leads to the following expression for the flow velocity:

$$V_j^* = \frac{\sqrt{-1}}{2\pi} \sum_{i=1}^N \Gamma_i \frac{1}{Z_j - Z_i}, \quad j = 1, 2, \dots, N, \quad (2)$$

where Z is the complex position $x + \sqrt{-1}y$ and V^* the complex conjugate velocity $u - \sqrt{-1}v$. In general, it will be necessary to add to this flow velocity a solution of a Laplace problem to take care of the boundary conditions.

While the sum in Eq. (2) may easily be evaluated, the number of terms is proportional to the square of the number of vortices N . Thus, the computational effort increases rapidly when the number of vortices increases. In contrast, various mesh-based solution procedures for the Poisson equation are able to find the solution in a computational time roughly proportional to the number of mesh cells. As a result, a point vortex description seems most useful if (a) the number of vortices is much smaller than the number of mesh cells needed to describe the flow (i.e., the vorticity is restricted to a small part of the total domain); (b) the point-singularity description itself is of particular interest and the errors induced by a mesh-based representation must be avoided; or (c) the infinite domain implicit in Eq. (2) is to be preserved. Certainly discrete vortex representations have drawn and continue to draw considerable theoretical and numerical interest. In addition, the Poisson equation is not unique to fluid mechanics; it arises in other fields such as electromagnetism and gravitation. For these reasons, more efficient procedures to evaluate the solution under pointwise forcing are of considerable interest.

Various methods to reduce the computational effort have been proposed. Anderson [2] used a fast Fourier transform method, with corrections for the interactions between nearby vortices. However, some of the mentioned advantages of the vortex method are lost due to the presence of the mesh. In addition, for high accuracy the evaluation of the interactions between neighboring vortices can become computationally intensive.

An alternative approach followed in this paper is, to group the vortices spatially and to approximate the effects induced by each group at large distances. Appel [3] and Barnes and Hut [4] made approximations using a single replacement element. Yet, using such approximations, high accuracy is difficult to achieve while the algorithm tends to be scalar.

In contrast, the present study uses a Laurent series approximation for the velocity induced by each group. This approximation takes the form

$$V_j^* = \sum_{k=-1}^{\infty} \frac{C_k}{(Z_j - Z_0)^k} \quad (3a)$$

$$C_k = \frac{\sqrt{-1}}{2\pi} \sum_i \Gamma_i (Z_i - Z_0)^{k-1}, \quad (3b)$$

where Z_0 is a suitably chosen origin point for the group of vortices and the sum in (3b) extends over all vortices in the considered group. The Laurent series allow the desired accuracy to be maintained by the choice of the truncation of the infinite sum. In addition, when the point j at which the velocity is to be evaluated is sufficiently far distant from the group of vortices, the series converges geometrically and only a limited number of terms is needed for given accuracy. Savings in computational effort result when the number of terms needed for the Laurent series is sufficiently small compared to the number of vortices in the group. For that reason, a minimum group size exists below which further savings are not made. Using the adaptive algorithm on a CYBER 205 computer, Van Dommelen and Rundensteiner [5] found that this group size is of the order of a 100 elements.

At about the same time, similar ideas were developed by Rokhlin [6] and Greengard and Rokhlin [7]. In fact, an adaptive algorithm developed by Carrier, Greengard, and Rokhlin [8] is quite similar to the present one in both the use of Laurent series and the grouping involved. An important difference between the procedures is how the adaptive group structure is addressed. While the procedure [8] is based on five topological sets expressing the relationships between groups, the present procedure is based on an unusual numbering system of the groups. The numbering system is generated simultaneously with the group structure; it leads to a relatively simple and streamlined program logic.

The procedure of Greengard and Rokhlin recasts the Laurent series as Taylor series to achieve further reductions in computational operations, an enhancement not yet incorporated in the present scheme. However, unless the number of vortices is sufficiently large, the possible savings seem limited. Furthermore, not recasting the series offers some compensating advantages, such as reduced storage (only a vanishingly small fraction of the Laurent series expansions need be stored), increased vector length, and less overhead.

In its present form, our procedure can be divided into two parts: generation of an adaptive panel structure, to group the vortices spatially, and determination of the velocity. The next two sections describe each of these steps in turn.

2. GENERATION AND NUMBERING OF THE PANELS

In order to use Laurent series effectively, the vortices must be spatially grouped together. Figure 1 illustrates a typical grouping for the example of flow about a circular cylinder. In this example, there are 16,479 vortices outside the cylinder (shown as dots) and an equal number of mirror vortices inside the cylinder (not shown).

The procedure for generating this panel structure is shown in Fig. 2. The first few steps are further illustrated in Fig. 3. The starting domain is taken as the smallest square that encloses all vortices. This square is subdivided into four squares, or subpanels, of equal size (indicated as A, B, C, and D in Fig. 3). The vortices are reordered so as to group the vortices in each of the four subpanels together (in the

2

3

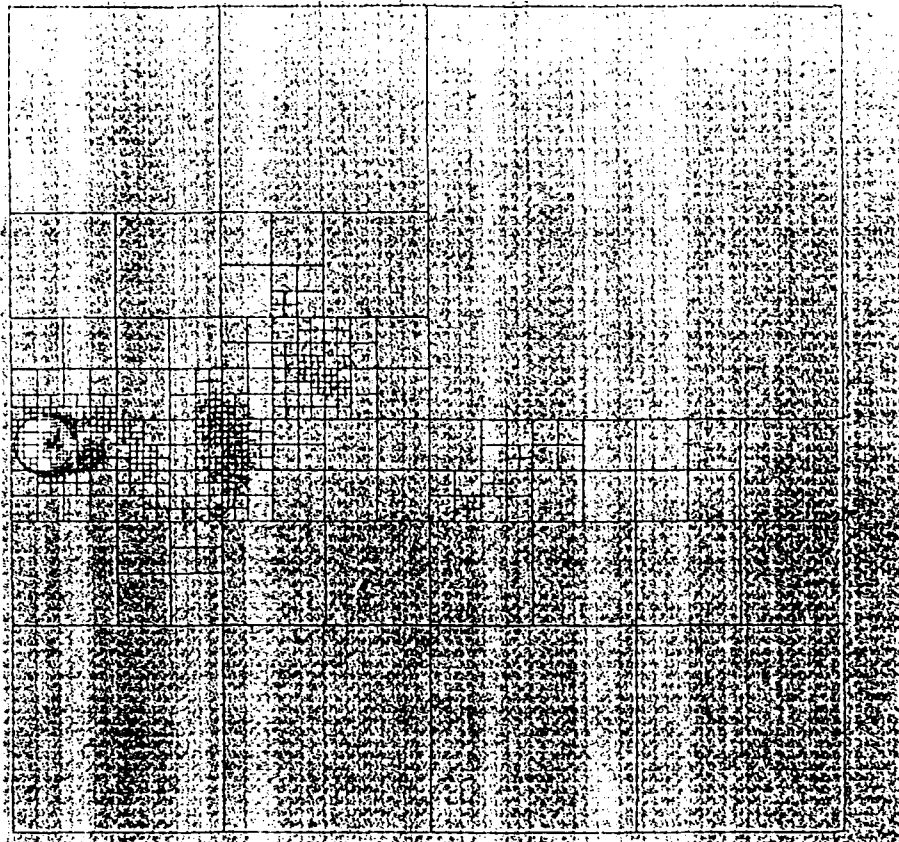


FIG. 1. Example panel structure generated for flow about a circular cylinder. The 16,000 vortices outside the cylinder are shown as dots, an equal number of mirror vortices within the cylinder are not shown.

CYBER 205 implementation, the built-in vector function Q8VCMPRS was used for this purpose).

Information about each of the panels is stored in memory. This information includes the position of the panel and the storage locations of the first and the last vortex within the panel. It also includes an identifying panel number defined later.

After subdivision, execution transfers to the first of the four subpanels generated, and a decision is made whether this panel should be further subdivided. The decision is based on the number of vortices in the panel; if sufficient vortices are present, for example, more than 100, the panel is further subdivided. Meanwhile the panel data for the remaining three subpanels is temporarily stored away in a last-in, first-out buffer. (The last part of the memory allocated for the panel information was used as buffer.)

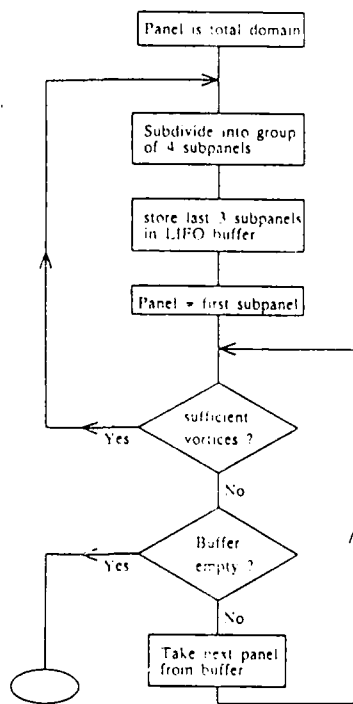


Fig. 2. Basic flow chart for generating the panel structure.

If the considered panel does not contain sufficient vortices, the next panel will be retrieved from the buffer for possible further subdivisions. Proceeding in this manner, the entire domain is subdivided into panels containing a limited number of vortices.

Each of the panels is given a unique number to simplify identification of the panel and its place in the panel structure. Figure 3 illustrates that the storage is always kept in order of increasing panel number. The actual definition of the panel number is illustrated in Fig. 4: all panels which could be created by the subdivision process can be represented as a series of uniform divisions of the domain. For each of these uniform subdivisions, the x - and y -positions can be given a binary number. The four panels generated at the first level of subdivision can be numbered using a one-digit binary number (top of Fig. 4). Each additional level of subdivision requires one additional digit.

Therefore, the binary digits determine the position of the panel. The number of binary digits determines the subdivision level. It follows that the binary digits of the x - and y -positions describe the panels uniquely. The complete information is stored in a single panel number using the following procedure:

5

(a) Increment each digit in both the x - and y -position by one, so that binary zero becomes 1 and binary one becomes 2.

(b) "Interleave" the resulting digits of the x - and y -positions into a single number, so that the odd digits become the digits of the x -position and the even digits those of the y -position.

(c) Add trailing zeros to obtain a final panel number with a fixed and predetermined number of digits. The 205 procedure chooses a 28 digit panel number.

The procedure is illustrated in Fig. 4 for example panels. Since the highest value of the digits in the obtained panel number is 2, it can be considered as the representation of a number in a base-3 notation.

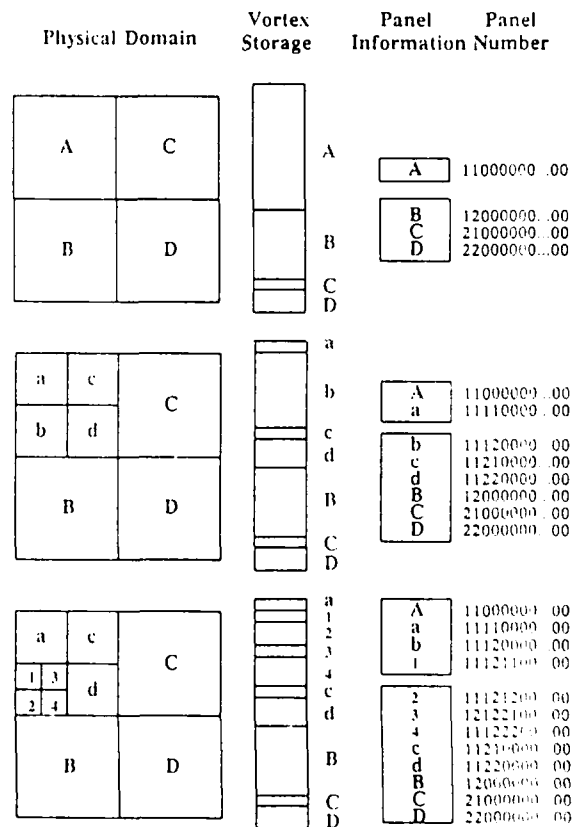


FIG. 3. The first three steps in generating the panel structure of Fig. 1. Shown are: the subsequent divisions of the domain, the order in which the vortices are stored, the order in which the information about the panels is stored, and the numbering of the panels

7

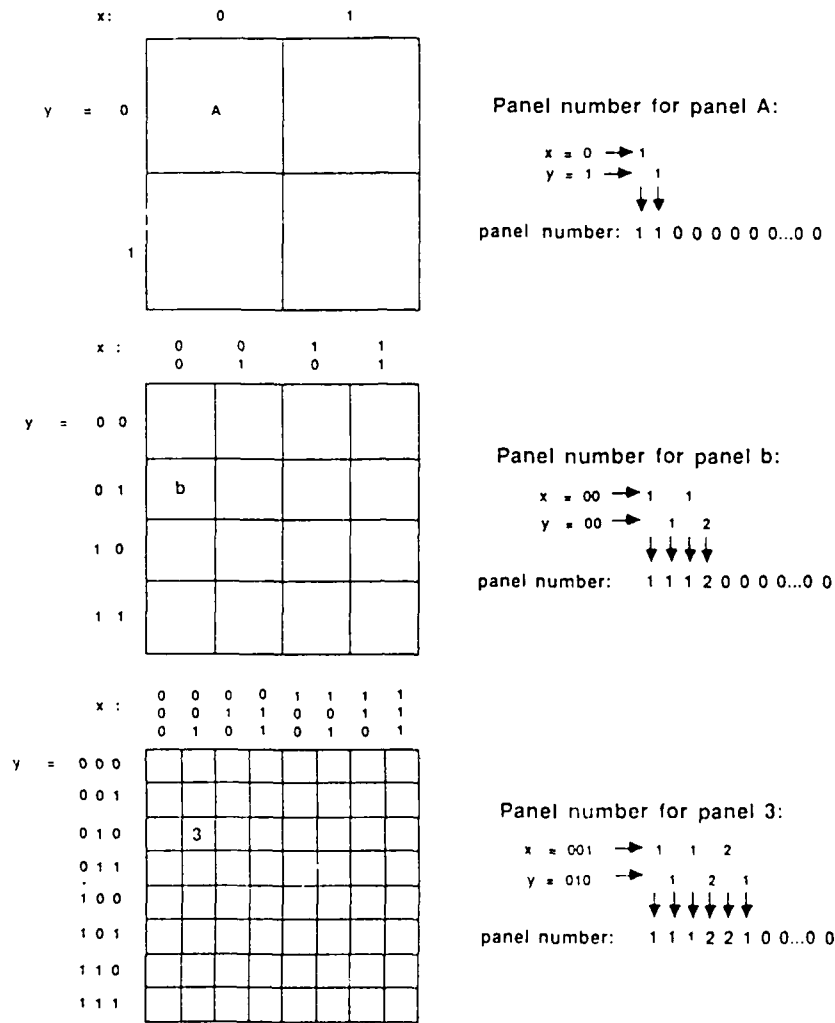


FIG. 4. Definition of the panel number of example panels.

By construction, the panel number contains all the information about the panel: the non-zero digits determine the panel position and the number of pairs of non-zero digits the subdivision level. Particularly important properties are:

- (i) For any given panel, the panel numbers of neighboring panels of the same size may be found by simply binary manipulations. (For example, to find the panel at the same y -position but the previous x -position, determine the odd non-zero digits of the panel number, giving the x -location, and do a binary subtraction of unity to find the digits of the sought panel number.)

(ii) For any given panel number, the panel number of the next larger "mother" panel containing the given panel is found by setting the last two non-zero digits to zero. (The last two non-zero digits were generated by the last panel subdivision.)

(iii) Subpanels of any panel have a panel number greater than the original panel, but less than the next panel of equal size. (The subpanels have the same leading digits as the original panel, but non-zero trailing digits.) This property implies that in order of increasing panel number, panels are arranged in "families," with the subpanels always immediately following the panels of which they are a part.

The algorithm for generating the panels described at the start of this section generates them in order of increasing panel number, subdividing the current lowest panel before moving on to the next panel.

Since each subdivision adds two more non-zero digits, the total number of digits in the panel number limits the smallest panel that can be defined. In the 205 implementation, this total number of digits was chosen to be 28, since 28-digit numbers are the largest base-3 numbers that can be stored in a single 205 memory location, saving storage and computational operations. In 28 digit representation, the smallest panel can be about 16,000 times smaller than the original domain, which would seem sufficient for most purposes.

3. DETERMINATION OF THE VELOCITY

The velocity is determined in a single pass over all panels in the order in which they were generated as described in the previous section. The procedure is outlined in Fig. 5.

For each panel, a "neighborhood" of vortices is established, consisting of the vortices both within the panel itself and in the panels, of at least equal size, sharing a boundary line or a corner point with the considered panel. The vortices in this neighborhood are not summed by the Laurent series expansion of the considered panel. This restriction ensures that the Laurent series converges exponentially. Instead, in evaluating the velocity induced on the neighborhood, the original sum in Eq. (2) is used. This sum is only performed for panels which are not further subdivided; for panels which are subdivided, the velocity is evaluated by means of the subpanels.

Laurent series can be used for all vortices outside the neighborhood of a panel. However, to reduce the computational effort, the Laurent series is only used for those vortices which cannot be evaluated by means of the Laurent series of the next larger "mother" panel: the single Laurent series of the mother panel is more efficient than the four Laurent series of its subpanels. Therefore, the Laurent series of any panel is used only for the vortices within the neighborhood of the mother, but outside the neighborhood of the panel itself.

8

9

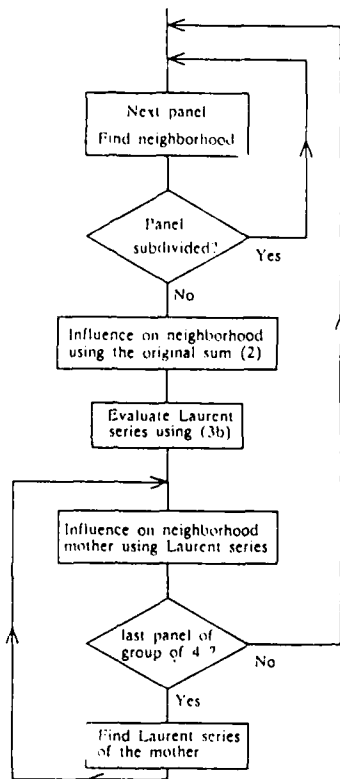


FIG. 5. Basic flow chart for the determination of the velocity.

In this scheme, at each stage the smallest possible number of Laurent series is used, for N vortices resulting in the $O(N \ln N)$ operation counts of the next section. In the procedure of Greengard and Rokhlin [7] this operation count is further reduced to $O(N)$ by recasting the Laurent series as Taylor series; however, the present procedure has the advantage of being less complex and requires only a single sweep over the panel structure to evaluate the velocity.

To incorporate the Taylor series within the present procedure, the evaluation of the neighborhood of the mother would have to be modified. For each suitable panel within this neighborhood, the sum (3a) would be replaced by a recasting of the Laurent series into a Taylor series. Additional steps would be needed to transfer the Taylor series of the larger panels to the subpanels and to add the contributions of these series to the velocity.

Clearly, this will increase program complexity and scalar overhead. In addition, it requires that the neighborhood of the mother is described in terms of individual panels. The present procedure describes this neighborhood in terms of a small number of vectors of vortices, increasing vectorization. Furthermore, the present

procedure has a storage advantage: when the final subpanel of any group of 4 is reached, the four Laurent series of the subpanels can be combined into the Laurent series of the mother (bottom of Fig. 5). The four Laurent series of the subpanels can then be discarded; they are no longer needed. As a result, at any time only a small fraction of the Laurent series need be stored. On the other hand, using Taylor series, no obvious way to avoid storing the Taylor series coefficients for each panel is evident. This can be a disadvantage since each series represents a set of coefficients while, in addition, the total number of panels may be difficult to estimate precisely beforehand.

In the actual implementation of the procedure in Fig. 5, the first step is identification of the neighborhood of each panel. The present procedure starts out by identifying the individual digits of the binary x - and y -positions of the panel. By performing unit binary additions and subtractions, the panel numbers of the eight neighboring panels of the same size are found. For each of these eight panel numbers, the corresponding panel is located. In case any of the eight panels is undefined, the panel with the largest panel number less than or equal to the sought one is selected. On behalf of the properties of the panel number, the selected panel will always enclose the sought panel, ensuring the geometric convergence of the Laurent series. Since the panel numbers are ordered, an appropriate search on a scalar machine is binary; the CYBER 205 implementation switches to the vector function Q8SLT when the search interval extends over less than 500 panels.

After the neighboring panels have been located, the storage locations of the vortices in the neighborhood are simply the combination of the storage locations of the vortices in each of the nine panels. The subdivision process of the previous section reordered the vortices so as to group vortices in the same panel in contiguous storage locations or vectors. As a result, the neighborhood is described by at most nine vectors of vortices, and an additional check is made to identify contiguous vectors which can be described by a single vector. (In particular, the four subpanels of the larger panel containing the considered panel describe a single vector of vortices.) Since the number of vortices per panel is never small, the computations remain efficient on the 205.

The next step in the procedure in Fig. 5 is the evaluation of the original sum in Eq. (2) for panels which are not further subdivided. This sum was split into real and imaginary parts and modified to:

$$u_i = \sum_j g_j \frac{y_j - y_i}{(x_j - x_i)^2 + (y_j - y_i)^2 + d_i^2} \quad (4a)$$

$$v_i = \sum_j g_j \frac{x_j - x_i}{(x_j - x_i)^2 + (y_j - y_i)^2 + d_i^2} \quad (4b)$$

$$g_i = \frac{I_i}{2\pi} \quad (4c)$$

These expressions are equivalent to the original sum in Eq. (2) when the value of 3

//

d_i vanishes. They are equivalent to the sum in Eq. (2) to machine precision when the value of d_i equals the machine epsilon. The addition of the d_i -term in (4a) and (4b) has the advantage of avoiding the singularity in the $i = j$ term while limiting the effect of numerical inaccuracy. For larger values of d_i , the velocity corresponds to vortices with finite core, which tend to improve the numerical properties of a vortex representation [9]. Expressions more elaborate than Eqs. (4a) through (4c) could be used [10]; since they increase the computational time for the original algorithm, they are likely to enhance the relative performance of the present algorithm.

The coefficients of the Laurent series follow from the sum (3b). The coefficients may be split into real and imaginary parts A_k and B_k , leading to the following recursive relationships:

$$a_i^1 = 0, \quad b_i^1 = g_i \quad (5a), (5b)$$

$$a_i^{k+1} = a_i^k(x_i - x_0) - b_i^k(y_i - y_0) \quad (5c)$$

$$b_i^{k+1} = a_i^k(y_i - y_0) + b_i^k(x_i - x_0) \quad (5d)$$

$$A_k = \sum_i a_i^k, \quad B_k = \sum_i b_i^k \quad (5e), (5f)$$

In order to avoid possible inaccuracy caused by underflow of terms, the x - and y -positions were measured from the center of the panel and normalized with half the linear panel dimension.

For the evaluation of the neighborhood of the mother panels in Fig. 5, the Laurent series (3a) is used. Split into real and imaginary parts, the series can be written:

$$U_j^1 = \frac{x_j - x_0}{(x_j - x_0)^2 + (y_j - y_0)^2} \quad (6a)$$

$$V_j^1 = \frac{y_0 - y_j}{(x_j - x_0)^2 + (y_j - y_0)^2} \quad (6b)$$

$$U_j^{k+1} = \frac{U_j^k(x_j - x_0) + V_j^k(y_j - y_0)}{(x_j - x_0)^2 + (y_j - y_0)^2} \quad (6c)$$

$$V_j^{k+1} = \frac{V_j^k(x_j - x_0) - U_j^k(y_j - y_0)}{(x_j - x_0)^2 + (y_j - y_0)^2} \quad (6d)$$

$$u_j = \sum_{k=1} A_k U_j^k - B_k V_j^k \quad (6e)$$

$$v_j = - \sum_{k=1} A_k V_j^k + B_k U_j^k \quad (6f)$$

It can readily be shown that the terms induced by any individual vortex i converge geometrically with a convergence ratio

$$\frac{|t_k|}{|t_{k+1}|} = \left| \frac{Z - Z_0}{Z_i - Z_0} \right| \quad (7)$$

if Z_0 is the position of the center of the panel. Since the vortices in the eight neighboring panels are excluded from the Laurent series, simple geometry shows that the convergence ratio is at least $3/\sqrt{2}$. Therefore, truncating the Laurent series at 22 terms, each vortex would be summed to a relative error $6 \cdot 10^{-8}$, about the machine accuracy in half precision on the CYBER 205.

The last step in the procedure in Fig. 5 is the evaluation of the Laurent series of the current mother panel. While this Laurent series could be found using Eq. (3b), it can be found more efficiently from the Laurent series of the subpanels. The contribution of each of the subpanels to the Laurent series of the mother is given by

$$AC_k = m_k^k C_k + m_{k-1}^k C_{k-1} + \dots + m_1^k C_1 \quad (8a)$$

$$m_k^k = 2^{-k} \quad (8b)$$

$$m_{k-1}^k = m_{k-1}^{k-1} \frac{k-1}{l} \frac{1}{\sqrt{2}} H, \quad (8c)$$

where

$$H = -1 + \sqrt{-1} \quad (8d)$$

$$H = -1 - \sqrt{-1} \quad (8e)$$

$$H = 1 + \sqrt{-1} \quad (8f)$$

$$H = 1 - \sqrt{-1} \quad (8g)$$

for the first through the fourth subpanels, respectively. (The factor 2^{-k} in the above expressions reflects the scaling of Laurent series proportional to the panel size.) The coefficients m_{k-1}^k can be evaluated a priori after which the evaluation of the coefficients vectorizes.

4. PERFORMANCE

The numerical performance of the present algorithm is difficult to analyze in general. In the following, the analysis has been simplified by assuming that the N vortices are homogeneously distributed over a square. In that case, the domain will be subdivided in panels containing the same number of vortices, n , each. The number of unsubdivided panels is N/n and the number of levels of subdivisions needed is $\log_4(N/n)$.

13

The total computational time to find the velocity of the N vortices consists of a number of contributions. First of all, the vortices must be gathered into panels. The first subdivision of the total domain involves N vortices which are first examined on x -position, then on y -position, and correspondingly reordered. The time involved in this step will be written as

$$Nv_G f_{G,N}$$

The factor v_G is the time needed to compare the x - and y -positions of a vortex with those of the center of the panel, pass the vortex 4 times through the vector function Q8VCMPRS (in the 205 implementation, otherwise to store the vortex twice), and add one to the number of vortices in first the right half of the panel and then to the number of vortices in the subpanel, using Q8SCNT.

The penalty factor $f_{G,N}$ expresses the overhead performed which is independent of the number of vortices involved, such as computing and storing the panel information for the four panels and, on the 205, starting up the vector operations. For a large number of vortices, the operations for the individual vortices dominate the total time and $f_{G,N}$ will approach unity. However, for vector processors such as the 205, the vector operations for the individual vortices are performed with such a speed that $f_{G,N}$ becomes appreciable when the number of vortices becomes less than a few hundred. (For the simple vector operations in half precision on the FSU/DOE 205, the start-up overhead becomes equivalent to the time of execution when the number of vortices is 200). The subscript N in the penalty factor $f_{G,N}$ expresses the representative number of elements or vector length.

In the next level of subdivision, four panels with each $\frac{1}{4}N$ vortices are subdivided, requiring a computational time

$$\frac{1}{4}Nv_G f_{G,N/4} \cdot 4 = Nv_G f_{G,N/4}$$

Since there are $\log_4(N/n)$ levels of subdivisions and the penalty factor increases with decreasing vector length, the total time for finding the panels may conservatively be written as:

$$t_G = Nv_G f_{G,n} \log_4 \left(\frac{N}{n} \right) \quad (9a)$$

The logarithmic factor may be bounded by the maximum number of subdivisions allowed by the machine accuracy [8], but such a bound depends on the particular coding techniques and machine accuracy available and will be avoided here.

In the present algorithm, the original sum in Eq. (2) is used to evaluate the velocity induced by the n vortices in each unsubdivided panel upon its neighborhood of nine panels. If v_z is the time needed to evaluate a single term in Eq. (2), the total time can be written, conservatively, as

$$t_z = n \cdot 9n \cdot v_z f_{z,n} \frac{N}{n} \quad (9b)$$

neglecting panels that may fall outside the domain, or

$$t_s = 9n \left[1 - \frac{4}{3} \sqrt{\frac{n}{N}} + \frac{4}{9} \frac{n}{N} \right] v_s f_{s,n} N,$$

after correction. Since n will typically be sizably smaller than N , Eq. (9b) will be used.

For each of the unsubdivided panels, K coefficients of the Laurent series (3b) must be determined, requiring a time

$$t_c = n \cdot K \cdot v_c \cdot f_{c,n} \cdot \frac{N}{n}. \quad (9c)$$

These Laurent series are next used to determine the velocity induced on the $4 \cdot 9n$ vortices in the neighborhood of the larger panel containing the unsubdivided panel, excluding the $9n$ vortices in the neighborhood of the unsubdivided panel itself. The time needed for N/n unsubdivided panels is

$$K \cdot 27n \cdot v_L \cdot f_{L,n} \cdot \frac{N}{n}.$$

Similarly, the Laurent series for the $N/4n$ larger panels are used to evaluate the velocity induced upon $27 \cdot 4n$ vortices, neglecting edge effects. With $\log_4(N/4)$ levels of subdivision, the time can be written conservatively as:

$$t_L = K \cdot 27n \cdot v_L \cdot f_{L,n} \cdot \frac{N}{n} \log_4 \left(\frac{N}{n} \right). \quad (9d)$$

The procedure of Greengard and Rokhlin [7] avoids the logarithmic factor, since the number of coefficients in the Taylor series does not increase with panel size. However, the logarithmic factor in (9a) would remain.

Time is further needed to combine the Laurent series of the unsubdivided panels into these of the larger panels. In the 205 implementation, each coefficient C_k of the larger panel was written as an inner product between the vector of $4K$ coefficients of the subpanels and a corresponding vector of coefficients m_l^k , Eqs. (8a) through (8g). The time needed is:

$$t_l = \frac{4}{3} \frac{K^2}{n} v_l f_{l,4K} N. \quad (9e)$$

The contribution most difficult to estimate is the overhead involved in addressing the panel structure. For each panel, the neighborhood needs to be established, as well as the neighborhood of the next larger panel. Most of the operations involved will roughly be proportional to the number of panels: N/n unsubdivided ones, $N/4n$ next larger ones, and so on, a total of less than $4N/3n$ panels. However, the binary

search to find the nine neighboring panels requires operations proportional to $\log_2(4N/3n)$. The time for overhead will therefore be written as

$$t_0 = \left[\frac{4}{3} s_0 + \frac{8}{3} s_r \log_2 \left(\frac{N}{n} \right) \right] \frac{N}{n}, \quad (9f)$$

where s_0 and s_r are representative computational times for each panel and for each binary search, respectively, neglecting $\log_2 4/3$. The symbol s was used here instead of v in order to indicate that the operations involved are largely scalar.

Using these various contributions to the computational time, the decision when to stop subdivision of the panels can be addressed. Collecting all contributions, the total time needed to find the velocity becomes:

$$t = \left(v_G f_{G,n} + 27 v_L f_{L,n} K + \frac{8}{3} \frac{s_r}{n} \right) N \log_2 \frac{N}{n} + \left(9 v_\Sigma f_{\Sigma,n} n + v_C f_{C,n} K + \frac{4}{3} v_I f_{I,4K} \frac{K^2}{n} + \frac{4}{3} \frac{s_0}{n} \right) N. \quad (10)$$

In estimating the relative importance of the terms, it will be assumed that the number of vortices N is large. Indeed, the number of vortices must be sizably larger than the typical number of terms in the Laurent series in order for the algorithm to be useful.

Under the limiting process where both N and the number of vortices per panel n tend to infinity, corresponding to relatively few large panels, the dominant term in Eq. (10) is the time, Eq. (9b), for the original sum, as could be expected. Since this term is proportional to n , decreasing the number of vortices per panel leads to corresponding reductions in computation time.

However, when decreasing the number of panels, adverse affects must eventually occur. The penalty factor $f_{\Sigma,n}$ increases when the value of n decreases, since the start up time increases in relative importance. On a two pipe 205, the vector start up becomes dominating when the number of vortices becomes less than 200, limiting further reductions in the time needed for the original sum.

On the other hand, the time needed for other operations increases while n decreases. For example, the time for doing the Laurent series (9d) increases when n decreases below a certain limit, since the penalty factor increases. This term contains the relatively large numerical factor $27K$, so that appreciable increases in the penalty factor tend to be important. In addition, the scalar times, which can be relatively large on a 205, are inversely proportional to n .

It may be concluded that for sufficiently many vortices, the computational time first decreases with the number of vortices per panel and then increases. As a result, a number of vortices per panel exists for which the present algorithm performs optimally.

For that reason, in generating the panels, the present algorithm decides whether 75

to subdivide panels further based on the number of vortices in the panel. Further subdivisions are only made when the number of vortices is greater than some minimum value n , chosen a priori.

Table I provides examples of the influence of the value of n on the computational time. In this case, the vortices were approximately homogeneously distributed over the interior of a circle, grouped in rings. It appears from Table I that the minimum number of vortices to subdivide a panel on a 205 should be roughly 200. Fortunately, the precise value used appears to have relatively little influence on the results.

In addition to the computational time, the numerical errors in the algorithm are important. For p vortices of strength Γ located on a ring of radius R , the velocity induced is

$$V_j^* = \sqrt{-1} \frac{p\Gamma}{2\pi Z_j} \frac{Z_j^p}{Z_j^p - R^p}$$

TABLE I
Computational Time and Numerical Errors for Vortices Homogeneously Distributed
within a Circle Using 23 Term Asymptotic Expansions

Number of vortices	1000	2000	4000	8000	16,000	32,000	64,000
Time for summation, CPU seconds							
Original	0.10	0.36	1.38	5.39	21.35	86.32	356.78
100	0.11	0.35	0.71	1.95	3.55	9.35	17.17
200	0.11	0.27	0.67	1.61	3.55	8.12	17.10
400	0.10	0.27	0.82	1.61	4.58	8.12	22.53
Ratio of improvement							
200	0.9	1.3	2.0	3.3	6.0	10.6	20.9
Maximum error in the velocity, percent							
Original	0.005	0.019	0.020	0.040	0.080	0.160	0.319
100	0.004	0.007	0.009	0.013	0.016	0.022	0.024
200	0.004	0.006	0.009	0.013	0.016	0.021	0.024
400	0.005	0.006	0.012	0.043	0.021	0.021	0.030
Mean square error in the velocity, percent							
Original	0.003	0.006	0.012	0.023	0.046	0.093	0.187
200	0.002	0.004	0.005	0.007	0.009	0.012	0.013
Average error in the velocity, percent							
Original	0.003	0.005	0.010	0.020	0.041	0.082	0.164
200	0.002	0.003	0.005	0.006	0.008	0.010	0.012

6

17

or

$$V_j^* = \sqrt{-1} \frac{(p-1)\Gamma}{4\pi Z_j}$$

if the vortex j is located on the same ring. By summation over all rings the analytical solution can be found and compared to the obtained results.

Table I list the maximum deviation in either velocity component from the analytical solution, expressed in a percentage of the velocity at the perimeter of the circle. The present algorithm shows considerably better accuracy than the original sum, which may be due to the summation of the terms in groups. In the original algorithm, the individual terms were added to an increasingly large total, leading to a loss of significant digits.

For random walk computations, the mean square or average errors may be more relevant than the maximum error, since only averaged quantities are relevant. Both these errors show behavior similar to the maximum error.

TABLE II
As Table I, but Using 13 Term Expansions

Number of vortices	1000	2000	4000	8000	16,000	32,000	64,000
Time for summation, CPU seconds							
Original	0.10	0.36	1.38	5.39	21.36	86.35	356.72
100	0.09	0.26	0.57	1.40	2.79	6.61	13.03
200	0.09	0.25	0.55	1.07	2.79	6.91	13.08
400	0.10	0.25	0.79	1.43	4.27	6.92	20.40
Ratio of improvement							
100	1.1	1.4	2.4	3.9	7.7	13.1	27.4
Maximum error in the velocity, percent							
Original	0.005	0.010	0.020	0.040	0.080	0.160	0.319
100	0.003	0.005	0.007	0.009	0.011	0.013	0.015
200	0.003	0.006	0.007	0.011	0.011	0.016	0.015
400	0.005	0.006	0.011	0.012	0.019	0.016	0.025
Mean square error in the velocity, percent							
Original	0.003	0.006	0.012	0.023	0.046	0.093	0.187
100	0.002	0.003	0.004	0.005	0.006	0.007	0.009
Average error in the velocity, percent							
Original	0.003	0.005	0.010	0.020	0.041	0.082	0.164
100	0.002	0.002	0.003	0.004	0.005	0.006	0.008

18

The results in Table I were obtained by expanding all Laurent series to machine precision, 23 terms. Yet in view of the final errors in the results, there appears little justification in demanding such accuracy, unless special provisions are made to avoid accumulation of the round-off errors. Results for 13 term Laurent series are presented in Table II. Remarkably, the resulting errors prove somewhat lower than those in the 23 term expansion. A good explanation of this effect cannot be given; however, the maximum possible error in truncating the Laurent series is only 0.006%, small compared to the final errors. On the other hand, the final terms in the Laurent series correspond to the fastest Fourier components: for that reason truncating the series may have some averaging effect on the round-off errors.

For the case of Tables I and II, the vorticity occupied most of the domain under consideration. A somewhat different case arises when the vortices are evenly spaced along the perimeter of a circle. Since the vorticity is now sparsely distributed, the present procedure will generate a considerable number of empty panels, and it

TABLE III
Computational Time and Numerical Errors for Vortices Homogeneously
Distributed on a Circle Using 13 Term Asymptotic Expansions

Number of vortices	1000	2000	4000	8000	16,000	32,000	64,000
Time for summation, CPU seconds							
Original	0.10	0.36	1.38	5.41	21.38	86.32	356.75
50	0.08	0.17	0.36	0.78	1.65	3.53	7.30
100	0.06	0.14	0.31	0.65	1.42	3.04	6.28
200	0.06	0.17	0.34	0.75	1.51	3.36	7.19
Ratio of improvement							
100	1.7	2.6	4.5	8.3	15.1	28.4	56.8
Maximum error in the velocity, percent							
Original	0.024	0.061	0.128	0.271	0.547	1.100	—
50	0.012	0.023	0.046	0.093	0.180	0.360	0.702
100	0.012	0.024	0.046	0.094	0.181	0.361	0.702
200	0.013	0.026	0.049	0.098	0.184	0.363	0.705
Mean square error in the velocity, percent							
Original	0.005	0.010	0.018	0.041	0.079	0.143	—
100	0.004	0.008	0.012	0.031	0.059	0.096	0.149
Average error in the velocity, percent							
Original	0.001	0.002	0.003	0.006	0.012	0.024	—
100	0.000	0.001	0.001	0.001	0.002	0.002	0.002

107

might seem that this would adversely affect computational time. However, the data in Table III shows that performance improves. This appears to agree with the observations of Carrier, Greengard, and Rokhlin [8].

The simplified case of vortices arranged on a single horizontal line can shed some light on this increase in efficiency. Repeating the previous analysis with suitable modifications, the total time becomes:

$$t = \left[2v_G f_{G,n} + 6v_L f_{L,n} K + 8 \frac{s_1}{n} \right] N \log_4 \frac{N}{n} + \left[3v_E f_{E,n} n + v_C f_{C,n} K + 4v_I f_{I,n} \frac{K^2}{n} + 4 \frac{s_0}{n} \right] N. \quad (12)$$

Comparison with Eq. (10) does show that the time for scalar panel overhead has increased. On the other hand, the time needed for the direct summation has improved, since the empty panels decrease the number of vortices in the neighborhood of unsubdivided panels from $9n$ to $3n$. In addition, the time for the Laurent series has decreased, since $6n$ rather than $27n$ vortices need to be

TABLE IV
Computational Time and Numerical Errors for Vortices
on the Perimeter of a Circle for a MicroVAX II

Number of vortices	400	800	1600	3200	6400	12,800	25,600
Time for summation, CPU seconds							
Original	9.1	36.3	151.9	614.2	2470.8	9867.3	39469.2
30	5.0	10.9	24.5	56.3	127.0	272.3	604.1
40	4.7	10.6	25.1	55.4	128.5	286.3	597.8
50	4.7	10.6	25.0	55.5	133.5	292.5	616.3
60	4.7	10.6	26.4	55.7	138.9	303.3	635.6
Mean square error in the velocity, percent							
Original	0.00000	0.00000	0.00001	0.00004	0.00007	0.00019	0.00036
40	0.00001	0.00001	0.00001	0.00002	0.00004	0.00010	0.00018
Additional array storage used, 4 byte words							
40	496	3289	3907	5040	7281	11374	20827
Percentage CPU time for various steps							
t_G	62	50	48	43	42	41	34
t_L	30	14	8	9	9	7	7
t_E	0	26	34	38	40	43	50

determined from the Laurent series of the unsubdivided panels; the remaining contributions are found using the combined Laurent series.

Next, while scalar operations are relatively slow on the 205, the corresponding total times are proportional to $1/n$, which is of order 10^{-2} . On the other hand, the times for the direct sum and the Laurent series are proportional to $9n$ and $27K$, respectively, which are of order 10^2 . For that reason, the scalar times need not dominate even for quite slow scalar processing.

While the present algorithm still leads to reduced errors, the differences are not so pronounced as in Tables I and II. The reason may be that in this case the vortices in the immediate vicinity of each other dominate the errors (the sum approximates a singular integral). Those vortices are still summed in the same way as in the original algorithm.

Table IV shows computational times for a scalar version of the algorithm. As may be expected, the scalar version can address smaller groups of vortices more efficiently than the 205 version, resulting in some additional savings.

The total time CPU time used can be divided into contributions t_0 to perform the original sum (2), t_{L_1} to perform the Laurent series of panels which are not further subdivided, and t_{L_2} for the Laurent series of panels which are. Table IV shows those contributions for the case that $n = 40$. Recasting of Laurent series into Taylor series as used by Greengard and Rokhlin [7] could be used to reduce the required time t_{L_2} .

Comparison of Table IV with the data of Carrier, Greengard, and Rokhlin [8] does suggest a significant increase in storage due to such a recasting.

5. CONCLUDING REMARKS

The present algorithm is concerned with fast solution of the 2-dimensional Poisson equation under pointwise forcing. Since the actual application is not the true subject of this paper, or a concise description of the one considered here will be given: Lagrangian flow computations using a random walk simulation of diffusion effects similar to [9]. A relatively simple removal of the singular behavior, Eq. (4), was used in computed examples such as Fig. 1. In most computations, the chosen vortex diameter was 0.675 times the random step size $\sigma = \sqrt{2\nu \Delta t}$. The normal boundary condition was satisfied by means of mirror vortices within the cylinder. To satisfy the tangential boundary condition, after each predictor-corrector step all vortices within a distance 1.27σ from the wall, a thin sub-layer of the boundary layer, were removed. Next the slip velocity at the wall was evaluated and integrated to find the amount of circulation needed to satisfy the no-slip condition. This circulation was subsequently assigned to a ring of vortices a distance 0.675σ away from the wall and spaced 1.27σ apart. The procedure leads to the same flux of vortices through the cutoff at 1.27σ as a homogeneous distribution of vortices within the cutoff. In order to reduce the random fluctuations introduced by strong vortices, the number of vortices placed at each location along the wall was chosen 20

to give an approximately uniform vortex strength. At least one vortex was placed at each location if the local circulation was non-zero. Some experiments varying the given numerical values, or using an exponential vortex core rather than Eq. (4), were performed, but results were ambiguous due to the random noise. The random step sizes were taken from a data base of 8000 random numbers, starting from a randomly chosen position.

The purpose of this paper was to show how the computational time can be greatly reduced using Laurent series, allowing a much larger number of vortices to be included. The use of Laurent series or replacement elements to save computational time is not a new notion [6]; however, the present method renders the application effective by gathering the point forces into an adaptive, ordered panel structure. The contribution of the present paper is therefore primarily a programming technique which allows an easily addressable adaptive description of irregular distributions of points. Moreover, it is quite suited for vector processing and requires little storage. It seems simpler and possibly more vectorizable than the procedure of Carrier, Greengard, and Rokhlin [8].

The evidence of the Tables I through IV shows that the present algorithm is "fast" in the sense that the computational time roughly doubles when the number of vortices doubles. For the original sum in Eq. (2), the computational time becomes larger by a factor four instead. For that reason the savings in computational time increase with the number of vortices.

In fact, the time estimates in Eqs. (10) and (12) show the computational time to be proportional to $N \log N$, similar to the fast Fourier transform solutions of the Poisson equation such as Hockney's FACR algorithm, which needs $N \log_2(\log_2 N)$ operations. However, a closer study of Eqs. (10) and (12) shows that for typical values $K \sim 20$ and $n \sim 100$, the coefficient of the $N \log N$ term in the present algorithm will be numerically quite large.

For that reason, one of the motivations mentioned in the Introduction should still be present in order to adopt an algorithm such as the present one.

An interesting question is whether the present algorithm is applicable to 3-dimensional Poisson problems. This would make it possible to address such problems as the motion of stars in galaxies and 3-dimensional flows with sparse vortex geometry. Most of the procedures in Sections 2 and 3 carry through immediately by the simple step of including the digits of the third coordinate in the panel numbers. However, the straightforward generalization of the Laurent series to spherical harmonics as applied by Greengard and Rokhlin [11] has the disadvantage that the number of terms added for each order of accuracy increases. A procedure based on fast Fourier transforms proposed by Greengard and Rokhlin [12] can significantly reduce the effort.

The present procedure of generating and addressing a complex panel structure does not need to be restricted to solution of the Poisson equation, but could be used for other problems involving groups of points in which the interaction between elements of different groups can be simplified when the distance between the groups is sufficient.

ACKNOWLEDGMENTS

The authors acknowledge the support of the Supercomputer Computations Research Institute and the Florida State University through use of its 205. During parts of this investigation, the first author was supported by NASA Ames and the AFOSR, and the second author by the SCRI.

REFERENCES

1. A. LEONARD, *Annu. Rev. Fluid Mech.* 17, 523 (1985).
2. C. R. ANDERSON, *J. Comput. Phys.* 62, 111 (1986).
3. A. W. APPEL, *SIAM J. Sci. Stat. Comput.* 6, 85 (1985).
4. J. BARNES AND P. HUT, *Nature* 342, 446 (1986).
5. L. L. VAN DOMMELIN AND E. A. RUNDENSTEINER, "Adaptive-panel vortex summation for the CYBER 205," 38th Annual Meeting of the Division of Fluid Dynamics of the American Physical Society, Nov. 22-24, 1985.
6. V. ROKHLIN, *J. Comput. Phys.* 60, 187 (1985).
7. L. GREENGARD AND V. ROKHLIN, *J. Comput. Phys.* 73, 325 (1987).
8. J. CARRIER, L. GREENGARD, AND V. ROKHLIN, Yale University, Department of Computer Science Report No. YALEU/DCS/RR-496, 1987; *SIAM J. Sci. Stat. Comput.* 9, No. 4 (1988).
9. A. J. CHORIN AND P. S. BERNARD, *J. Comput. Phys.* 37, 423 (1973).
10. J. T. BEALE AND A. J. MAJDA, *J. Comput. Phys.* 58, 188 (1984).
11. L. GREENGARD AND V. ROKHLIN, Yale University, Department of Computer Science Report No. YALEU/DCS/RR-515, 1987 (unpublished).
12. L. GREENGARD AND V. ROKHLIN, Yale University, Department of Computer Science Report No. YALEU/DCS/RR-602, 1988 (unpublished).

AUTHOR: Please complete before returning proofs
Read and Corrected by <i>L. Greengard</i>
<i>5/19/89</i>
(Date)

APPENDIX III
Summary of the Computational Scheme.

4

Computations

Random-walk vortex simulations of the full Navier-Stokes equations were performed as comparison. In the computations, the flow field was represented by discrete vortex blobs of the form:

$$u_j = \sum_i g_i \frac{y_j - y_i}{(x_j - x_i)^2 + (y_j - y_i)^2 + d_i^2}$$
$$v_j = \sum_i g_i \frac{x_i - x_j}{(x_j - x_i)^2 + (y_j - y_i)^2 + d_i^2}$$
$$g_i = \frac{\Gamma_i}{2\pi}$$

A recently developed fast procedure allowed the computations to be performed with sizably more vortex blobs than previously possible [see J. Comp. Phys. paper]. The vortices were advanced in time using a two-step Runge-Kutta scheme. To simulate diffusion effect, each time step the vortex motion was augmented with a random component of average magnitude $\sqrt{2\nu\Delta t}$

The normal wall boundary condition was satisfied by mirror vortices, after a mapping of the airfoil onto a circle. The mapping used was a generalized Von Mises transform which correctly reproduces the kinks in the contour at the trailing edge:

$$\frac{dZ}{d\zeta} = C \prod_{k=1}^K \left(1 - \frac{\zeta_k}{\zeta}\right)^{\gamma_k}$$

The constants C , ζ_k and γ_k are determined from: the kinks in the NACA 0012 airfoil contour caused by the small but finite thickness at the trailing edge, the regularity of the mapping at infinity, and finally from least square minimization of the errors in airfoil shape elsewhere. The Von Mises type procedure was preferred above a Fast Fourier transform, since the transform is relatively inaccurate due to the singularities in contour. In addition, the transform would be quite inefficient during the actual flow computation.

The no-slip boundary condition was satisfied by addition of vortices at the wall during each time-step: First all vortices within a distance of $1.27\sqrt{2\nu\Delta t}$ were removed. Then a ring of new vortices was added at a distance $0.675\sqrt{2\nu\Delta t}$ to correct the wall velocity to zero. (The distance for adding vortices equals the diffusion distance of the vorticity generated by the wall during the time-step for the true Navier-Stokes equations; the removal distance

was chosen based on a statistical study requiring that the scheme handles locally uniform vorticity distributions accurately, not unlike discretization techniques in finite difference procedures). The vortex diameter d_i was rather arbitrarily chosen to be $0.675\sqrt{2\nu\Delta t}$; testing showed that results depended little on the actual value used.

The CYBER 205 results were post-processed on the departmental MicroVAX II, using a fast Fourier transform to find the streamlines. The vorticity was represented in bit-mapped graphics as half tones.

APPENDIX IV

On the Lagrangian Description of Unsteady Boundary-Layer Separation. Part I: General Theory, Journal of Fluid Mechanics Paper.

**ON THE LAGRANGIAN DESCRIPTION OF UNSTEADY
BOUNDARY-LAYER SEPARATION. PART I: GENERAL THEORY.**

by

Leon L. Van Dommelen
Department of Mechanical Engineering
FAMU/FSU College of Engineering
Tallahassee, Florida 32304, U.S.A.

and

Stephen J. Cowley
Department of Mathematics
Imperial College of Science, Technology and Medicine
Huxley Building, 180 Queen's Gate
London SW7 2BZ, U.K.

(PAGE 1)

Abstract

Although unsteady, high-Reynolds-number, laminar boundary layers have conventionally been studied in terms of Eulerian coordinates, a Lagrangian approach may have significant analytical and computational advantages. In Lagrangian coordinates the classical boundary-layer equations decouple into a momentum equation for the motion parallel to the boundary, and a hyperbolic continuity equation (essentially a conserved Jacobian) for the motion normal to the boundary. The momentum equations, plus the energy equation if the flow is compressible, can be solved independently of the continuity equation. Unsteady separation occurs when the continuity equation becomes singular as a result of touching characteristics, the condition for which can be expressed in terms of the solution of the momentum equations. The solutions to the momentum and energy equations remain regular. Asymptotic structures for a number of unsteady three-dimensional separating flows follow and depend on the symmetry properties of the flow (e.g. line symmetry, axial symmetry). In the absence of any symmetry, the singularity structure just prior to separation is found to be quasi two-dimensional with a displacement thickness in the form of a crescent shaped ridge. Physically the singularities can be understood in terms of the behavior of a fluid element inside the boundary layer which contracts in a direction parallel to the boundary and expands normal to it, thus forcing the fluid above it to be ejected from the boundary layer.

1. Introduction

A major feature of unsteady large-Reynolds-number flow past a rigid body is the shedding of vortices from the surface of the body. Such vortices alter the forces exerted on the body dramatically (McCroskey & Pucci 1982). A more complete theoretical understanding of vortex shedding would be advantageous in the design of air, land and water transport. Theoretical models of vortex shedding also have application, *inter alia*, in the description of air flow over hills and water waves, water flow over sand ripples, and blood flow through curved and constricted arteries and veins.

A classical example of vortex shedding develops when a circular cylinder is set into motion in the direction normal to its axis. This example was first studied by Prandtl (1904), and the process by which an initially attached boundary layer develops into a separated flow

with detached free shear layers has been clearly illustrated by the experiments of Nagata, Minami & Murata (1979), and Bouard & Coutanceau (1980). The term 'separation' will in this paper be used to refer to the 'breakaway' of a thin layer of vorticity from the surface of a body. This definition of separation is close to that of both Prandtl (1904) and Sears & Telionis (1975). In particular, Sears & Telionis speak only of separation when the penetration of the boundary-layer vorticity away from the wall becomes too large to be described on the usual $O(Re^{-\frac{1}{2}})$ boundary-layer scale (Re is the Reynolds number of the flow, and is assumed large). Therefore, once separation has developed the classical attached flow solution will, in general, no longer be valid.

The first theoretical advance in understanding the unsteady cylinder flow at high Reynolds numbers was made by Blasius (1908). He explained the occurrence of flow reversal inside the attached unsteady boundary layer which is set up immediately the cylinder starts to move. In the case of steady flow past a rigid surface, flow reversal is often accompanied by separation. However, Moore (1958), Rott (1956) and Sears (1956) all realized that zero wall shear is not necessarily related to separation in unsteady flow. Sears & Telionis (1975) noted subsequently that their definition of separation is consistent with the termination of the boundary-layer solution in a singularity. Such a singularity will be referred to as the separation singularity, and the time at which it develops as the separation time.

A considerable number of numerical computations have attempted to verify the existence of a singularity in the boundary-layer solution for the circular cylinder problem. The first convincing evidence that a singularity forms within a finite time was given by Van Dommelen & Shen (1977, 1980a, 1982). In a Lagrangian computation, with fluid particles as independent coordinates, they found that a separation singularity develops after the cylinder has moved approximately $\frac{3}{4}$ of a diameter. The existence of this singularity has been confirmed by the finite difference numerical calculations of Ingham (1984) and Cebeci (1982) (however see Cebeci, 1986), and the computer extended series solution of Cowley (1983). These calculations were all based on Eulerian formulations. A similar two-dimensional separation singularity has been observed using Lagrangian procedures on an impulsively started ellipse at several angles of attack (Van Dommelen, Wu, Chen & Shen, unpublished results), on airfoils (Wu 1988), in turbulence production (Walker 1988),

on an impulsively started sphere (Van Dommelen 1987), and using Eulerian schemes in leading edge stall (Cebeci, Khattab & Schimke, 1983) and about a rotating cylinder (Ece, Walker & Smith, 1984).

Excluding vortex methods, flows with free surfaces, and some more specialized compressible flow computations, Lagrangian coordinates have not been as widely used as their Eulerian counterparts in fluid mechanics, especially for boundary-layer flows. Yet for some flows, such as unsteady flows in which advection dominates diffusion, Lagrangian coordinates seem more appropriate (e.g. see the inviscid calculations of Stern & Paldor (1983), Russell & Landahl (1984) and Stuart (1987)). As far as unsteady separation is concerned, the advantage of a Lagrangian approach stems from the fact that in these coordinates the classical boundary-layer equations decouple into a momentum equation for the motion parallel to the boundary, and a continuity equation for the motion normal to the boundary (Shen 1978). The solution of the former equation can be found independently of the latter. Moreover, while the time that the separation singularity develops can be identified from the solution to the momentum equation, only the solution to the continuity equation is singular (see section 2).

An important consequence of the Lagrangian approach is that simple descriptions can be found to a wide variety of separations in one-, two- and three-dimensional unsteady flows. In this paper we consider unsteady flows in general, then in part 2, (Van Dommelen 1989), the separation process that occurs at the equatorial plane of a sphere which is set into a spinning motion is examined in detail.

In the next section we develop the simple analytic machinery needed to find self-consistent three-dimensional separation structures for both compressible and incompressible fluids. Some of the properties of the Lagrangian version of the boundary-layer equations are also discussed. In section 3 the Lagrangian structure for three-dimensional separation is derived under the assumption that the flow can be completely general, then in section 4 the changes in structure are discussed when various symmetries restrict the flow geometry.

2. Lagrangian Formulation

The Lagrangian description of boundary-layer flow uses fluid particles (i.e. infinitesi-

mal masses of fluid) as the basis of the coordinate system. A convenient coordinate system for the fluid particles (ξ, η, ζ) is given by the initial Eulerian position of the particles (see Lamb (1945) for example):

$$\xi \equiv (\xi, \eta, \zeta) = (x, y, z) \quad \text{at } t = 0 \quad . \quad (2.1)$$

The precise form of the Lagrangian solution depends on the particular reference time, defined here as the start of the motion, but the physical solution is independent of it.

Following Rosenhead (1963) we assume that the position coordinates x and z describe an orthogonal coordinate system on the surface of the body in question. The lengths of the line elements dx and dz are taken as $h_1 dx$ and $h_3 dz$ respectively. The coordinate normal to the surface is denoted by y , which is scaled with the square root of the reference shear viscosity.

In Lagrangian coordinates, conservation of volume for a compressible fluid can be expressed in terms of a Jacobian determinant as follows (e.g. Hudson 1980):

$$\rho H(x, z) J(x, y, z) = \rho_0 H_0 \quad , \quad (2.2a)$$

where

$$J(x, y, z) = \begin{vmatrix} x, \xi & x, \eta & x, \zeta \\ y, \xi & y, \eta & y, \zeta \\ z, \xi & z, \eta & z, \zeta \end{vmatrix} \quad , \quad \rho_0(\xi, \eta, \zeta) = \rho(\xi, \eta, \zeta, 0) \quad , \quad (2.2b, c)$$

$$H(x, z) = h_1(x, z) h_3(x, z) \quad , \quad H_0 = H(\xi, \zeta) \quad , \quad (2.2d, e)$$

$\rho(\xi, \eta, \zeta, t)$ is the density of the fluid, and a subscript comma denotes a Lagrangian derivative. The velocity components of the flow are related to the fluxions of position by

$$u = h_1(x, z) \dot{x} \quad , \quad w = h_3(x, z) \dot{z} \quad , \quad (2.3a, b)$$

where a dot represents a Lagrangian time derivative.

For compressible flow, the momentum and energy equations are (e.g. Rosenhead 1963):

$$\rho(\dot{u} + (u h_{1z} - w h_{3z}) \frac{w}{H}) = -\frac{1}{h_1} p_x + D_y(\mu D_y u) + \rho g_x \quad , \quad (2.3c)$$

$$\rho(\dot{w} + (w h_{3z} - u h_{1z}) \frac{u}{H}) = -\frac{1}{h_3} p_z + D_y(\mu D_y w) + \rho g_z \quad , \quad (2.3d)$$

$$\rho \frac{\partial e}{\partial \rho} \dot{\rho} + \rho \frac{\partial e}{\partial p} \dot{p} - \frac{p}{\rho} \dot{\rho} = \mu((D_y u)^2 + (D_y w)^2) + D_y \left(\frac{\mu}{\sigma} D_y T \right) \quad , \quad (2.3e)$$

where μ is the scaled shear viscosity, σ is the Prandtl number, and g_x and g_z are the components of the acceleration of gravity. The temperature, T , and internal energy e , are assumed to be functions of density and pressure, while the pressure, p , is a known function of x , z and t ; thus

$$\dot{p} = p_t + \frac{u}{h_1} p_x + \frac{w}{h_3} p_z \quad . \quad (2.3f)$$

For an incompressible flow $\dot{\rho} = 0$ and e is taken to be a function of T and p .

Although the y -derivative D_y is Eulerian in nature, it can be written in the Lagrangian form (see also Shen 1978):

$$D_y u = \frac{\rho(\xi, \eta, \zeta, t) H(x, z) J(x, u, z)}{\rho_0(\xi, \eta, \zeta) \bar{H}(\xi, \zeta)} \quad . \quad (2.4)$$

From (2.4) it follows that at a fixed wall the Eulerian D_y and Lagrangian $\partial/\partial\eta$ operators differ only by the density ratio, which leads to simplifications in the calculation of the wall shear.

Allowing for a moving boundary, appropriate boundary conditions to (2.3) are:

$$(u, w, \rho) = (u_b(x, z, t), w_b(x, z, t), \rho_b(x, z, t)) \quad \text{on} \quad y = 0 \quad , \quad (2.5a)$$

$$(u, w, \rho) \rightarrow (u_e(x, z, t), w_e(x, z, t), \rho_e(x, z, t)) \quad \text{as} \quad y \rightarrow \infty \quad , \quad (2.5b)$$

where u_b and w_b specify the velocity of the boundary in the x - and z -directions respectively, u_e and w_e are the corresponding external slip-velocities, ρ_e is the external flow density, and the wall density ρ_b can be given implicitly as the temperature at the wall. Ordinarily, these boundary conditions translate immediately to the Lagrangian domain by means of (2.3a,b). In the case of suction or blowing through the wall, they must be applied at an η -boundary moving through the Lagrangian domain, however, the wall boundary conditions turn out to be of little importance for the local analysis of this paper.

The principle advantages of Lagrangian coordinates derive from the absence of both the normal particle position y and the normal velocity component v from (2.3) and (2.4). Consequently, the particles' motion, as projected onto the surface of the body (x, z), can be found independently of the normal particle position y . Subsequent integration of the

Jacobian (2.2) along lines of particles at constant projected position (x, z) yields the normal particle position

$$y = \int_0^s \frac{\rho_0 H_0 ds}{\rho H |\nabla x \wedge \nabla z|} , \quad (2.6)$$

where $ds^2 = d\xi^2 + d\eta^2 + d\zeta^2$, $\nabla x = (x_{,\xi}, x_{,\eta}, x_{,\zeta})$ is the Lagrangian gradient, and the integral is performed in the Lagrangian $(\xi, \eta, \zeta; t)$ coordinate system along the lines of constant x, z , and t , i.e. lines which in physical space are vertical through the boundary layer.

The central issue of this paper can now be stated: we hypothesize that during the evolution toward separation, the projected position (x, z) can remain regular, and commonly does remain regular. When true, such regularity strongly restricts the possible behavior of x and z near separation, and to characterize separation we need only identify the nature of solutions to the continuity equation (2.2) or (2.6) - an equation which is much simpler than the momentum equations. The remaining ambiguity in the behavior of x and z is resolved using arguments of symmetry.

Various arguments to justify our hypothesis can be given. One of them is self-consistency. If it is assumed that x, z, u, w , and ρ are non-singular at the separation time t_s , then the solution to the Lagrangian momentum equations can be expanded in powers of $(t - t_s)$ to any algebraic order. In contrast, the usual Eulerian asymptotic expansions show only that the first few terms in the expansions are self-consistent.

As another argument, Van Dommelen (1981) showed analytically that the *inviscid* incompressible two-dimensional equations have solutions, x, z , which are regular functions of the Lagrangian variables, although $y(\xi, t)$ is singular (this analysis can be further developed by expanding in powers of a small coefficient of viscosity). Yet this example is somewhat artificial; physically it would require that during the evolution of the boundary layer the coefficient of viscosity was changed significantly by some external means.

A more powerful argument is possibly the capability of the analysis in this paper to reproduce and extend several known separation processes previously analyzed in Eulerian coordinates. However, the most convincing argument is provided by actual numerical solutions of the Lagrangian boundary-layer equations. For example, Van Dommelen & Shen's (1980a) computation of the boundary layer on an impulsively started circular cylinder

provided direct numerical evidence as to regularity of the momentum equation. Further, it is in remarkably close agreement with the results obtained by Cowley (1983) using a series extension technique. In particular, Cowley (1983) finds a singularity in the solution at the same time and position as the Lagrangian computations. Ingham (1984) performed an Eulerian Fourier series expansion of the solution in the direction along the cylinder. By carefully increasing the order of expansion as the spectrum expands due to the incipient singularity, he obtained results in close agreement with those of both Van Dommelen & Shen (1980a) and Cowley (1983). The fact that these three very different procedures were found to produce results in excellent agreement with one another until very close to the breakdown of the solution at separation is reassuring, since a number of more conventional finite difference computations (e.g. Telionis & Tsahalis (1974), Wang (1979), Cebeci (1986)) give significantly different results. Yet the results of Henkes & Veldman (1987) remain in agreement with the three unconventional methods until relatively close to the singularity, but disagree with Cebeci (1986) at a significantly earlier time. One of the difficulties with conventional finite difference procedures, as pointed out by Cebeci (1986), is the need to satisfy the CFL condition, a condition which is implicitly satisfied by the three procedures of Van Dommelen & Shen, Cowley and Ingham.

Clearly in any numerical Lagrangian computations, it is not possible to *prove* that the solution is regular, since the inevitable upper limit on resolution means that high order singularities are difficult to resolve. However, in the accompanying numerical study, part 2, the boundary layer at the equatorial plane of a spinning sphere is solved using up to 1000 mesh points across the boundary layer. Even at such high resolution, no trace of singular behavior was observed, and derivatives of high order could be evaluated precisely.

When the fact that solutions to the momentum equations are regular is accepted, (and for compressible flow in addition the density must be regular), the next question to arise is what implications such regularity has for the structure of the separation process. First, only the continuity equation can develop singular behavior, and from (2.2) or (2.6) it follows that this is only possible if the Lagrangian gradients of x and z become parallel, i.e. if at some point s

$$\nabla x = \lambda_s \nabla z \quad , \quad (2.7a)$$

where λ_s is a constant. Generally, the point s of interest is the particle and time at which

(2.7a) is satisfied for the first time. The condition (2.7a) is a three-dimensional extension of the two-dimensional condition first pointed out by Van Dommelen & Shen (1980a); it requires that a Lagrangian stationary point, $\nabla n = 0$, exists for an oblique coordinate

$$n = x - \lambda_s z \quad . \quad (2.7b)$$

An alternate way to phrase the condition for singular y is to define a unit vector in n -direction tangential to the wall,

$$\mathbf{n} = (n_x, n_z) = \frac{(1, -\lambda_s)}{\sqrt{1 + \lambda_s^2}} \quad , \quad (2.7c)$$

in which case a singularity occurs when, for all infinitesimal changes $\partial\xi$ in fluid particle,

$$\mathbf{n} \cdot \partial\mathbf{x} = 0 \quad , \quad \partial\mathbf{x} = (\partial x, \partial z) \quad . \quad (2.7d, e)$$

This implies that an infinitesimal particle volume $\partial\xi\partial\eta\partial\zeta$ around point s has been compressed to zero physical size in the n -direction. But since particle volume (or mass in compressible flow) is conserved, this compression in the n -direction along the wall is compensated for by a rapid expansion in the y -direction (see figure 1), which drives the fluid above the compressed region $\partial\xi\partial\eta\partial\zeta$ 'far' from the wall to form a separating vorticity layer.

From (2.6) it can be shown that this process constitutes separation in the sense of Sears & Telionis (1975), since the particle distance from the wall becomes too large, 'infinite', to be described on the usual boundary-layer scale. Note that the assumed regularity of x and z does not allow an infinite expansion in the direction parallel to the wall but normal to \mathbf{n} ; the particle can only expand strongly in the direction away from the wall. Similarly for a compressible fluid, the assumed regularity of ρ is inconsistent with an infinite compression of the particle volume. (At present there is no direct numerical evidence for the regularity assumption in the compressible case, although it is of course self-consistent).

From (2.7) we can derive generalized so-called Moore-Rott-Sears (MRS) conditions at the stationary point, similar to the conditions formulated by Sears & Telionis (1975) for two-dimensional flow. The form of the Eulerian D_y operator (2.4) implies using (2.2b) and (2.7a) that the vorticity vanishes at that point, i.e.

$$D_y u = D_y w = 0 \quad \text{at} \quad \nabla n = 0 \quad . \quad (2.8a)$$

In fact, the D_y -operator vanishes for all quantities which remain regular in the Lagrangian domain.

The second Moore-Rott-Sears condition is more complicated. Since (2.7a) is equivalent to two conditions on the Lagrangian derivatives of x and z , in three dimensional space we expect it to be satisfied on a curve of particles for times beyond the first occurrence of separation (c.f. section 3 and sub-section 4c). The Eulerian projection of the singular curve on the wall will be denoted by $x_{MRS} = (x_{MRS}, z_{MRS})$ and the Moore-Rott-Sears condition concerns the motion of this projected curve. To derive it, we focus attention on an arbitrary point s on the singular curve (rather than our usual choice in which s is the first point at which a singularity occurs). First we consider a Lagrangian differential $\partial\xi$ along the singular curve passing through point s , keeping time constant. Since x and z are functions of ξ and t only, $\partial\xi$ corresponds to a change in Eulerian position along the projected curve which satisfies (2.7d),

$$\mathbf{n} \cdot \partial \mathbf{x}_{MRS} = 0 \quad , \quad (2.8b)$$

so that the singular curve is normal to the local vector \mathbf{n} . As for any curve, the propagation velocity of this curve is given by the component of the propagation velocity of points on the curve in the direction normal to the curve. To find an expression for it, we now consider a total differential in Lagrangian space-time at the point s , resulting in changes $d\mathbf{x}_{MRS} = \partial\mathbf{x}_{MRS} + \dot{\mathbf{x}}_s dt$ and $dz_{MRS} = \partial z_{MRS} + \dot{z}_s dt$. Since $(\partial\mathbf{x}_{MRS}, \partial z_{MRS})$ satisfies (2.8b),

$$\mathbf{n} \cdot \frac{d\mathbf{x}_{MRS}}{dt} = \mathbf{n} \cdot \mathbf{u}_{MRS} \quad , \quad \mathbf{u}_{MRS} = (\dot{x}_s, \dot{z}_s) \quad , \quad (2.8c, d)$$

which shows that the propagation velocity of the singular curve equals the flow velocity of the singular particle s at the considered position (x_{MRS}, z_{MRS}) .

While this three-dimensional form of the MRS condition seems new, the general applicability of the two-dimensional case is fairly well established both theoretically (Moore 1958, Sears & Telionis 1975, Williams 1977, Shen 1978, Sychev 1979, 1980, Van Dommelen & Shen 1980b, 1982, 1983a,b, Van Dommelen 1981) and experimentally (Ludwig 1964, Didden & Ho 1985).

We can also verify the notion of Sears & Telionis (1975) that unsteady separation occurs in the middle of the boundary layer rather than at the wall. In the absence of a

transpiration velocity, the motion of points on the wall equals the motion of the boundary-layer particles at the wall, cf. (2.5) and (2.3a, b). Thus a fluid particle at the wall can only contract to vanishing size in the n -direction if the wall itself performs the same contraction, which is not possible for a solid wall.

In the next sections the nature of the separation process is analyzed. First we form local Taylor series expansions for the regular solutions to the momentum equations near the stationary point, and then we expand the solutions of the continuity equation in an asymptotic series. This procedure is similar to the one followed by Van Dommelen & Shen (1982) for two-dimensional separation. In contrast to the steady viscous singularities of Goldstein (1948) and Brown (1965), and the ideas of Sears & Telionis (1975), the unsteady singularity is essentially inviscid in character and consists of two vortex sheets separated by an increasingly large central inviscid region (as found by Ockendon (1972) for a rotating disc with suction, and by Sychev (1979, 1980), Van Dommelen & Shen (1980b, 1983a, b), Williams & Stewartson (1983) and Elliott, Cowley & Smith (1983) for steady separation over up- and down-stream moving walls). The leading order asymptotic structure of the unsteady singularity has also been recovered by Van Dommelen (1981) as a matched asymptotic solution to the Eulerian boundary-layer equations. More generally, Elliott *et al.* (1983) showed that there is a certain amount of arbitrariness in the Eulerian expansions. The Lagrangian expansion resolves such arbitrariness by the assumption, (supported by various numerical data, see Van Dommelen & Shen (1982), the closing remarks of subsection 4c, and part 2), that the leading order coefficients in the Taylor series expansion near the stationary point are non-zero.

3. Three-dimensional separation singularities

In this section we find the leading order term of an asymptotic analysis which describes the local structure of the flow as unsteady separation is approached. The time and position at which the separation singularity first develops will be denoted by the subscript s , thus for example

$$(\nabla n)_s = 0 \quad , \quad (3.1a)$$

where n is the oblique coordinate corresponding to the initial separation, defined in (2.7b) as

$$n = x - \lambda_s z \quad . \quad (3.1b)$$

Note that the definition of the x - and z -coordinates can simply be interchanged if n and z are not independent coordinates. In index notation, (3.1a) can be written as $n_i = 0$, where we will adopt the convention to omit the subscripts comma (to indicate Lagrangian derivatives) and s (to indicate the separation particle at the separation time) if they occur together (i.e. $n_i = (n_i)_s$).

The solution of the continuity equation (2.2) for y can be greatly simplified by a number of coordinate transformations for both the particle position coordinates (x, z) and the Lagrangian coordinates (ξ, η, ζ) . Here we will select transformations which preserve the Jacobian J (2.2b), since these are algebraically more simple than transformations which preserve the physical volume HJ , or mass ρHJ .

As a first transformation, we drop the position coordinate x in favor of n , shift the Lagrangian coordinate system to the separation particle s , and rotate it, resulting in the set of coordinates

$$n = x - \lambda_s z \quad , \quad z \quad , \quad k_i = \sum_{j=1}^3 a_{ij} (\xi_j - \xi_{js}) \quad , \quad (3.2a, b, c)$$

where a_{ij} is an orthonormal rotation matrix which is chosen to eliminate the mixed derivatives n_{12} , n_{13} , and n_{23} . Therefore, expanding n and z in a Taylor series expansion about the separation point, we obtain

$$n = n_s + \sum_{i=1}^3 \frac{1}{2} n_{ii} k_i^2 + \dots + \delta t \left(\dot{n}_s + \sum_{i=1}^3 \dot{n}_i k_i + \dots \right) + \dots \quad , \quad (3.3a)$$

$$z = z_s + \sum_{i=1}^3 z_i k_i + \dots + \delta t \dot{z}_s + \dots \quad , \quad (3.3b)$$

where $\delta t = t - t_s$.

However, if t_s is the first time that a stationary point occurs, the Taylor series coefficients in (3.3) cannot be completely arbitrary: the singularity condition may not be satisfied anywhere for $\delta t < 0$. The condition for a singularity to exist for earlier times at some neighboring point is, in terms of n and z ,

$$n_{,i} - (\lambda - \lambda_s) z_{,i} = 0 \quad , \quad (3.4a)$$

where λ is the ratio between ∇z and ∇x at the neighboring singular point. Expanding (3.4a) in a Taylor series, we obtain

$$n_{ii}k_i - z_i\delta\lambda + \dot{n}_i\delta t + \dots = 0 \quad \text{for } i = 1, 2, 3 \quad , \quad (3.4b)$$

where $\delta\lambda = \lambda - \lambda_s$. If all three coefficients n_{11} , n_{22} , and n_{33} were non-zero, a solution to (3.4b) could be found for $\delta t < 0$, contradicting our assumption that the singularity develops first at $\delta t = 0$. (Strictly, because of the higher order terms omitted in (3.4b), the solution must be found iteratively, however, the iterations converge because the higher order terms act as a contraction mapping sufficiently close to point s). Therefore at the first occurrence of separation, at least one of n_{11} , n_{22} , or n_{33} must be zero, and we will reorder (k_1, k_2, k_3) such that n_{11} vanishes. In addition, the coefficients n_{22}, n_{33}, z_1 cannot all be non-zero, since by solving for $\delta\lambda$, k_2 , and k_3 , it again follows that a singularity exists for $\delta t < 0$. Without loss of generality, we assume that z_1 is zero, since if either n_{22} or n_{33} vanishes, the (k_1, k_2, k_3) coordinate system can be rotated further to eliminate z_1 .

It follows that in some suitably oriented Lagrangian coordinate system the conditions $n_{11} = z_1 = 0$ are necessary at the time when separation starts. This implies two additional conditions on $x(\xi, t)$ and $z(\xi, t)$, besides the two conditions implicit in (3.1a). Since Lagrangian space-time is four-dimensional, in general we do not expect that more than four conditions can be satisfied at any time. Hence, in the remainder of this section we will assume that the values of the remaining derivatives can be completely arbitrary and in general non-zero.

However, when the functions x and z are not arbitrary, but restricted by constraints of symmetry in the flow, the latter assumption needs to be reconsidered, since the symmetry requires that various derivatives must vanish. Examples are two-dimensional flow, and the flows discussed in the next section.

Under the assumption that the remaining coefficients in the Taylor series have arbitrary values, the transformation

$$\bar{z} = z - z(\xi_s, t) \quad , \quad \bar{n} = n - n(\xi_s, t) - \lambda_s^{(2)} \bar{z}^2 \quad , \quad (3.5a, b)$$

$$\bar{k}_1 = k_1 \quad , \quad \bar{k}_2 = \frac{n_{22} z_3 k_2 - n_{33} z_2 k_3}{\sqrt{n_{22}^2 z_3^2 + n_{33}^2 z_2^2}} \quad , \quad \bar{k}_3 = \frac{n_{33} z_2 k_2 + n_{22} z_3 k_3}{\sqrt{n_{22}^2 z_3^2 + n_{33}^2 z_2^2}} \quad , \quad (3.5c, d, e)$$

where

$$\lambda_s^{(2)} = \frac{n_{22}n_{33}}{2(n_{22}z_3^2 + n_{33}z_2^2)} \quad , \quad (3.5f)$$

eliminates the \bar{n}_{33} term. The final coordinate transform

$$l_1 = \bar{k}_1 + \frac{\bar{n}_{113}}{\bar{n}_{111}} \bar{k}_3 \quad , \quad l_2 = \bar{k}_2 \quad , \quad l_3 = \bar{k}_3 \quad , \quad (3.6a, b, c)$$

$$\bar{n} = \bar{n} - \lambda_s^{(3)} \bar{z}^3 - \mu_s \delta t \bar{z} \quad , \quad \bar{z} = \bar{z} \quad , \quad (3.6d, e)$$

where

$$\lambda_s^{(3)} = \frac{\bar{n}_{111}^2 \bar{n}_{333} - 3\bar{n}_{111} \bar{n}_{113} \bar{n}_{133} + 2\bar{n}_{113}^3}{6\bar{n}_{111}^2 \bar{z}_3^3} \quad , \quad \mu_s = \frac{\bar{n}_{111} \dot{\bar{n}}_3 - \bar{n}_{113} \dot{\bar{n}}_1}{\bar{n}_{111} \bar{z}_3} \quad , \quad (3.6f, g)$$

eliminates the \bar{n}_{113} , \bar{n}_{333} , and $\dot{\bar{n}}_3$ derivatives.

The transformed position coordinate \bar{n} corresponds to an oblique coordinate measured from a moving, curved line through the separation particle, viz.

$$\bar{n} = \bar{x} - \bar{x}_0(\bar{z}, t) \quad , \quad (3.7a)$$

where

$$\bar{x} = x - x(\xi_s, t) \quad , \quad \bar{z} = z - z(\xi_s, t) \quad , \quad (3.7b, c)$$

$$\bar{x}_0(\bar{z}, t) = \lambda_s \bar{z} + \lambda_s^{(2)} \bar{z}^2 + \lambda_s^{(3)} \bar{z}^3 + \mu_s \delta t \bar{z} \quad . \quad (3.7d)$$

Note that the curved line $\bar{x} = \bar{x}_0(\bar{z}, t)$, which can be viewed as the line along which the separation initially develops (see below), does not have a singular shape at the first occurrence of separation.

The Taylor series expansions for \bar{n} and \bar{z} near the separation point become

$$\bar{n} = \frac{1}{2} \bar{n}_{22} l_2^2 + \sum_{ijk} \frac{1}{6} \bar{n}_{ijk} l_i l_j l_k + \dots + \delta t \sum_i \dot{\bar{n}}_i l_i + \dots \quad , \quad (\bar{n}_{113} = \bar{n}_{333} = \dot{\bar{n}}_3 = 0) \quad , \quad (3.8a)$$

$$\bar{z} = \bar{z}_2 l_2 + \bar{z}_3 l_3 + \dots \quad . \quad (3.8b)$$

The characteristics of the Jacobian equation (2.2) for y are, in terms of the new coordinates,

$$\frac{dl_1}{dy} = \frac{\rho H}{\rho_0 H_0} \{ -\bar{z}_3 \bar{n}_{22} l_2 + \dots \} \quad , \quad (3.9a)$$

$$\frac{dl_2}{dy} = \frac{\rho H}{\rho_0 H_0} \{ \bar{z}_3 (\frac{1}{2} \bar{n}_{111} l_1^2 + \frac{1}{2} \bar{n}_{133} l_3^2 + \dot{\bar{n}}_1 \delta t) + \dots \} , \quad (3.9b)$$

$$\frac{dl_3}{dy} = \frac{\rho H}{\rho_0 H_0} \{ -\bar{z}_2 (\frac{1}{2} \bar{n}_{111} l_1^2 + \frac{1}{2} \bar{n}_{133} l_3^2 + \dot{\bar{n}}_1 \delta t) + \dots \} , \quad (3.9c)$$

with a singularity occurring when all three right hand side expressions vanish (note that not all three are independent). Near the point s , (3.9a) is zero on a surface approximating the $l_2 = 0$ plane, while both (3.9b) and (3.9c) vanish at points depending on the nature of the quadratic expression $(\frac{1}{2} \bar{n}_{111} l_1^2 + \frac{1}{2} \bar{n}_{133} l_3^2)$. If this quadratic is hyperbolic, singular particles occur along hyperbolic lines regardless of the sign of δt . Thus, if $\delta t = 0$ is to be the first time that separation occurs, the quadratic must be elliptic, and of the same sign as the constant term when $\delta t < 0$. This requires $\bar{n}_{111} \bar{n}_{133} > 0$ and $\bar{n}_{111} \dot{\bar{n}}_1 < 0$; we will choose the positive l_1 -direction such that

$$\bar{n}_{22} \bar{n}_{111} > 0 , \quad \bar{n}_{22} \bar{n}_{133} > 0 , \quad \bar{n}_{22} \dot{\bar{n}}_1 < 0 . \quad (3.10a, b, c)$$

The Lagrangian description of the separation process can now be completed by the determination of y at times shortly before the initial occurrence of separation. At $t = t_s$ the boundary-layer approximation is obviously no longer valid because from the integral (2.6) it follows that y becomes infinite at the stationary point. However, the rate of growth near this point can be found by means of an asymptotic expansion. To find local scalings, we follow the guiding principles of Van Dyke (1975). In general, we attempt to scale the Lagrangian coordinates l_i and the position coordinates \bar{n} , \bar{z} and y to variables L_i, N, Z , and Y such that in the inner region the Jacobian equation for Y , i.e.

$$J_L(N, Y, Z) = \begin{vmatrix} N_{L_1} & N_{L_2} & N_{L_3} \\ Y_{L_1} & Y_{L_2} & Y_{L_3} \\ Z_{L_1} & Z_{L_2} & Z_{L_3} \end{vmatrix} = \frac{\rho_0 H_0}{\rho H} , \quad (3.11)$$

has non-singular leading order coefficients. This suggests that the δt term in (3.9b), which ensures the absence of singular points for $\delta t < 0$, should be retained. Further, for $\delta t = 0$ we want to match the solution close to the stationary particle to a solution for y which is regular away from this point. Thus we want to retain those terms which ensure the absence of singular points away from particle ξ_s at time $\delta t = 0$, i.e. the l_1^2 - and l_3^2 -terms in (3.9b) and the l_3 -term in (3.9a). The appropriate scaling is therefore

$$l_1 = |\delta t|^{\frac{1}{2}} L_1 , \quad l_2 = |\delta t|^{\frac{3}{2}} L_2 , \quad l_3 = |\delta t|^{\frac{1}{2}} L_3 , \quad (3.12a, b, c)$$

$$\bar{n} = |\delta t|^{\frac{3}{2}} N \quad , \quad \bar{z} = |\delta t|^{\frac{1}{2}} Z \quad , \quad y = |\delta t|^{-\frac{1}{2}} Y \quad . \quad (3.12d, e, f)$$

These scalings suggest that the separation process occurs in a relatively thin strip, $\bar{n} \sim |\delta t|^{3/2}$ along a segment of the separation line $\bar{x} = \bar{x}_0(\bar{z}, t)$ of length $\bar{z} \sim |\delta t|^{1/2}$.

For the scaling (3.12), the solution for Y is most easily found by integration of (3.11) as in (3.9a), where L_2 and L_3 are eliminated in favor of N and Z , which are constant along the lines of integration, using (3.8). The result is:

$$Y \sim \frac{\rho_{0s} H_{0s}}{\rho_s H_s} \left(\int_{-\infty}^{L_0} \frac{dL}{\sqrt{P(L; N, Z)}} \pm \int_{L_1}^{L_0} \frac{dL}{\sqrt{P(L; N, Z)}} \right) \quad , \quad (3.13a)$$

where

$$P(L; N, Z) = -\frac{1}{3} \bar{n}_{22} \{ \bar{z}_3^2 \bar{n}_{111} L^3 + (3\bar{n}_{133} Z^2 - 6\bar{n}_1 \bar{z}_3^2) L - 6\bar{z}_3^2 N \} \quad , \quad (3.13b)$$

and $L_0(N, Z)$ is the real root of the cubic P . This root is a unique and continuous function of N and Z since P is a monotonically decreasing function of L from (3.10).

The choice of sign of the square-root in (3.13a), and the limits of integration are determined by the topology of the lines of constant N and Z . In physical space these lines are straight and pass vertically through the boundary layer; however, in Lagrangian space they are highly curved near the separation particle, as shown qualitatively in figure 2a. The lines can be divided into three segments corresponding to three asymptotic regions. The lower segments start at the wall and extend upward towards the vicinity of the separation particle. Because the Jacobian is nowhere singular along these segments, the y -positions of the fluid particles remain finite on the boundary-layer scale, i.e. the scaled coordinate Y is small. Hence, these lower segments give rise to a layer of particles at the wall with a thickness comparable to that of the original boundary layer, this is shown schematically in figure 1.

Along the central segments, the lines of constant N and Z pass through the vicinity of the separation particle. Here the y -position of the particles grows rapidly, and is given in scaled form by (3.13). Thus the central segments give rise to the intermediate, thicker, layer of particles shown in figure 1. The topology of the central segments in the Lagrangian domain, figure 2a, determines the choice of sign in (3.13a). From (3.8) and (3.9) it follows that on integrating upwards, L_1 increases from large negative values towards $L_0(N, Z)$.

Since Y is increasing along this part, the negative sign in (3.13a) applies. At position L_0 , the lines of constant N and Z turn around in the Lagrangian domain and L_1 again tends to $-\infty$; along this second part the positive sign in (3.13a) applies.

Along the third segments, the lines of constant N and Z proceed upwards toward the external flow. As in the lower segments, the Jacobian is no longer small here. Thus the changes in y are finite on boundary-layer scale, and the third segments give rise to a layer of particles with a boundary-layer scale thickness, atop the central region, as shown in figure 1.

Hence, the separation structure is one in which the boundary layer divides into a central layer of physical thickness proportional to $Re^{-\frac{1}{2}}|\delta t|^{-\frac{1}{2}}$ between two 'sandwich' layers of thickness proportional to $Re^{-\frac{1}{2}}$.

The structure (3.13) is identical to the one obtained by Van Dommelen & Shen (1982) for two-dimensional separation, except that the coefficients now depend on the position Z along the describing line \bar{x}_0 . A convenient way to illustrate the influence of the position Z is to scale out the coefficients using a procedure similar to Van Dommelen (1981):

$$L_1 = \beta_2 \bar{L}_1 = \beta_2 (\bar{Z}^2 + 1)^{\frac{1}{2}} L_1^* \quad , \quad L_2 = \beta_0 \beta_2^{\frac{3}{2}} \bar{L}_2 = \beta_0 \beta_2^{\frac{3}{2}} (\bar{Z}^2 + 1)^{\frac{3}{2}} L_2^* \quad , \quad (3.14a, b)$$

$$N = \alpha \beta_2^3 \bar{N} = \alpha \beta_2^3 (\bar{Z}^2 + 1)^{\frac{3}{2}} N^* \quad , \quad Y = \frac{\bar{Y}}{\gamma \beta_2^{\frac{1}{2}}} = \frac{Y^*}{\gamma \beta_2^{\frac{1}{2}} (\bar{Z}^2 + 1)^{\frac{1}{2}}} \quad , \quad Z = \frac{\beta_2}{\beta_1} \bar{Z} \quad , \quad (3.14c, d, e)$$

where the tilde-variables scale out the Taylor series coefficients, the starred variables scale out Z , and

$$\alpha = \frac{1}{3} \bar{n}_{111} \quad , \quad \gamma = \left(\frac{1}{3} \bar{z}_3^2 \bar{n}_{22} \bar{n}_{111} \right)^{\frac{1}{2}} \frac{\rho_s H_s}{\rho_0 H_0} \quad , \quad (3.14d, e)$$

$$\beta_0 = \frac{\bar{z}_3 \bar{n}_{111}}{(\bar{z}_3^2 \bar{n}_{22} \bar{n}_{111})^{\frac{1}{2}}} \quad , \quad \beta_1 = \left(\frac{\bar{n}_{133}}{\bar{z}_3^2 \bar{n}_{111}} \right)^{\frac{1}{2}} \quad , \quad \beta_2 = \left(-\frac{2\bar{n}_1}{\bar{n}_{111}} \right)^{\frac{1}{2}} \quad . \quad (3.14f, g, h)$$

In terms of the starred variables (3.13) reduces to

$$Y^* \sim \int_{-\infty}^{L_0^*} \frac{dL^*}{\sqrt{2N^* - 3L^* - L^{*3}}} \pm \int_{L_1^*}^{L_2^*} \frac{dL^*}{\sqrt{2N^* - 3L^* - L^{*3}}} \quad , \quad (3.14i)$$

where

$$L_0^*(N^*) = I(N^*) \quad , \quad (3.15a)$$

and the function I is the inverse to the cubic $N^* = \frac{1}{2}I^3 + \frac{3}{2}I$, i.e.

$$I(N^*) = \left(N^* + (1 + N^{*2})^{\frac{1}{2}} \right)^{\frac{1}{3}} + \left(N^* - (1 + N^{*2})^{\frac{1}{2}} \right)^{\frac{1}{3}} . \quad (3.15b)$$

The values of β_1/β_2 , $\alpha\beta_2^3$, and $\gamma\beta_2^{\frac{3}{2}}$ depend on the choice of the Eulerian coordinates (x, z) , but not on the definition of the Lagrangian coordinates.

An alternative expression for Y^* can be found in terms of the incomplete elliptic integral of the first kind $F(\phi|m)$:

$$Y^*(L_1^*, N^*) \sim \frac{2}{\Lambda} F\left(\frac{\pi}{2}|m\right) \pm \frac{1}{\Lambda} F(\varphi|m) , \quad (3.16a)$$

where

$$\Lambda(N^*) = \left(3(L_0^{*2} + 1) \right)^{\frac{1}{4}} , \quad m(N^*) = \frac{1}{2} + \frac{3L_0^*}{4\Lambda^2} , \quad (3.16b, c)$$

$$\varphi(L_1^*, N^*) = 2 \arctan \left(\frac{\sqrt{L_0^* - L_1^*}}{\Lambda} \right) . \quad (3.16d)$$

Elliptic integrals are distorted identity functions, (in particular $F(\varphi|0) = \varphi$ exactly), so that the arctan is responsible for the major variations in Y along the characteristics.

Further terms in the asymptotic expansions (3.8) and (3.16) can be found in principle. We note that the next term in the expression for Y does not involve a logarithmic correction, even though logarithmic second order terms do arise for the symmetric flows studied in the next section.

We now turn to the physical interpretation of these results. The boundary-layer thickness is asymptotically determined by the position of the upper particle layer in figure 1; letting $L_1^* \rightarrow -\infty$ along the positive branch of (3.16a), we obtain the scaled boundary-layer thickness as

$$Y^{+*}(N^*) \sim \frac{4}{\Lambda} F\left(\frac{\pi}{2}|m\right) . \quad (3.17)$$

The function $Y^{+*}(N^*)$ gives the general shape of the boundary-layer thickness in a cross-section of constant z . For large values of N^* the boundary-layer thickness decays toward zero much more slowly than suggested by the sketch in figure 1. Nevertheless, at the outer edges of the thin separation region, the solution still matches with finite values of y ; for from (3.12), (3.14), and (3.16)

$$y^+ \sim \frac{4\alpha^{\frac{1}{2}}}{3^{\frac{1}{2}}2^{\frac{1}{2}}\gamma} F\left(\frac{\pi}{2} \left| \frac{1}{2} \pm \frac{\sqrt{3}}{4} \right. \right) \frac{1}{|\bar{n}|^{\frac{1}{2}}} \quad \text{for } |\delta t|^{\frac{3}{2}} \ll |\bar{n}| \ll 1 . \quad (3.18)$$

To show the dependence of the boundary-layer thickness on the coordinate z , contours of constant \bar{Y}^+ in the \bar{N}, \bar{Z} -plane are plotted in figure 2b. Note that the coordinate \bar{N} is measured from the oblique, curved, separation line. Actual lines of constant boundary-layer thickness might, for example, appear as sketched in figure 2c, which has been drawn by taking $|\delta t| = 0.06$ and unit values for various coefficients in (3.7) and (3.14). Asymptotically, the boundary-layer thickness has the shape of a crescent shaped ridge. The crescent shape is long and thin, i.e. quasi-two-dimensional, because from (3.12) the \bar{n} length scale is asymptotically shorter than the \bar{z} length scale (note that for three-dimensional *steady* separation Smith (1978) has proposed a quasi-two-dimensional structure). In an Eulerian numerical calculation, the development of such a crescent-shaped ridge may be a possible diagnostic indicating the presence of a singularity.

Evidence of this type of singularity is provided by Ragab's (1986) calculations for impulsively started flow past a 4:1 prolate spheroid inclined at a 30° angle of attack. His results strongly suggest that the displacement thickness becomes unbounded away from the symmetry line. However, it is not possible to deduce the shape of the singularity from the results presented.

A point of interest is the decay of the boundary-layer thickness along the describing line for large \bar{Z} . From (3.12), (3.14), and (3.16),

$$y^+ \sim \frac{1}{\gamma\beta_1^{\frac{1}{2}}} Y^{+*} \left(\frac{\bar{n}}{\alpha\beta_1^3 |\bar{z}|^3} \right) \frac{1}{|\bar{z}|^{\frac{1}{2}}} \quad \text{for } |\delta t|^{\frac{1}{2}} \ll |\bar{z}| \ll 1 \quad . \quad (3.19)$$

Hence for increasing \bar{z} , the separation structure expands in \bar{n} -direction, while the thickness of the boundary-layer decreases.

The particle propagation velocity $\dot{\bar{n}}$ which gives rise to the accumulation of particles at the separation line is, according to (3.8a), given to leading order by

$$\dot{\bar{n}} \sim |\delta t|^{\frac{1}{2}} \dot{\bar{n}}_1 L_1 \quad . \quad (3.20)$$

To describe this in the more familiar Eulerian coordinates, the transcendental relationship (3.16) must be inverted to the form

$$L_1^* = L_1^*(N^*, Y^*) \quad . \quad (3.21)$$

The inversion has been performed numerically, and in figure 2d we present contours of L_1^* in the (N^*, Y^*) plane. From (3.14),

$$\dot{\bar{n}} \sim -|\delta t|^{\frac{1}{2}} \frac{3}{2} \alpha \beta_2^3 (\bar{Z}^2 + 1)^{\frac{1}{2}} L_1^* \left(\frac{\bar{N}}{(\bar{Z}^2 + 1)^{\frac{3}{2}}}, \bar{Y} (\bar{Z}^2 + 1)^{\frac{1}{2}} \right). \quad (3.22)$$

It follows that the lines of constant L_1^* shown in figure 2d describe the shape of the lines of constant $\dot{\bar{n}}$ in cross-sections of constant \bar{z} through the separation structure. They also give the asymptotic shape of the lines of constant velocity components \dot{x} and \dot{z} and density ρ in these cross-sections, since

$$(\dot{x}, \dot{z}, \rho) = (\dot{x}_s, \dot{z}_s, \rho_s) + |\delta t|^{\frac{1}{2}} \left((\dot{\bar{x}}_1, \dot{\bar{z}}_1, \bar{\rho}_1) \beta_2 (\bar{Z}^2 + 1)^{\frac{1}{2}} L_1^* + (\dot{\bar{x}}_3, \dot{\bar{z}}_3, \bar{\rho}_3) \frac{\beta_2}{\beta_1 \bar{z}_3} \bar{Z} \right) + \dots \quad (3.23)$$

We note that the topology of figure 2d for $|\delta t| \approx 0$ seems quite close to the computed lines of constant velocity presented by Van Dommelen (1981) for finite $|\delta t|$, and thus lines of constant velocity might be a useful indication of an incipient unsteady separation.

The next point of interest is the shape of the velocity profiles. According to (3.23), in Eulerian space the velocity profiles must develop a large flat region of nearly constant velocity as separation is approached. However, accepting the numerical results of Van Dommelen (1981), this flat region is only evident extremely close to the singularity, so that resolution problems or finite Reynolds number effects tend to obscure the phenomenon. From (3.23) and figure 2d, the velocity profiles near an incipient three-dimensional separation must have a local maximum or minimum in velocity. However, this is not necessarily a precise indication of incipient separation. For example, in the case of the circular cylinder, a minimum in the velocity profiles develops relatively quickly, after $\frac{1}{6}$ diameter motion, yet separation occurs much later, after $\frac{3}{4}$ diameter motion. Figure 2e shows the shape of the velocity profiles near the interior extrema. The shapes of the velocity profiles in the sandwich layers at the edges of figure 2e cannot be found from asymptotic analysis since they depend on the precise details of the earlier evolution (cf. the remarks below (3.24) and part 2).

A more significant sign of the start of separation might be a transverse expansion of the lines of constant vorticity near the velocity minimum/maximum; since the above analysis is inviscid to leading order, the vorticity lines closely follow the motion of the

boundary-layer particles. In the boundary-layer approximation, the vorticity is the y -derivative of the velocity distribution. The corresponding asymptotic topology of contours of $\partial L_1^*/\partial Y^*$ is shown in figure 2f. This topology seems close to the computed vorticity lines presented by Van Dommelen (1981) for a time near separation.

The asymptotic structures of the upper and lower vorticity layers are similar to the two-dimensional case (Van Dommelen 1981). Expressed in terms of Eulerian coordinates, they take the form of regular Taylor expansions:

$$\left(\dot{x}, \dot{y}, \dot{z}, \dot{\rho}\right) = \sum_{mnr \geq 0} \bar{x}^m \bar{z}^n \delta t^r \left(u_{mnr}^-(\bar{y}), v_{mnr}^-(\bar{y}), w_{mnr}^-(\bar{y}), \rho_{mnr}^-(\bar{y})\right) \quad , \quad (3.24a)$$

and

$$\left(\dot{x}, \dot{y}, \dot{z}, \dot{\rho}\right) = \sum_{mnr \geq 0} \bar{x}^m \bar{z}^n \delta t^r \left(u_{mnr}^+(\bar{y}), v_{mnr}^+(\bar{y}), w_{mnr}^+(\bar{y}), \rho_{mnr}^+(\bar{y})\right) \quad , \quad (3.24b)$$

respectively, where the sums run over the non-negative integers, and the Prandtl transformation $\bar{y} = y - y^+(\bar{x}, \bar{z}, \delta t)$, describes the motion of the upper layer.

Substituting (3.24) into the boundary-layer equations, we find that the $u_{mnr}^\pm, w_{mnr}^\pm, \rho_{mnr}^\pm$, ($m, n \geq 0, r \geq 1$) and the v_{mnr}^\pm , ($m, n, r \geq 0$) are determined in terms of the $(u_{mn0}^\pm, w_{mn0}^\pm, \rho_{mn0}^\pm)$, but that these latter functions are indeterminate due to the dependence of the solution on earlier times. The $(u_{mn0}^\pm, w_{mn0}^\pm, \rho_{mn0}^\pm)$ must, however, satisfy the boundary conditions (2.5a) at the wall, and match both at the outer edge of the boundary layer (see (2.5b)), and with the central inviscid low-vorticity region. At fixed N and Z , the latter matching conditions yield from inverting (3.16) and using (3.23),

$$(u_{000}^-, w_{000}^-, \rho_{000}^-) \rightarrow (\dot{x}_s, \dot{z}_s, \rho_s) - (\dot{\bar{x}}_1, \dot{\bar{z}}_1, \bar{\rho}_1) \frac{4}{\gamma^2} \frac{1}{y^2} \quad \text{as } y \rightarrow +\infty \quad , \quad (3.25a)$$

$$(u_{000}^+, w_{000}^+, \rho_{000}^+) \rightarrow (\dot{x}_s, \dot{z}_s, \rho_s) - (\dot{\bar{x}}_1, \dot{\bar{z}}_1, \bar{\rho}_1) \frac{4}{\gamma^2} \frac{1}{\bar{y}^2} \quad \text{as } \bar{y} \rightarrow -\infty \quad . \quad (3.25b)$$

Asymptotic matching conditions can also be derived as $|N|, |Z| \rightarrow \infty$, as Van Dommelen (1981) has done for two-dimensional flows.

A final point of interest is the 'accessibility' of the region of flow beyond the time of initial separation. In a steady Eulerian computation, Cebeci, Khattab & Stewartson (1981) took the accessible region to be the domain where a boundary-layer solution can be

found, (whether it is still an asymptotically correct solution of the Navier-Stokes equations in the presence of interaction or not). In the Lagrangian case, some care is needed, because the singular continuity equation is integrated separately. Numerical experiments such as the one in part 2 do in fact suggest that the non-singular momentum equations can be integrated past the separation singularity without apparent difficulty. When that is done, the vertical lines through the boundary layer appear in Lagrangian space as shown in figure 2g rather than figure 2a. For the shaded particles, y is indeterminate; these particles may be thought of as having disappeared at infinite y . Yet the continuity equation can still be integrated along all lines of constant \bar{n} and \bar{z} which start at the wall. A singularity develops only on the line passing through the saddle point in figure 2g, which for $0 < \delta t \ll 1$ corresponds to a singular line segment

$$\bar{N} \sim + (1 - \bar{Z}^2)^{\frac{3}{2}} . \quad (3.26)$$

However, the solution so obtained must be considered meaningless at least for all particles which have at some *previous* time passed through the singular curve. For that reason, we define the region of inaccessibility as those stations (x, z) which contain particles which have at any time been on the singular curve. Initially, the region of inaccessibility will primarily expand in the z -direction through the scaling (3.12e). In the n -direction it will expand by means of the motion of the describing line (3.7) and additionally through the motion of the particles which propagate downstream away from the singular curve. Thus, the region of inaccessibility extends over a finite surface area, rather than just the curve (3.26), in agreement with the steady Eulerian definition of Cebeci *et al.* (1981).

Naturally, the singularity structure derived here will not remain asymptotically correct arbitrarily close to $t = t_s$, because the normal velocity above the central inviscid region becomes infinite at $t = t_s$. From a study of the Navier-Stokes equations it is found that the singularity is smoothed out when a 'triple-deck' interaction comes into operation for $\delta t = O(Re^{-\frac{2}{11}})$, at which point the scaled boundary-layer thickness is $O(Re^{\frac{1}{11}})$. Because the singularity is quasi-two-dimensional, the scalings and governing equations are essentially those derived by Elliott *et al.* (1983) for two-dimensional flows, but with the addition of a passive z -momentum equation. In the central interaction problem, the coordinate z , which has an interaction length scale $O(Re^{-\frac{1}{11}})$, only appears as a parameter. However, it is not clear whether the singularity will be completely removed by the interaction (Smith 1987).

4. Three-dimensional symmetric separation

In the previous section a separation singularity structure was derived assuming that the flow was arbitrary, an assumption that might be appropriate for flow past an asymmetric body. However, in the case of a spheroid at relatively small angles of attack it is likely that separation first occurs on one of the symmetry lines; indeed numerical calculations confined to the symmetry line have been performed on this basis (Wang & Fan (1982) Cebeci, Stewartson & Schimke (1984)). In sub-section (a) below we derive the form of the singularity appropriate for separating flows where the separation line crosses a symmetry line normally.

However, this is not the only type of symmetric separation of interest. When a sphere is impulsively rotated about a diameter, centripetal effects generate a boundary-layer flow towards the equator. After a finite time an equatorial singularity develops as a result of a boundary-layer collision. The structure of this singularity on the symmetry line has been determined by Banks & Zaturka (1979), and Simpson & Stewartson (1982a). In this case the separation line coincides with the symmetry line. Similar singularities occur after a finite time at the apex of a horizontal circular cylinder which is impulsively heated (Simpson & Stewartson 1982b), at the inner bend of a uniformly curved pipe through which flow is impulsively started (Lam 1988), and at the stagnation points on a two-dimensional cylinder in oscillating flow as a result of steady streaming effects (Vasantha & Riley 1988).

A more general form of the singularity generated by two symmetric colliding boundary layers on a smooth wall would first develop at a point rather than along the entire symmetry line. For example, such a singularity might develop on the equator of an ellipsoid which is rotated about one of its principal axes, or in starting flow through a curved pipe with non-uniform curvature, or at the apex of a heated ellipsoid. In sub-section (b) the three-dimensional structure of such a singularity is derived. The results on the symmetry line agree with previous authors, but the simplicity of the Lagrangian approach allows us to determine additionally the singularity structure off this line. The latter is a necessary preliminary in order to formulate subsequent asymptotic stages in the separation process.

Another class of separation singularities are rotationally symmetric about the separation point, so that the separation line degenerates to a point. For example, singularities develop after a finite time on the axis of a spinning disc or sphere whose direction of

rotation is impulsively reversed (Bodonyi & Stewartson 1977, Banks & Zaturka 1981, Stewartson, Simpson & Bodonyi 1982, Van Dommelen 1987), and at the apex of a sphere which is impulsively heated (Brown & Simpson 1982, Awang & Riley 1983). The structures of these singularities, which differ due to the presence and absence of swirl, are derived in sub-sections (c) and (d) respectively. The results *on* the axis agree with those of previous authors, while the singularity structures *off* the axis are new.

(a) Lateral symmetry

When the boundary-layer flow is symmetrical about a line along the surface of the body, the describing line of separation must either cross the symmetry line normally or coincide with it. In this sub-section we will address the case of normal crossing, leaving the second possibility to the next sub-section.

For consistency with section 3, we identify the compressed coordinate n with x and take the ξ, η -plane as the symmetry plane so that x is an even function of ζ and z an odd function. Then the analysis is a simpler version of the one in the previous section. The only transformation of the Lagrangian coordinate system needed is a rotation around the ζ -axis to eliminate the x_{12} derivative. Also, the discussion concerning which derivatives must be zero if t_s is the first separation time (see (3.4) and following) can be restricted to the symmetry plane to show that the second order derivative which is forced to be zero must lie within the symmetry plane.

Hence the structure of the separation process remains basically unchanged, although the describing line of separation simplifies, and is now symmetric about the symmetry line $z = 0$ (cf. (3.7)):

$$\bar{n} = x - x(\xi_s, t) - \frac{x_{33}}{2z_3^2} z^2 \quad (4.1)$$

A degenerate case is two-dimensional flow, where x is totally independent of ζ , and the separation line becomes a straight generator in the z -direction. In addition, the coefficient β_1 vanishes, which suppresses the decay of the boundary-layer thickness with z . The resulting structure is described in detail by Van Dommelen (1981).

Thus lateral symmetry, or more strongly two-dimensionality, does not fundamentally alter the separation process. This conclusion is consistent with the symmetry line calculations of Cebeci, Stewartson & Schimke (1984).

(b) Symmetric boundary-layer collision

When the describing line coincides with the symmetry line, significant changes in structure are unavoidable, since the flow is symmetric while the separation structure illustrated in figure 2 is asymmetrical.

We identify the compressed coordinate n again with x , but now we assume that the η, ζ -plane is the symmetry plane, so that x is an odd function of ξ while z is an even function. A singularity occurs when $x_{,\xi}$ first vanishes at the symmetry plane, since the derivatives $x_{,\eta}$ and $x_{,\zeta}$ are zero by symmetry. Since the first occurrence of a zero value must occur where $x_{,\xi}$ is a minimum, the second order derivatives $x_{\xi\eta}$ and $x_{\xi\zeta}$ must vanish, while the other second order derivatives are zero by symmetry.

The fact that all the second order derivatives are zero invalidates the scalings for η and y made in the previous section (e.g. (3.12), (3.14)), hence a separate analysis with significant modifications is needed. Proceeding along similar lines as in the previous section, a local Lagrangian coordinate system k_1, k_2, k_3 is introduced with origin at the separation particle, but with the same orientation as the original axis system. A rotation of this coordinate system around the k_1 -axis,

$$\bar{k}_1 = \xi \quad , \quad \bar{k}_2 = \frac{z_3 k_2 - z_2 k_3}{\sqrt{z_2^2 + z_3^2}} \quad , \quad \bar{k}_3 = \frac{z_2 k_2 + z_3 k_3}{\sqrt{z_2^2 + z_3^2}} \quad , \quad (4.2a, b, c)$$

$$\bar{x} = x \quad , \quad \bar{z} = z - z(\xi_s, t) \quad , \quad (4.2d, e)$$

can be made to eliminate the \bar{z}_2 -derivative. The shearing transformation

$$l_1 = \xi \quad , \quad l_2 = \bar{k}_2 + \frac{\bar{x}_{123}}{\bar{x}_{122}} \bar{k}_3 \quad , \quad l_3 = \bar{k}_3 \quad , \quad (4.3a, b, c)$$

$$\bar{x} = x \quad , \quad \bar{z} = z - z(\xi_s, t) \quad , \quad (4.3d, e)$$

eliminates the \bar{x}_{123} derivative, resulting in the Taylor series expansions

$$x \sim \frac{1}{6} \bar{x}_{111} l_1^3 + \frac{1}{2} \bar{x}_{122} l_1 l_2^2 + \frac{1}{2} \bar{x}_{133} l_1 l_3^2 + \dots + \delta t \bar{x}_1 l_1 + \dots \quad , \quad (4.4a)$$

$$\bar{z} \sim \bar{z}_3 l_3 + \dots \quad . \quad (4.4b)$$

The expressions for the characteristics of the Jacobian equation for y become

$$\frac{dl_1}{dy} = \frac{\rho H}{\rho_0 H_0} l_1 \{ -\bar{z}_3 \bar{x}_{122} l_2 + \dots \} \quad , \quad (4.5a)$$

$$\frac{dl_2}{dy} = \frac{\rho H}{\rho_0 H_0} \left\{ \bar{z}_3 \left(\frac{1}{2} \bar{x}_{111} l_1^2 + \frac{1}{2} \bar{x}_{122} l_2^2 + \frac{1}{2} \bar{x}_{133} l_3^2 + \delta t \dot{\bar{x}}_1 \right) + \dots \right\} \quad (4.5b)$$

In order to avoid singularities for $\delta t < 0$, the quadratic in (4.5b) must be elliptic and of opposite sign to $\dot{\bar{x}}_1$. Since $x_{,\epsilon}$ is initially positive, cf. (2.1), it follows from (4.4a) and (4.5b) that at a first zero

$$\bar{x}_{111} > 0, \quad \bar{x}_{122} > 0, \quad \bar{x}_{133} > 0, \quad \dot{\bar{x}}_1 < 0. \quad (4.6a, b, c, d)$$

The topology of the characteristics (4.5), shown in figure 3a, can be compared to the asymmetric case figure 2a, where the separation characteristic develops a cusp at $\delta t = 0$. In this case, the separation characteristic is constrained by symmetry to remain straight.

Appropriate local scalings near separation can be found using arguments similar to those of the previous section:

$$l_1 = |\delta t|^{\frac{1}{2}} \beta_2 \bar{L}_1 = |\delta t|^{\frac{1}{2}} \beta_2 (\bar{Z}^2 + 1)^{\frac{1}{2}} L_1^* \quad , \quad (4.7a)$$

$$l_2 = |\delta t|^{\frac{1}{2}} \beta_0 \beta_2 \bar{L}_2 = |\delta t|^{\frac{1}{2}} \beta_0 \beta_2 (\bar{Z}^2 + 1)^{\frac{1}{2}} L_2^* \quad , \quad (4.7b)$$

$$x = |\delta t|^{\frac{3}{2}} \alpha \beta_2^3 \bar{X} = |\delta t|^{\frac{3}{2}} \alpha \beta_2^3 (\bar{Z}^2 + 1)^{\frac{3}{2}} X^* \quad , \quad (4.7c)$$

$$y = \frac{\bar{Y}}{|\delta t|^{\frac{1}{2}} \gamma \beta_2} = \frac{Y^*}{|\delta t|^{\frac{1}{2}} \gamma \beta_2 (\bar{Z}^2 + 1)^{\frac{1}{2}}} \quad , \quad \bar{z} = |\delta t|^{\frac{1}{2}} \frac{\beta_2}{\beta_1} \bar{Z} \quad , \quad (4.7d, e)$$

$$\alpha = \frac{1}{3} \bar{x}_{111} \quad , \quad \gamma = \left(\frac{1}{3} \bar{z}_3^2 \bar{x}_{122} \bar{x}_{111} \right)^{\frac{1}{2}} \frac{\rho_s H_s}{\rho_{0s} H_{0s}} \quad , \quad (4.7f, g)$$

$$\beta_0 = \frac{\bar{z}_3 \bar{x}_{111}}{(\bar{z}_3^2 \bar{x}_{122} \bar{x}_{111})^{\frac{1}{2}}} \quad , \quad \beta_1 = \left(\frac{\bar{x}_{133}}{\bar{z}_3^2 \bar{x}_{111}} \right)^{\frac{1}{2}} \quad , \quad \beta_2 = \left(-\frac{2\dot{\bar{x}}_1}{\bar{x}_{111}} \right)^{\frac{1}{2}} \quad . \quad (4.7h, i, j)$$

The continuity integral becomes

$$Y^* = \int_0^{L_0^*} \frac{dL^*}{\sqrt{L^*(2X^* - 3L^* - L^{*3})}} \pm \int_{L_1^*}^{L_0^*} \frac{dL^*}{\sqrt{L^*(2X^* - 3L^* - L^{*3})}} \quad , \quad (4.8a)$$

where

$$L_0^*(X^*) = I(X^*) \quad . \quad (4.8b)$$

This can be written as an elliptic integral similar to (3.16),

$$Y^*(L_2^*, X^*) \sim \frac{2}{\Lambda} F\left(\frac{\pi}{2} | m \right) \pm \frac{1}{\Lambda} F(\varphi | m) \quad , \quad (4.9a)$$

where

$$\Lambda(X^*) = (3(L_0^{*2} + 1)(L_0^{*2} + 3))^{\frac{1}{4}}, \quad m(X^*) = \frac{1}{2} - \frac{3L_0^{*2} + 6}{4\Lambda^2}, \quad (4.9b, c)$$

$$\varphi(L_2^*, X^*) = 2 \arctan \left(\frac{1}{\Lambda} \sqrt{(L_0^{*2} + 3) \left(\frac{L_0^*}{L_1^*} - 1 \right)} \right). \quad (4.9d)$$

Note that instead of using L_1^* as the independent variable, there is an advantage in using L_2^* , as given implicitly by the relation

$$L_1^*(L_2^*, X^*) = (L_2^{*2} + 1)^{\frac{1}{2}} I(X^*/(L_2^{*2} + 1)^{\frac{1}{2}}), \quad (4.9e)$$

since at the symmetry line the solution is regular in terms of L_2^* :

$$Y^*(L_2^*, 0) \sim \frac{2}{\sqrt{3}} \left(\frac{\pi}{2} + \arctan L_2^* \right). \quad (4.10)$$

Contours of the boundary-layer thickness \bar{Y}^+ in the \bar{X}, \bar{Z} plane are shown in figure 3b. The asymptotic relations for large $|\bar{X}|$ and $|\bar{Z}|$, corresponding to (3.18) and (3.19), are

$$y^+ \sim \frac{4\alpha^{\frac{1}{2}}}{3^{\frac{1}{4}} 2^{\frac{1}{2}} \gamma} F \left(\frac{\pi}{2} \middle| \frac{1}{2} - \frac{\sqrt{3}}{4} \right) \frac{1}{|x|^{\frac{1}{2}}} \quad \text{for } |\delta t|^{\frac{1}{2}} \ll |x| \ll 1, \quad (4.11)$$

$$y^+ \sim \frac{1}{\gamma \beta_1} Y^{*+} \left(\frac{x}{\alpha \beta_1^3 |\bar{z}|^3} \right) \frac{1}{|\bar{z}|} \quad \text{for } |\delta t|^{\frac{1}{2}} \ll |\bar{z}| \ll 1. \quad (4.12)$$

The velocity components and density in the neighbourhood of the stationary point are given by

$$\dot{x} \sim -|\delta t|^{\frac{1}{2}} \frac{3}{2} \alpha \beta_2^3 (\bar{Z}^2 + 1)^{\frac{1}{2}} L_1^*, \quad (4.13a)$$

$$(\dot{z}, \rho) \sim (\dot{z}_s, \rho_s) + |\delta t|^{\frac{1}{2}} \left((\bar{z}_2, \bar{\rho}_2) \beta_0 \beta_2 (\bar{Z}^2 + 1)^{\frac{1}{2}} L_2^* + (\bar{z}_3, \bar{\rho}_3) \frac{\beta_2}{\beta_1 \bar{z}_3} \bar{Z} \right). \quad (4.13b)$$

Hence L_1^* can be interpreted as the velocity component towards the symmetry plane. The scaled velocity profile, $-L_1^*$, is illustrated in figure 3c at a number of X^* stations, while contours of L_1^* , and the corresponding vorticity component, dL_1^*/dY^* , are illustrated in figures 3d and 3e respectively. In cross-sections of constant z , the variations in velocity parallel to the symmetry plane are proportional to L_2^* . L_2^* velocity-profiles are given in figure 3f, while figures 3g and 3h illustrate contours of L_2^* and the vorticity dL_2^*/dY^* .

Close to the wall, i.e. as $Y \rightarrow 0$,

$$\dot{x} \sim -\frac{3}{4}\gamma^2\beta_2^2xy^2 \quad , \quad (\dot{z}, \rho) \sim (\dot{z}_s, \rho_s) - (\dot{\bar{z}}_2, \bar{\rho}_2) \frac{2}{\sqrt{3}} \frac{\beta_0}{\gamma} \frac{1}{y} \quad , \quad (4.14a, b)$$

which match to a regular vorticity layer of similar form to (3.24). Similarly a match can be achieved with a separating layer governed by a Prandtl transformation above the central inviscid region.

Figure 3i shows the characteristics, i.e. lines of constant x and z , for $\delta t > 0$. Integration of the continuity equation yields a singularity over a segment $-1 < \bar{Z} < 1$ of the symmetry line $\bar{X} = 0$. Since neither the singularity nor any particles on the symmetry line leave the symmetry line, the region of inaccessibility remains restricted to the symmetry line.

A special case occurs for separation at the intersection of two symmetry lines, such as at the apex of an ellipsoid. In that case, in addition to the symmetry in ξ , x is an even function of ζ and z an odd one, and the transformations of the Lagrangian coordinate system (4.2) and (4.3) become trivial. No changes in the leading order singularity structure occur, since it was already symmetric in z -direction, even though this condition was not imposed. However, the velocity parallel to the symmetry plane must be antisymmetric, and the density symmetric (cf. (4.13b):

$$\dot{z} \sim |\delta t|^{\frac{1}{2}} \dot{\bar{z}}_3 \frac{\beta_2}{\beta_1 \bar{z}_3} \bar{Z} \quad , \quad \rho \sim \rho_s + |\delta t|^{\frac{1}{2}} \bar{\rho}_2 \beta_0 \beta_2 (\bar{Z}^2 + 1)^{\frac{1}{2}} L_2^* \quad . \quad (4.15a, b)$$

In the case of two-dimensionality, where x is independent of ζ , the coefficient β_1 vanishes as in the previous subsection, suppressing the decay of the boundary-layer thickness with z . The flow on the symmetry line can then be written as a one-dimensional problem, and was studied from an Eulerian standpoint by Banks and Zaturka (1979) and Simpson & Stewartson (1982a,b). In part 2, Van Dommelen (1989) uses this flow to verify the Lagrangian analysis numerically to high accuracy. Favourable numerical comparisons with the singularity structure away from the symmetry line have been obtained by Lam (1988) for starting flow through a circular pipe.

The existence of this singularity has also been reported by Stern & Paldor (1983), Russell & Landahl (1984) and Stuart (1987) while studying *inviscid* models for the growth of large amplitude disturbances in boundary layers. In fact, because unsteady separation is

primarily inviscid in its final stages, an alternative approach to that above would be to solve the inviscid version of (2.3) exactly, and then to examine the possible singularities of the solutions (see also Van Dommelen (1981) for the two-dimensional singularity). Note that although Stuart's (1987) exact, inviscid, symmetry line solutions do not include a parallel flow in the z -direction, our results are in agreement since the details of the singularity structure are independent of $z(\xi_s, t)$.

As in section 3 the above singular solution will not remain valid for sufficiently small $|\delta t|$ because previously neglected pressure gradients will become important (cf. the interactive problem for the two-dimensional singularity formulated by Elliott *et al.* (1983)). Further, because the velocity towards the separation line is much smaller in the upper and lower vorticity layers than in the central layer, it is in the vorticity layers that the effect of the pressure gradient will be felt first. However, it is the central layer which is responsible for the growth in boundary-layer thickness; thus it appears that the first asymptotic rescaling does not lead to an 'interactive' effect to smooth out the above singularity. Instead, the singularity continues to be driven by the flow in the central layer, while significant changes occur in the upper and lower layers. Similar arguments seem to hold for the singularities in (c) and (d) below.

(c) Axisymmetric boundary-layer flow with swirl

In axisymmetric flow, the flow geometry does not depend on ξ and ζ individually, but only on the Lagrangian distance,

$$\varrho = \sqrt{\xi^2 + \zeta^2} \quad , \quad (4.16)$$

from the axis $\xi = \zeta = 0$. The displacement of rings of particles $\varrho = \eta = t = \text{constant}$ from their original position must remain restricted to a change in physical distance,

$$r = \sqrt{x^2 + z^2} \quad , \quad (4.17)$$

from the axis, a rotation around the axis, and a shift in vertical position. Hence according to the theory of orthogonal matrices, the solution must be of the form

$$x = c(\varrho^2, \eta, t)\xi + s(\varrho^2, \eta, t)\zeta \quad , \quad (4.18a)$$

$$z = -s(\varrho^2, \eta, t)\xi + c(\varrho^2, \eta, t)\zeta \quad , \quad (4.18b)$$

where, because of the assumption of regular x and z ,

$$c \sim x_{,\xi}(0, \eta, 0, t) + \frac{1}{6} x_{,\xi\xi\xi}(0, \eta, 0, t) \rho^2 + \dots \quad (4.19a)$$

$$s \sim x_{,\zeta}(0, \eta, 0, t) + \frac{1}{6} x_{,\zeta\zeta\zeta}(0, \eta, 0, t) \rho^2 + \dots \quad (4.19b)$$

In terms of c and s the physical distance from the axis is given by

$$r^2 = (c^2 + s^2) \rho^2 \quad (4.20)$$

The Jacobian J in (2.2) can be written in terms of ρ and r as

$$J = (r^2)_{,\rho^2} y_{,\eta} - (r^2)_{,\eta} y_{,\rho^2} \quad (4.21)$$

Thus separation occurs at a stationary point for $r^2(\rho^2, \eta, t)$, and from (4.20) and (4.21) it occurs on the axis when

$$c(0, \eta_s, t_s) = s(0, \eta_s, t_s) = 0 \quad (4.22a, b)$$

A rotation of the Lagrangian coordinate system to diagonalize the second order derivatives of x is not advantageous here, since the axial symmetry would be lost. Instead we rotate the coordinate system around the symmetry axis,

$$\bar{k}_1 = \frac{x_{23}\xi - x_{12}\zeta}{\sqrt{x_{12}^2 + x_{23}^2}} \quad , \quad \bar{k}_2 = \eta - \eta_s \quad , \quad \bar{k}_3 = \frac{x_{12}\xi + x_{23}\zeta}{\sqrt{x_{12}^2 + x_{23}^2}} \quad , \quad (4.23a, b, c)$$

to eliminate the \bar{x}_{12} -derivative, followed by the shearing transformation

$$l_1 = \bar{k}_1 \quad , \quad l_2 = \bar{k}_2 + \frac{\bar{x}_{333}}{6\bar{x}_{23}}(\bar{k}_1^2 + \bar{k}_3^2) + \delta t \frac{\dot{\bar{x}}_3}{\bar{x}_{23}} \quad , \quad l_3 = \bar{k}_3 \quad , \quad (4.24a, b, c)$$

to eliminate \bar{x}_{333} and $\dot{\bar{x}}_3$.

The characteristics of the Jacobian are lines of constant distance r from the axis. If t_s is the first time that a singularity forms then $\bar{x}_{111}\dot{\bar{x}}_1$ must be negative, or for a suitable choice of the positive l_1 -direction

$$\bar{x}_{111} > 0 \quad , \quad \dot{\bar{x}}_1 < 0 \quad . \quad (4.25a, b)$$

The characteristic lines of constant r in the ρ, l_2 -plane appear as sketched in figure 4a.

Appropriate local scalings are

$$e = |\delta t|^{\frac{1}{2}} \beta P^* , \quad l_2 = |\delta t| \beta_0 \beta^2 L_2^* , \quad r = |\delta t|^{\frac{1}{2}} \alpha \beta^3 R^* , \quad y = \frac{Y^*}{|\delta t| \gamma \beta^2} , \quad (4.26a, b, c, d)$$

$$\alpha = \frac{1}{3} \bar{x}_{111} , \quad \gamma = \frac{1}{3} \bar{x}_{111} (\bar{x}_{23}^2)^{\frac{1}{2}} \frac{\rho_s H_s}{\rho_{0s} H_{0s}} , \quad \beta_0 = \frac{\bar{x}_{111}}{2(\bar{x}_{23}^2)^{\frac{1}{2}}} , \quad \beta = \left(-\frac{2\bar{x}_1}{\bar{x}_{111}} \right)^{\frac{1}{2}} , \quad (4.26e, f, g, h)$$

leading to a continuity integral

$$Y^* \sim \int_0^{P_0^*} \frac{2dP^*}{\sqrt{4R^{*2} - (3P^* + P^{*3})^2}} \pm \int_{P^*}^{P_0^*} \frac{2dP^*}{\sqrt{4R^{*2} - (3P^* + P^{*3})^2}} , \quad (4.27a)$$

where

$$P_0^*(R^*) = I(R^*) . \quad (4.27b)$$

This can be written as the elliptic integral

$$Y^*(L_2^*, R^*) = \frac{2}{\Lambda} F\left(\frac{\pi}{2} | m \right) \pm \frac{1}{\Lambda} F(\varphi | m) , \quad (4.28a)$$

where

$$\Lambda(R^*) = (3(P_0^{*2} + 1)(P_0^{*2} + 3)^3)^{\frac{1}{4}} , \quad m(R^*) = \frac{1}{2} - \frac{3P_0^{*4} + 18P_0^{*2} + 18}{4\Lambda^2} , \quad (4.28b, c)$$

$$\varphi(L_2^*, R^*) = 2 \arctan \left(\frac{1}{\Lambda} \sqrt{(P_0^{*2} + 3)^2 \left(\frac{P_0^{*2}}{P^{*2}} - 1 \right)} \right) , \quad (4.28d)$$

and P^{*2} is related to L_2^* and R^* through the solution of the cubic equation

$$4R^{*2} = 9L_2^{*2} P^{*2} + (P^{*2} + 3)^2 P^{*2} . \quad (4.28e)$$

On the axis, (4.28a) simplifies to

$$Y^*(L_2^*, 0) = \frac{2}{3} \left(\frac{\pi}{2} + \arctan L_2^* \right) , \quad (4.29)$$

while for large R^* , the boundary-layer thickness asymptotes to

$$y^+ \sim \frac{4\alpha^{\frac{1}{2}}}{3^{\frac{1}{2}} 2^{\frac{1}{2}} \gamma} F\left(\frac{\pi}{2} \left| \frac{1}{2} - \frac{\sqrt{3}}{4} \right. \right) \frac{1}{r^{\frac{1}{2}}} \quad \text{for } |\delta t|^{\frac{1}{2}} \ll r \ll 1 . \quad (4.30)$$

The velocity components in the radial and azimuthal directions, and the density, are

$$\dot{r} \sim -|\delta t|^{\frac{1}{2}} \frac{3}{2} \alpha \beta^3 (U_0^* + \chi W_0^*), \quad r\dot{\theta} \sim |\delta t|^{\frac{1}{2}} \frac{3}{2} \alpha \beta^3 \zeta (W_0^* - \chi U_0^*), \quad \chi = \frac{\zeta \dot{x}_3}{\dot{x}_1}, \quad (4.31a, b, c)$$

$$\rho = \rho_s + |\delta t| (\bar{\rho}_2 \beta_0 \beta^2 L_2^* + \frac{1}{2} \bar{\rho}_{11} \beta^2 P^{*2} - \dot{\rho}), \quad (4.31d)$$

where $\zeta = \text{sgn}(\bar{x}_{23})$, and

$$U_0^* = \frac{(P^{*2} + 3)P^{*2}}{2R^*}, \quad W_0^* = \frac{3P^{*2}L_2^*}{2R^*}, \quad (4.32a, b)$$

are the symmetric and anti-symmetric velocity profiles shown in Figure 4b.

Both the radial and the circumferential velocity profiles depend non-trivially on the parameter χ . However the magnitude of the velocity,

$$q = \sqrt{u^2 + w^2} = |\delta t|^{\frac{1}{2}} \frac{3}{2} \alpha \beta^3 \sqrt{1 + \chi^2} P^*, \quad (4.33)$$

does not; contours of q are illustrated in figure 4c. The vorticity components normal to the velocity and parallel to it are proportional to

$$\Omega_n = \frac{U_0^* U_{0Y}^* + W_0^* W_{0Y}^*}{\sqrt{U_0^{*2} + W_0^{*2}}} = -\frac{3}{2} P^* L_2^*, \quad (4.34a, b)$$

$$\Omega_p = \frac{W_0^* U_{0Y}^* - U_0^* W_{0Y}^*}{\sqrt{U_0^{*2} + W_0^{*2}}} = -\frac{3}{2} P^* (P^{*2} + 1). \quad (4.35a, b)$$

Contours of these quantities are plotted in figures 4d and 4e respectively.

A match with the sandwich layer adjacent to the wall is again possible, since as $Y \rightarrow 0$

$$\dot{r} \sim \frac{3}{2} \gamma \beta^2 \chi r y, \quad r\dot{\theta} \sim -\frac{3}{2} \gamma \beta^2 \zeta r y, \quad \rho \sim \rho_s - \bar{\rho}_2 \frac{2}{3} \frac{\beta_0}{\gamma} \frac{1}{y}. \quad (4.36a, b, c)$$

Similarly a match can be achieved with the upper separating layer.

Figure 4f shows the characteristics for $\delta t > 0$. The singular line is the physically expanding circle $R^* = 1$, but the region of inaccessibility is larger due to particles with $L_2^* \neq 0$ which move radially outward from the singular line at a greater rate.

On the axis itself, the continuity integral is particularly simple:

$$y = \int_0^\eta \frac{\rho_0 H_0 d\eta}{\rho H(x_{,\xi}^2 + x_{,\zeta}^2)}. \quad (4.37)$$

When this integral is expanded to second order, a logarithmic correction to the y -position is obtained. This and other terms were initially overlooked in Eulerian analyses of the flow on the axis (Bodonyi & Stewartson (1977), Banks & Zaturka (1981)), but in a Lagrangian approach the logarithmic term follows naturally from the hypothesis that the solution for the motion parallel to the boundary is regular. (A similar logarithmic term arises in the symmetric case (b) above, cf. part 2). In fact, from this hypothesis alone, the complete singularity structure presented by Stewartson, Simpson & Bodonyi (1982) can be recovered by means of a simple integration of (4.37).

(d) Axisymmetric boundary-layer collision without swirl

Finally, we consider the case of axially symmetric flow when there is no rotation of the flow about the axis. In the absence of such rotation (4.18) simplifies to

$$x = c(\varrho^2, \eta, t)\xi \quad , \quad z = c(\varrho^2, \eta, t)\zeta \quad . \quad (4.38)$$

No transformations of the Lagrangian coordinate system are needed in this case. It follows that if a singularity first appears on the axis c must vanish. The contours of constant r are then identical to those for a symmetric collision (figure 3a), while the Taylor series coefficients satisfy conditions (4.6a,b,d).

In a similar way to before suitable local scalings are

$$\varrho = |\delta t|^{\frac{1}{2}} \beta P^* \quad , \quad l_2 = |\delta t|^{\frac{1}{2}} \beta_0 \beta L_2^* \quad , \quad r = |\delta t|^{\frac{1}{2}} \alpha \beta^3 R^* \quad , \quad y = \frac{Y^*}{|\delta t|^{\frac{1}{2}} \gamma \beta^3} \quad , \quad (4.39a, b, c, d)$$

$$\alpha = \frac{1}{3} \bar{x}_{111} \quad , \quad \gamma = \frac{1}{3} \left(\frac{1}{3} \bar{x}_{111}^3 \bar{x}_{122} \right)^{\frac{1}{2}} \frac{\rho_s H_s}{\rho_{0s} H_{0s}} \quad , \quad \beta_0 = \left(\frac{\bar{x}_{111}}{\bar{x}_{122}} \right)^{\frac{1}{2}} \quad , \quad \beta = \left(-\frac{2\dot{\bar{x}}_1}{\bar{x}_{111}} \right)^{\frac{1}{2}} \quad , \quad (4.39e, f, g, h)$$

leading to a continuity integral

$$Y^* \sim \int_0^{P_0^*} \frac{P^{*\frac{1}{2}} dP^*}{R^* \sqrt{2R^* - 3P^* - P^{*3}}} \pm \int_{P^*}^{P_0^*} \frac{P^{*\frac{1}{2}} dP^*}{R^* \sqrt{2R^* - 3P^* - P^{*3}}} \quad , \quad (4.40a)$$

where

$$P_0^*(R^*) = I(R^*) \quad . \quad (4.40b)$$

This solution can be 'reduced' to the form

$$Y^*(L_2^*, R^*) = \frac{1}{P_0^{*2} + 3} \left(\frac{4 - 4n}{\Lambda} \Pi(n; \frac{\pi}{2} | m) - \frac{2}{\Lambda} F(\frac{\pi}{2} | m) \right)$$

$$\begin{aligned} & \pm \frac{1}{P_0^{*2} + 3} \left(\frac{2 - 2n}{\Lambda} \Pi(n; \varphi | m) - \frac{1}{\Lambda} F(\varphi | m) \right. \\ & \quad + \frac{2}{P_0^*} \arctan \left(\frac{P_0^*}{2\Lambda} \frac{\sin(\varphi)}{\sqrt{1 - m \sin^2 \varphi}} \right) \\ & \quad \left. + \frac{2}{P_0^*} \arctan \left(\frac{n P_0^*}{2\Lambda} \frac{\sin(2\varphi)}{\sqrt{1 - m \sin^2 \varphi}} \right) \right), \quad (4.41a) \end{aligned}$$

where $\Pi(n; \varphi | m)$ is the incomplete elliptic integral of the third kind, and

$$\Lambda(R^*) = (3(P_0^{*2} + 1)(P_0^{*2} + 3))^{\frac{1}{4}}, \quad m(R^*) = \frac{1}{2} - \frac{3P_0^{*2} + 6}{4\Lambda^2}, \quad n(R^*) = 1 - \frac{3P_0^{*2} + 12}{2\Lambda^2 + 6}, \quad (4.41b, c, d)$$

$$\varphi(L_2^*, R^*) = 2 \arctan \left(\frac{1}{\Lambda} \sqrt{(P_0^{*2} + 3) \left(\frac{P_0^*}{P^*} - 1 \right)} \right), \quad (4.41e)$$

$$P^*(L_2^*, R^*) = (L_2^{*2} - 1)^{\frac{1}{2}} I(R^* / (L_2^{*2} + 1)^{\frac{3}{2}}). \quad (4.41f)$$

On the axis (4.41a) simplifies to

$$Y^*(L_2^*, 0) = \frac{2}{3\sqrt{3}} \left(\frac{\pi}{2} + \arctan L_2^* + \frac{L_2^*}{L_2^{*2} + 1} \right), \quad (4.42)$$

while for large R^* the boundary-layer thickness asymptotes to

$$y^+ \sim \frac{2\alpha}{3^{\frac{1}{2}} \gamma} \left(\sqrt{3} \Pi \left(1 - \frac{\sqrt{3}}{2}; \frac{\pi}{2} \middle| \frac{1}{2} - \frac{\sqrt{3}}{4} \right) - F \left(\frac{\pi}{2} \middle| \frac{1}{2} - \frac{\sqrt{3}}{4} \right) \right) \frac{1}{\tau}. \quad (4.43)$$

The velocity and density are given to leading order by

$$\dot{r} \sim -|\delta t|^{\frac{1}{2}} \frac{3}{2} \alpha \beta^3 P^*, \quad \rho \sim \rho_s + |\delta t|^{\frac{1}{2}} \bar{\rho}_2 \beta_0 \beta L_2^*. \quad (4.44a, b)$$

Sample velocity profiles are illustrated in figure 5a, while contours of P^* and the vorticity dP^*/dY^* are given in figures 5b and 5c respectively. Again, a match is possible with the wall layer, since as $Y \rightarrow 0$,

$$\dot{r} \sim -\frac{3^{\frac{5}{3}}}{2^{\frac{4}{3}}} \beta^2 \gamma^{\frac{2}{3}} r y^{\frac{2}{3}}, \quad \rho \sim \rho_s + \bar{\rho}_2 \frac{2^{\frac{2}{3}} \beta_0}{3^{\frac{5}{3}} \gamma^{\frac{1}{3}}} \frac{1}{y^{\frac{1}{3}}}. \quad (4.45a, b)$$

5. Discussion

In this paper we have shown that the description of attached flow past a body using the classical boundary-layer equations can break down after a finite time due the formation of a local singularity. In a Lagrangian description the class of singularities is characterized by a singular continuity equation, but a regular momentum equation. The evidence shows that such singularities are both mathematically consistent and physically relevant (e.g. Van Dommelen & Shen 1980a, Van Dommelen 1987, 1989, Lam 1988, Bouard & Coutanceau 1980). The precise structure of the singularity depends on the symmetry of the flow, and some of the simpler structures have previously been partially or totally described in Eulerian coordinates by other authors. The purpose of this paper is to provide a unified theory to facilitate the identification of singularities of the Lagrangian type when they do occur. This seems especially relevant for the difficult problem of the asymmetric singularity, where the singular behaviour would have to be deduced from a three-dimensional unsteady computation.

These singularities occur when a fluid particle becomes compressed in one direction parallel to the boundary. Conservation of mass then implies that the fluid above this fluid particle is forced out of the boundary layer in the form of a detached vorticity layer. A common feature of all the singularities is that the typical length scale in the direction of compression is $O(|\delta t|^{\frac{2}{3}})$. However, the the strength of the singularity increases with the symmetry of the flow; the the boundary layer thickness varies from $O(|\delta t|^{-\frac{1}{2}})$ for the asymmetric symmetry to $O(|\delta t|^{-\frac{2}{3}})$ for the axisymmetric singularity without swirl.

Because the singularities take the form of a vertical ejection of fluid from the boundary layer, we believe that they indicate the onset of separation as hypothesized by Sears & Telionis (1975). While the present singularity structures do at least seem to describe the initial genesis of the separating shear layer, within an asymptotically short time interactive effects which are neglected in the classical boundary-layer formulation must be included (e.g. Elliott *et al.*, 1983, Henkes & Veldman 1987). At that stage a new asymptotic scaling must be substituted into the Navier-Stokes equations in order to recover the correct large-Reynolds-number limit. Knowledge of the precise asymptotic structure of the singularities is necessary to identify this new scaling, and one of the contributions of this work has been to identify the full structure of a number of symmetric singularities.

At first sight the symmetric singularities may appear less likely to occur in problems of

practical importance. However, they have previously arisen in inviscid models of 'transition to turbulence' in regions where symmetric counter-rotating longitudinal vortices are forcing the convergence of fluid particles (Stern *et al.* (1983), Russell *et al.* (1984), Stuart (1987)). A three-dimensional extension of the work by Smith & Burggraf (1985), may lead to an asymptotic description of transition which accounts for viscosity, where the turbulent bursts are associated with local regions of classical boundary-layer separation (symmetric or otherwise).

This work was presented in part at the IUTAM "Fluid Mechanics in the Spirit of G.I. Taylor" Conference, April 1986, Cambridge. The authors acknowledge financial support from the NASA "Materials Processing in Space" program, the SERC, the AFOSR, and ICOMP, NASA Lewis.

References

- Awang, M.A.Omar & Riley, N. 1983 Unsteady free convection from a heated sphere at high Grashof number. *J. Engng. Math.* **17**, 355-365.
- Banks, W.H.H. & Zaturka, M.B. 1979 The collision of unsteady laminar boundary layers. *J. Engng. Math.* **13**, 193-212.
- Banks, W.H.H. & Zaturka, M.B. 1981 The unsteady boundary-layer development on a rotating disc in counter rotating flow. *Acta Mechanica* **38**, 143-155.
- Blasius, H. 1908 Grenzschichten in Flüssigkeiten mit kleiner Reibung. *Z. Math. Phys.* **56**, 1-37.
- Bodonyi, R.J. & Stewartson, K. 1977 The unsteady laminar boundary layer on a rotating disk in a counter-rotating fluid. *J. Fluid Mech.* **79**, 669-688.
- Bouard, R. & Coutanceau, M. 1980 The early stage of development of the wake behind an impulsively started cylinder for $40 < Re < 10000$. *J. Fluid Mech.* **101**, 583-607.
- Brown, S.N. 1965 Singularities associated with separating boundary layers. *Phil. Trans. R. Soc. Lond.* **A257**, 409-444.
- Brown, S.N. & Simpson, C.J. 1982 Collision phenomena in free-convective flow over a sphere. *J. Fluid Mech.* **124**, 123-127.
- Cebeci, T. 1982 Unsteady separation. In *Numerical and Physical Aspects of Aerodynamic*

Flows, ed. T. Cebeci. Springer-Verlag.

Cebeci, T. 1986 Unsteady boundary layers with an intelligent numerical scheme. *J. Fluid Mech.* **163**, 129-140.

Cebeci, T., Khattab, A.K. & Stewartson, K. 1981 Three-dimensional boundary layers and the ok of accessibility. *J. Fluid Mech.* **107**, 57-87.

Cebeci, T., Khattab, A.K. & Schimke, S.M. 1983 Can the singularity be removed in time-dependent flows? In *Proc. A.F. Workshop, Colorado Springs*.

Cebeci, T., Stewartson, K. & Schimke, S.M. 1984 Unsteady boundary layers close to the stagnation region of slender bodies. *J. Fluid Mech.* **147**, 315-332.

Cowley, S.J. 1983 Computer extension and analytic continuation of Blasius' expansion for impulsive flow past a circular cylinder. *J. Fluid Mech.* **135**, 389-405.

Didden, N. & Ho, C-M. 1985 Unsteady separation in a boundary layer produced by an impinging jet. *J. Fluid Mech.* **160**, 235-256.

Ece, M.C., Walker, J.D.A. & Doligalski, T.L. 1984 The boundary layer on an impulsively started rotating and translating cylinder. *Phys. Fluids* **27**, 1077-1089.

Elliott, J.W., Cowley, S.J. & Smith, F.T. 1983 Breakdown of boundary layers:, i. on moving surfaces, ii. in semi-similar unsteady flow, iii. in fully unsteady flow. *Geophys. Astrophys. Fluid Dynamics* **25**, 77-138.

Goldstein, S. 1948 On laminar boundary-layer flow near a position of separation. *Q. J. Mech. Appl. Math.* **1**, 43-69.

Henkes, R.A.W.M. & Veldman, A.E.P. 1987 On the breakdown of the steady and unsteady interacting boundary-layer description. *J. Fluid Mech.* **179**, 513-530.

Hudson, J.A. 1980 *The excitation and propagation of elastic waves*. Cambridge University Press.

Ingham, D.B. 1984 Unsteady separation. *J. Comp. Phys.* **53**, 90-99.

Lam, S.T. 1988 On high-Reynolds-number laminar flows through a curved pipe, and past a rotating cylinder. Ph.D. dissertation, Univ. of London.

Lamb, Sir Horace, 1945 *Hydrodynamics*. Dover.

Ludwig, G.R. 1964 An experimental investigation of laminar separation from a moving

wall. *AIAA paper* 64-6.

McCroskey, W. J. & Pucci, S. L. 1982 Viscous-inviscid interaction on oscillating airfoils in subsonic flow. *AIAA J.* **20**, 167-174.

Moore, F.K. 1958 On the separation of the unsteady laminar boundary layer. In *Boundary-Layer Research*, ed. H.G. Gortler. Springer.

Nagata, H., Minami, K. & Murata, Y. 1979 Initial flow past an impulsively started circular cylinder. *Bull. JSME* **22**, 512-520.

Ockendon, H. 1972 An asymptotic solution of steady flow above an infinite rotating disk with suction. *Q. J. Mech. Appl. Math.* **25**, 291-301.

Prandtl, L. 1904 Über Flüssigkeitsbewegung bei sehr kleiner Reibung. In *Ludwig Prandtl gesammelte Abhandlungen*, Springer-Verlag 1961, 575-584.

Ragab, S.A. 1986 The laminar boundary layer on a prolate spheroid started impulsively from rest at high incidence. *AIAA paper* 86-1109.

Rosenhead, L. 1963 *Laminar boundary layers*. Oxford University Press.

Rott, N. 1956 Unsteady viscous flows in the vicinity of a separation point. *Q. Appl. Math.* **13**, 444-451.

Russell & Landahl, 1984 The evolution of a flat eddy near a wall in an inviscid shear flow. *Phys. Fluids* **27**, 557-570.

Sears, W.R. 1956 Some recent developments in airfoil theory. *J. Aeronaut. Sci.* **23**, 490-499.

Sears, W.R. & Telionis, D.P. 1975 Boundary-layer separation in unsteady flow. *SIAM J. Appl. Math.* **23**, 215.

Shen, S.F. 1978 Unsteady separation according to the boundary-layer equation. *Adv. Appl. Mech.* **13**, 177.

Simpson, C.J. & Stewartson, K. 1982a A note on a boundary-layer collision on a rotating sphere. *Z. Angew. Math. Phys.* **33**, 370-378.

Simpson, C.J. & Stewartson, K. 1982b A singularity in an unsteady free-convection boundary layer. *Q. J. Mech. Appl. Math.* **35**, 291-304.

Smith, F.T. 1978. Three-dimensional viscous and inviscid separation of a vortex sheet

from a smooth non-slender body. *RAE Tech. Rep.* 78095.

Smith, F. T. 1987 Break-up in unsteady separation. In *Forum on Unsteady Flow Separation*, ASME FED-Vol. 52, 55-64.

Smith, F.T. & Burggraf, O.R. 1985 On the development of large-sized short-scaled disturbances in boundary layers. *Proc. R. Soc. Lond.* A399, 25-55.

Stern, M.E. & Paldor N. 1983 Large amplitude long waves in a shear flow. *Phys. Fluids* 26, 906-919.

Stewartson, K., Simpson, C.J. & Bodonyi, R.J. 1982 The unsteady boundary layer on a rotating disk in a counter rotating fluid II. *J.Fluid Mech.* 121, 507-515.

Stuart, J.T. 1987 Nonlinear Euler partial differential equations: singularities in their solution. Presented at the Symposium in Honor of Prof. C.C. Lin.

Sychev, V.V. 1979 Asymptotic theory of non-stationary separation. *Izv. Akad. Nauk. SSSR, Mekh. Zhid. i Gaza*, No. 6, 21-32. Also *Fluid Dynamics* 14, 829-838.

Sychev, Vik.V. 1980 On certain singularities in solutions of equations of boundary layer on a moving surface. *P.M.M.* 44, 830-838.

Telionis, D.P. & Tsahalis, D. Th. 1974 Unsteady laminar separation over impulsively moved cylinders. *Acta Astronautica* 1, 1487.

Van Dommelen, L.L. 1981 Unsteady boundary-layer separation. Ph.D. dissertation, Cornell University.

Van Dommelen, L.L. 1987 Computation of unsteady separation using Lagrangian procedures. In *Proc. of the IUTAM Symp. on Boundary-Layer Separation*, eds. F. T. Smith & S. N. Brown, 73-87. Springer-Verlag

Van Dommelen, L.L. 1989 On the Lagrangian description of unsteady boundary-layer separation. Part 2: the spinning sphere. Submitted to the *J. Fluid Mech.*

Van Dommelen, L.L. & Shen, S.F. 1977 Presented at XIIIth Symp. Bienn. Symp. Adv. Meth. Prob. Fluid Mech., Olsztyn-Kortewo, Poland.

Van Dommelen, L.L. & Shen, S.F. 1980a The spontaneous generation of the singularity in a separating laminar boundary layer. *J. Comp. Phys.* 38, 125-140.

Van Dommelen, L.L. & Shen, S.F. 1980b The birth of separation. Presented at the XVth

Int. Cong. Theo. Appl. Mech., IUTAM, Toronto, Canada.

Van Dommelen, L.L. & Shen, S.F. 1982 The genesis of separation. In *Numerical and Physical Aspects of Aerodynamic Flows*, ed. T. Cebeci. Springer-Verlag.

Van Dommelen, L.L. & Shen, S.F. 1983a Boundary-layer separation singularities for an upstream moving wall. *Acta Mech.* **49**, 241-254.

Van Dommelen, L.L. & Shen, S.F. 1983b An unsteady interactive separation process. *AIAA J.* **21**, 358-362.

Van Dyke, 1975 *Perturbation methods in fluid mechanics*. The Parabolic Press, Stanford, CA, 86.

Vasantha, R. & Riley, N. 1988 On the initiation of jets in oscillatory viscous flows. *Proc. R. Soc. Lond.* **A419**, 363-378.

Walker, J.D.A. 1988 Mechanism of turbulence production near a wall. ICOMP seminar series, NASA-Lewis, July 26, 1988.

Wang, K.C. 1979 Unsteady boundary-layer separation. Martin Marietta Lab., Baltimore, Maryland, USA, Tech. Rept. MML TR 79-16c.

Wang, K.C. & Fan, Z.Q. 1982 Unsteady symmetry-plane boundary layers and three-dimensional unsteady separation. Part I. High incidence. San Diego State Univ. Tech. Rep. AE&EM TR-82-01.

Wu, T, 1988 Ph.D. dissertation, Cornell University.

Williams, J.C. 1977 Incompressible boundary-layer separation. *Ann. Rev. Fluid Mech.* **9**, 113.

Williams, J.C. & Stewartson, K. 1983 Flow development in the vicinity of the trailing edge on bodies impulsively set into motion. Part 2. *J. Fluid Mech.* **131**, 177.

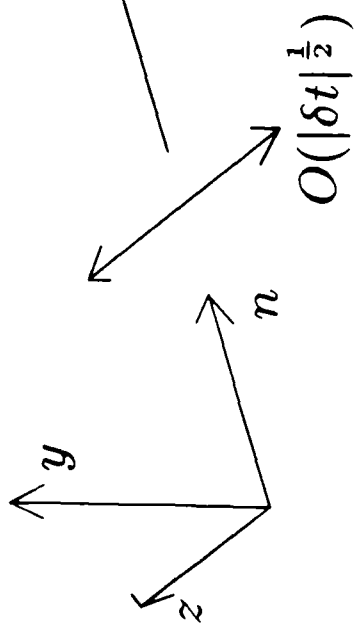
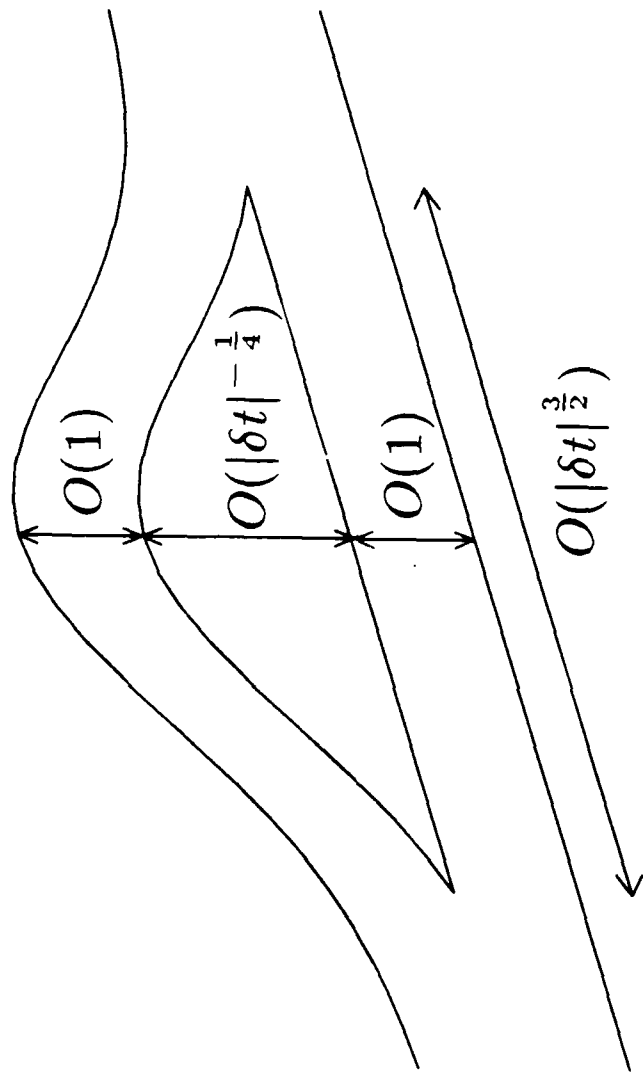
Figure 1. Structure of the separating boundary layer, illustrating the asymptotic scalings in the boundary-layer coordinate system (schematic).

Figure 2. Structure of asymmetric three-dimensional separation: (a) Lagrangian topology of vertical lines through the boundary layer near the separation particle; (b) contours of the scaled boundary-layer thickness $\tilde{Y}^+ = 5\frac{1}{2}, 5, 4\frac{1}{2}, \dots, 2\frac{1}{2}$ in scaled, oblique coordinates; (c) possible actual appearance of contours of boundary-layer thickness (schematic); (d) contours of the scaled velocity $L_1^* = 0, \pm 1, \pm 2, \dots$ in scaled coordinates; (e) $-L_1^*$ velocity-profiles; (f) contours of the scaled vorticity $dL_1^*/dY^* = 0, \pm 1, \pm 2, \dots$; (g) topology of vertical lines through the boundary layer for times beyond the first singularity.

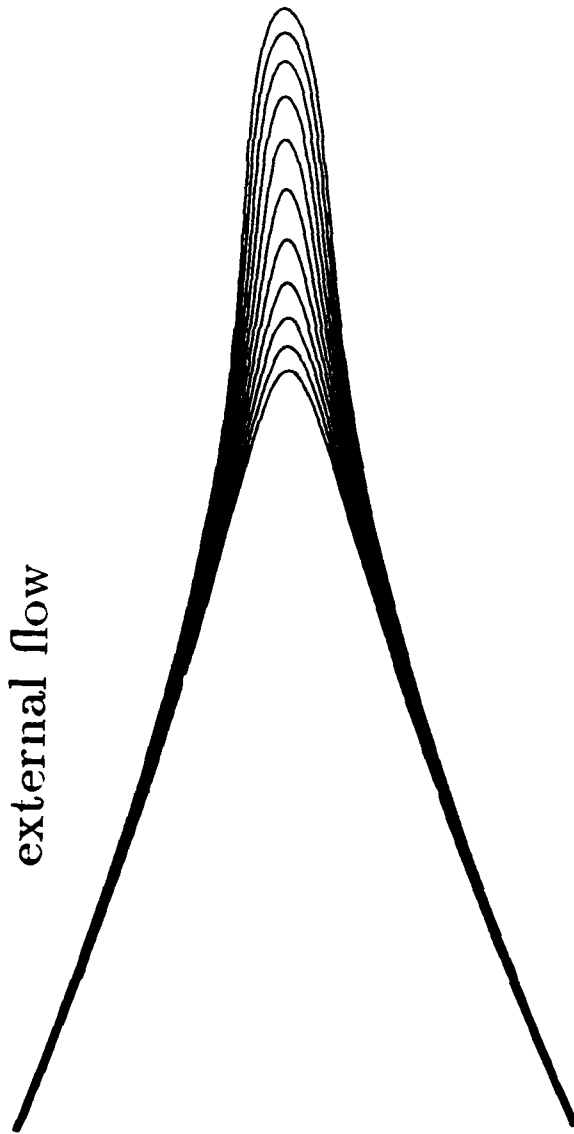
Figure 3. Structure of symmetric three-dimensional separation: (a) Lagrangian topology of physically vertical lines; (b) contours of boundary-layer thickness $\tilde{Y}^+ = 3\frac{1}{2}, 3, 2\frac{1}{2}, \dots, 1$; (c) $-L_1^*$ velocity-profiles; (d) contours of $L_1^* = 0, \frac{1}{2}, 1, 1\frac{1}{2}, \dots$; (e) contours of $dL_1^*/dY^* = 0, \pm 1, \pm 2, \dots$; (f) L_2^* velocity-profiles for flow parallel to the symmetry plane; (g) contours of $L_2^* = 0, \pm 1, \pm 2, \dots$; (h) contours of $dL_2^*/dY^* = 1, 2, 3, \dots$; (i) Lagrangian topology of physically vertical lines beyond the first singularity.

Figure 4. Structure of axi-symmetric separation with swirl: (a) Lagrangian topology of physically vertical lines; (b) the velocity profiles of the two components $-U_0^*$ and W_0^* ; (c) contours of the scaled absolute velocity $P^* = 0, \frac{1}{2}, 1, 1\frac{1}{2}, \dots$; (d) contours of the scaled vorticity component normal to the flow velocity $\Omega_n = 0, \pm 1, \pm 2, \dots$; (e) contours of the scaled vorticity component parallel to the velocity $\Omega_p = 0, -1, -2, \dots$; (f) Lagrangian topology of physically vertical lines beyond the first singularity.

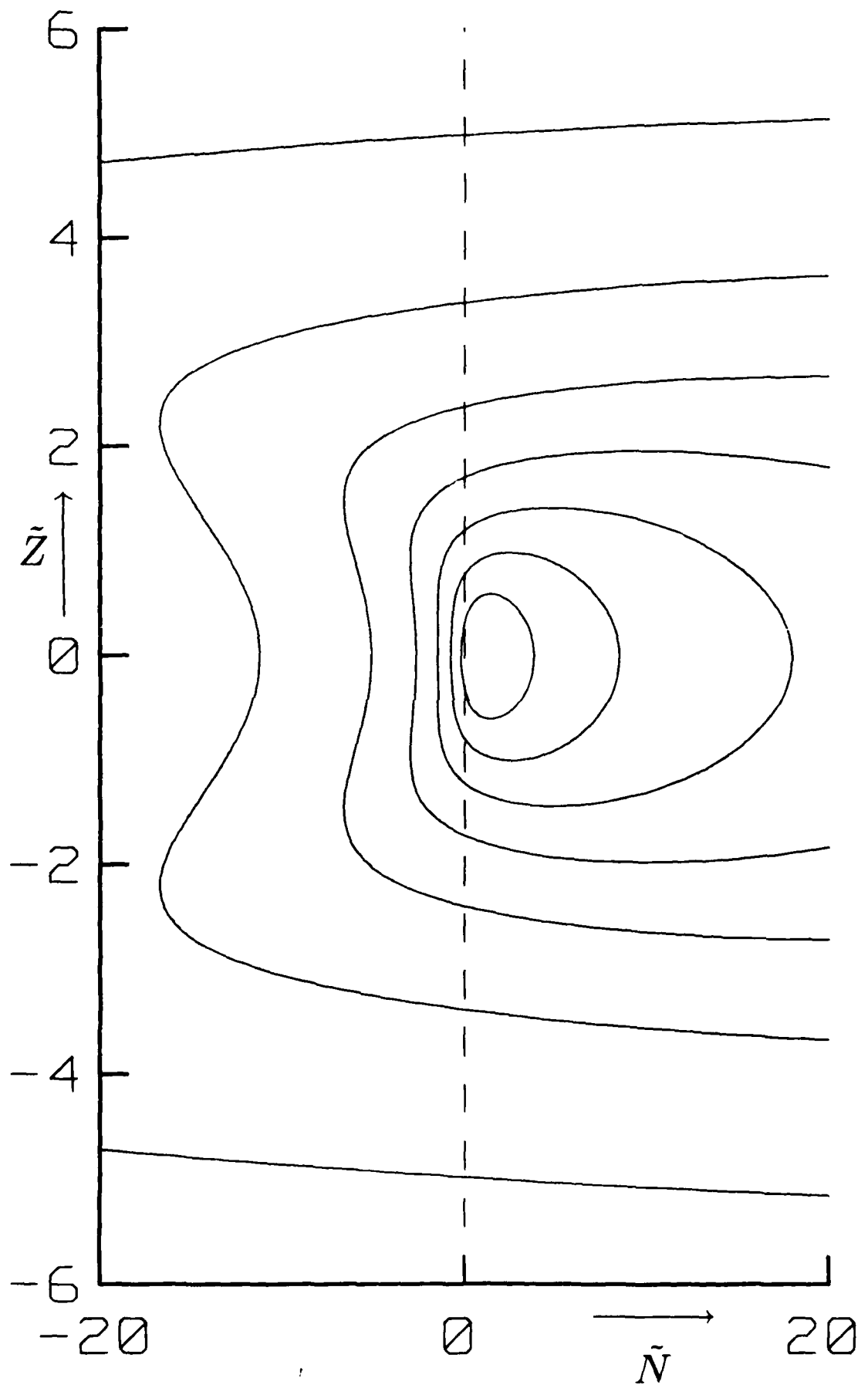
Figure 5. Structure of axi-symmetric separation without swirl: (a) P^* velocity-profiles; (b) contours of $P^* = 0, \frac{1}{2}, 1, 1\frac{1}{2}, \dots$; (c) contours of $dP^*/dY^* = 0, \pm 1, \pm 2, \dots$

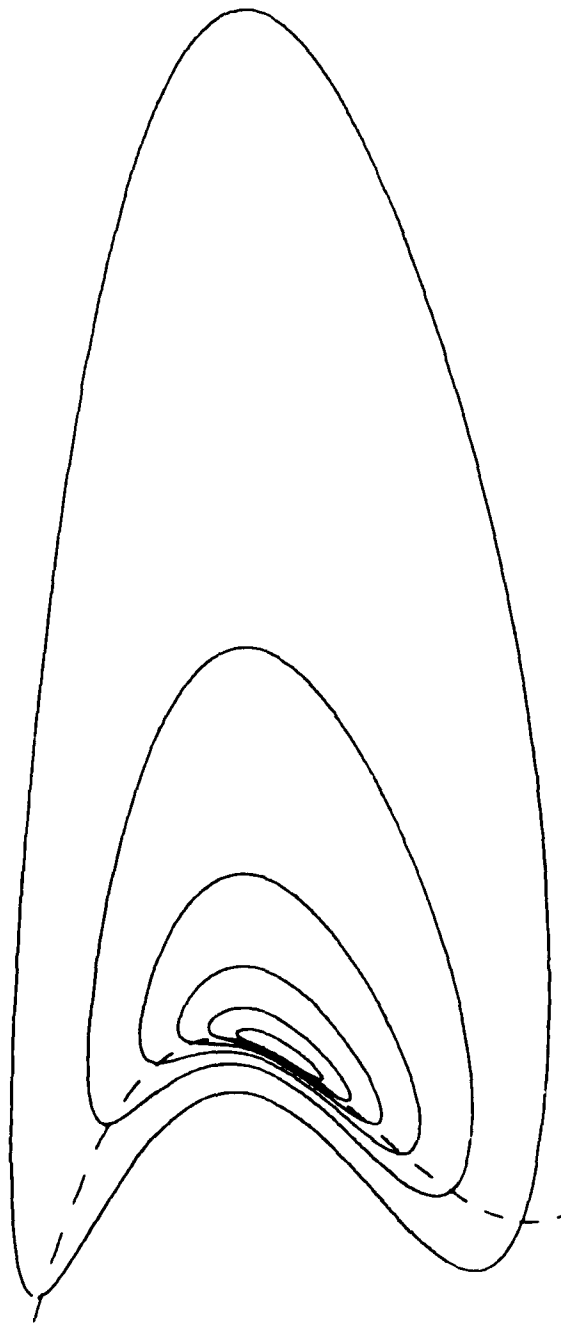


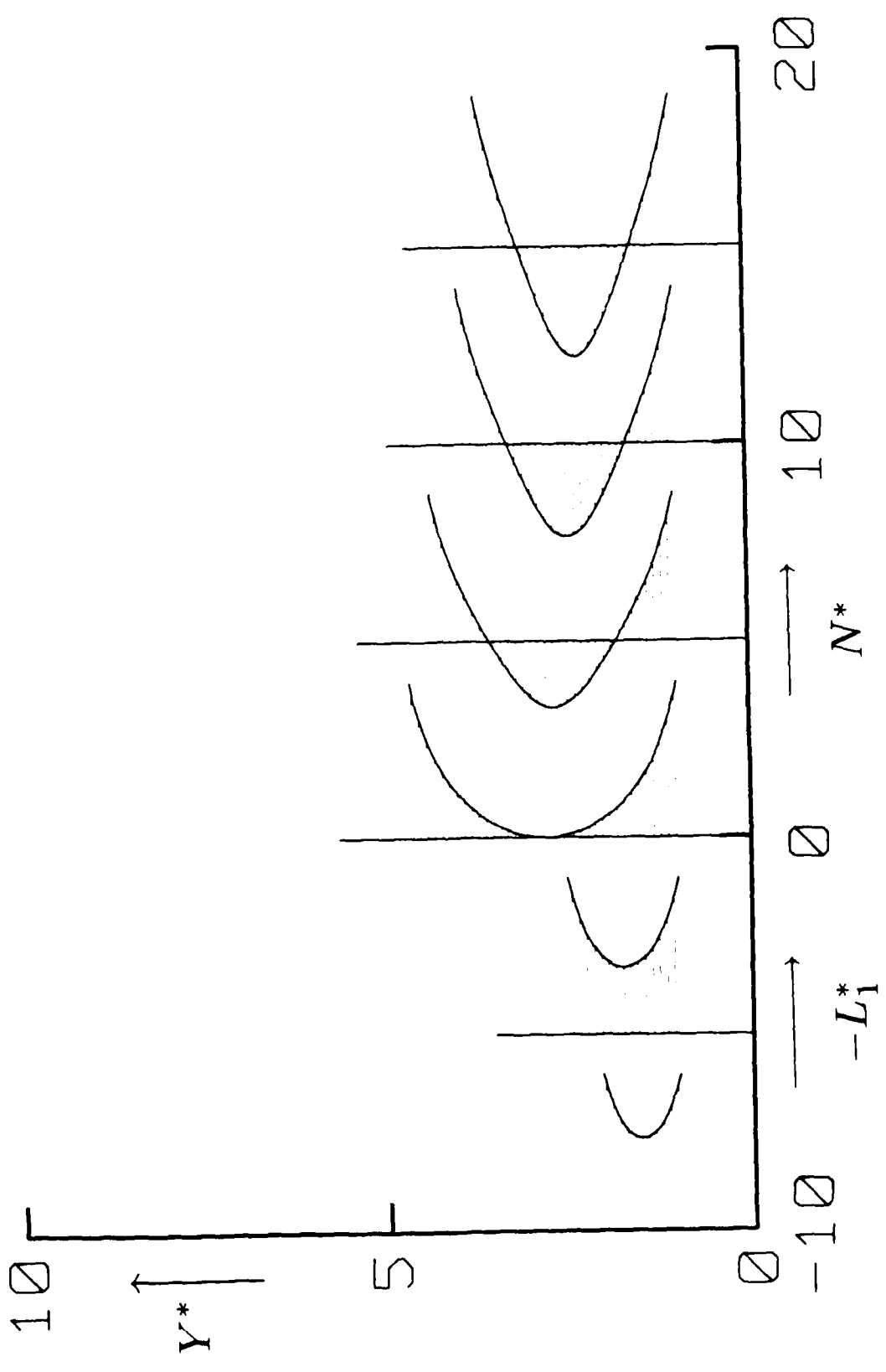
toward the
external flow

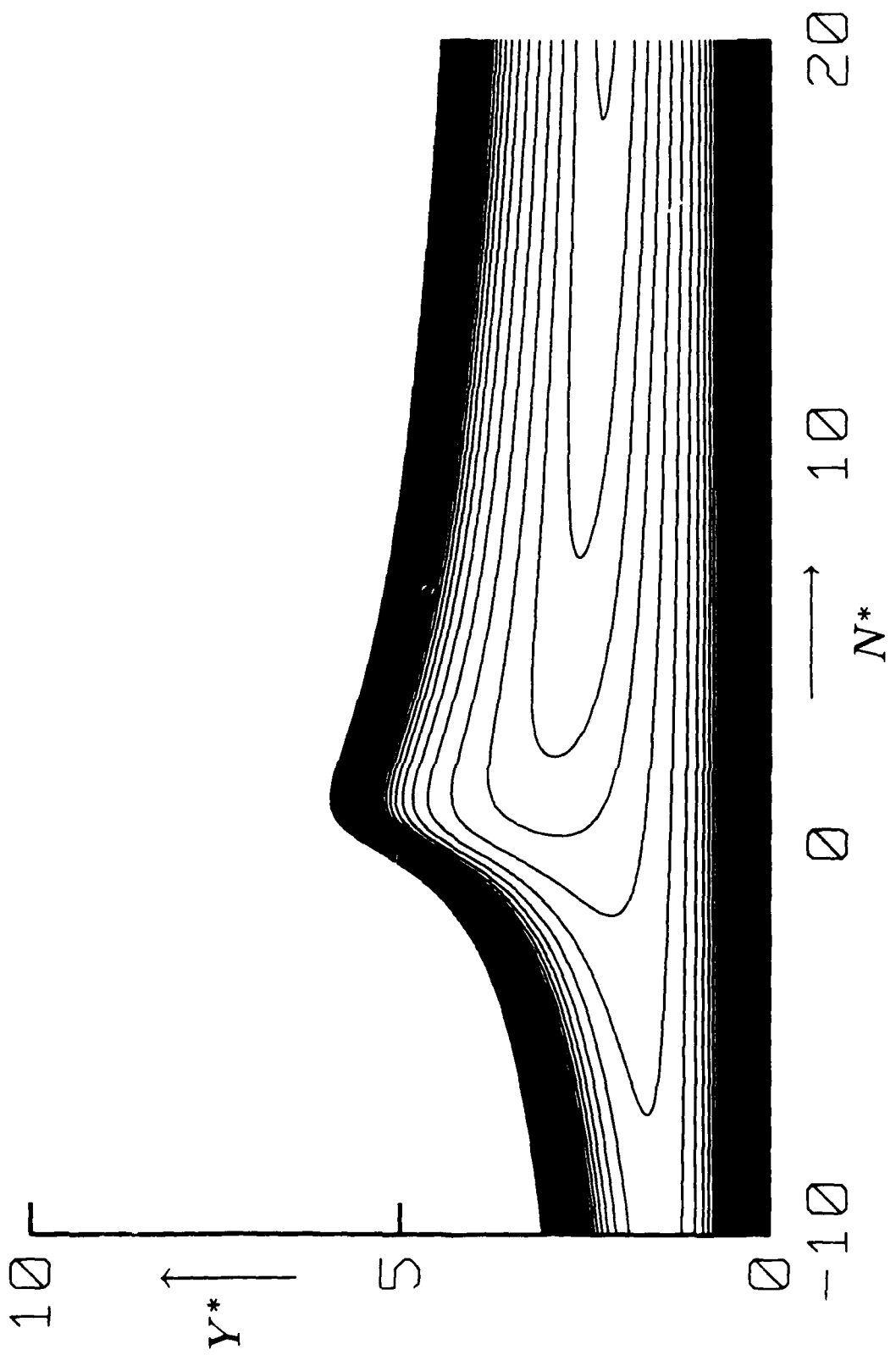


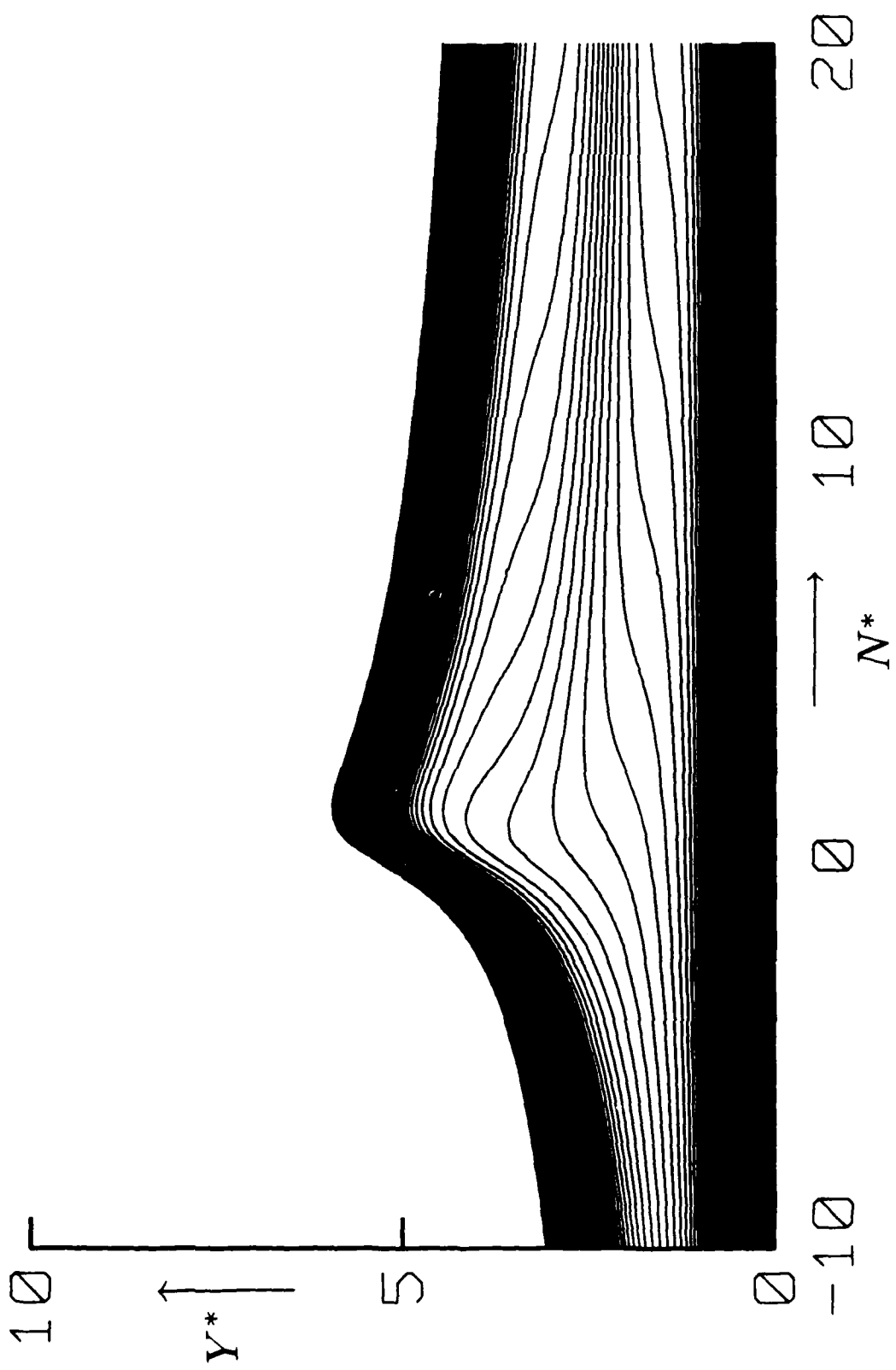
toward the wall



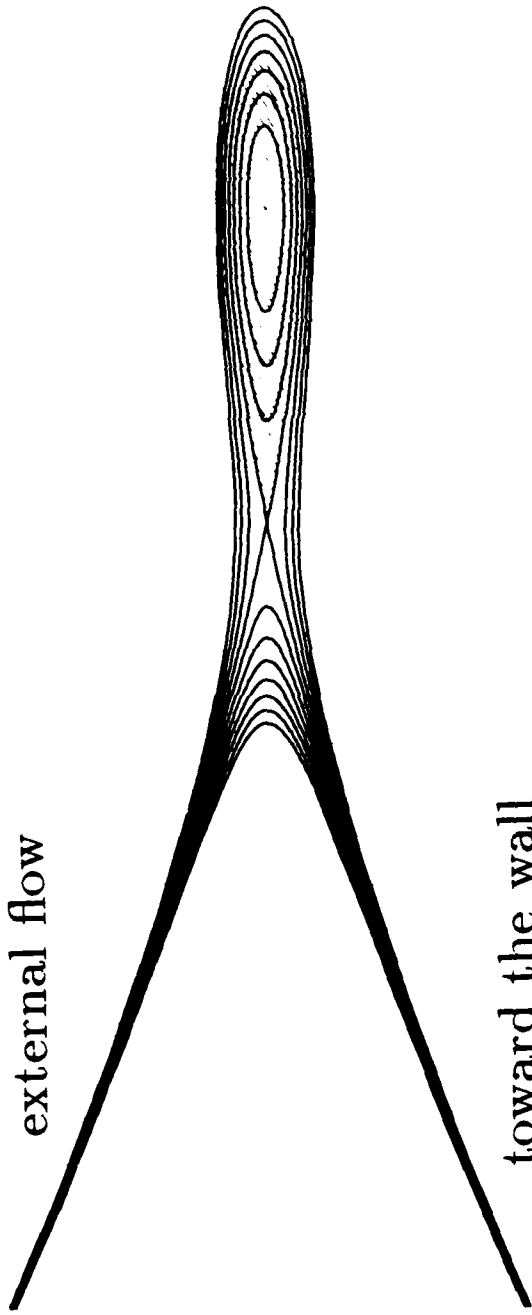






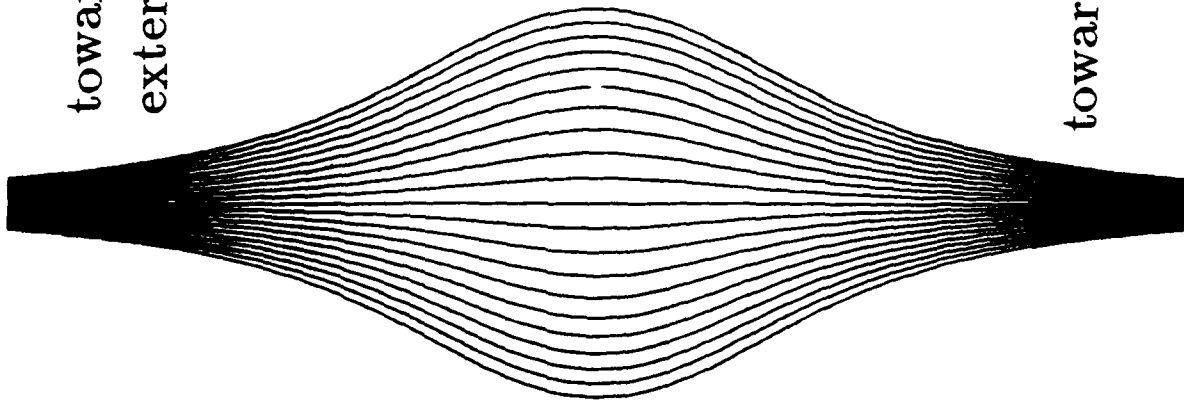


toward the
external flow

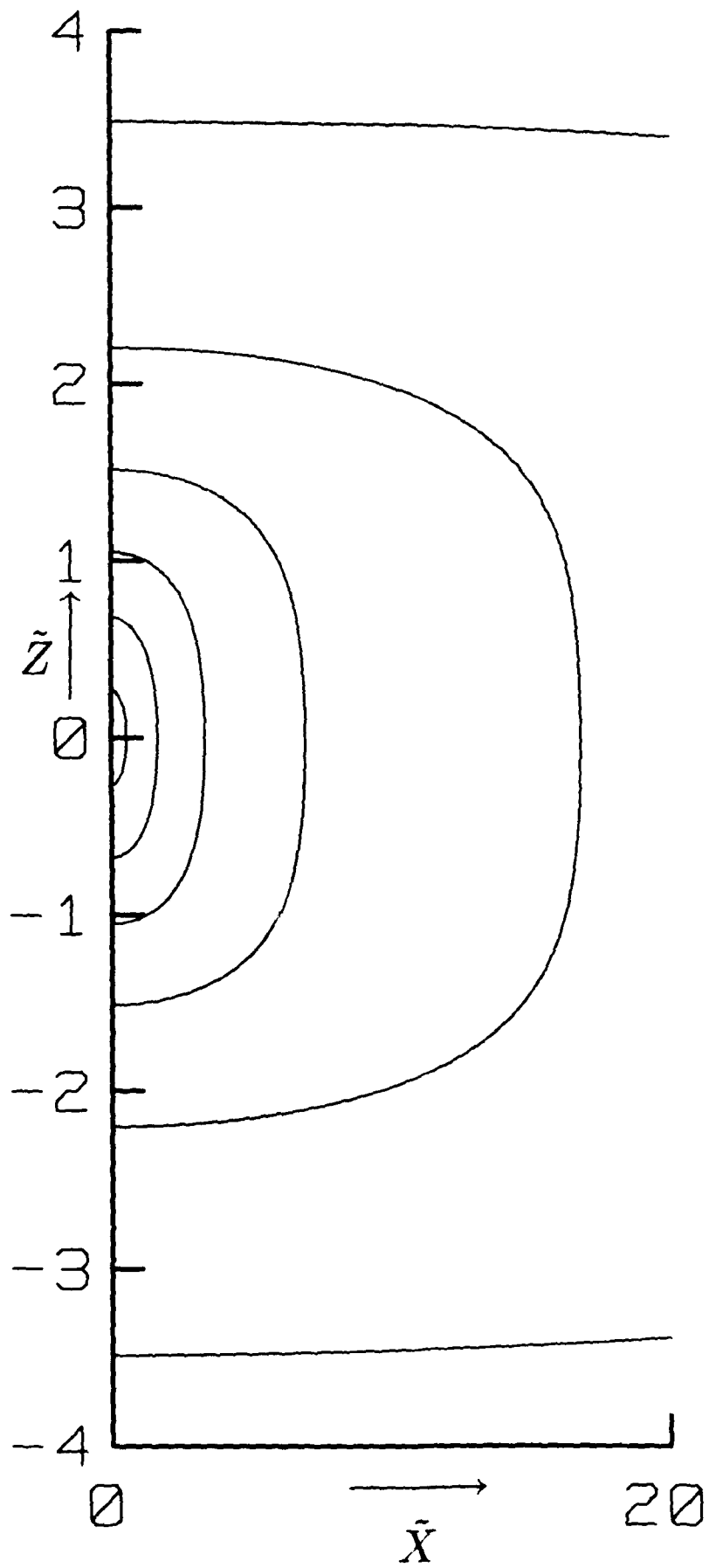


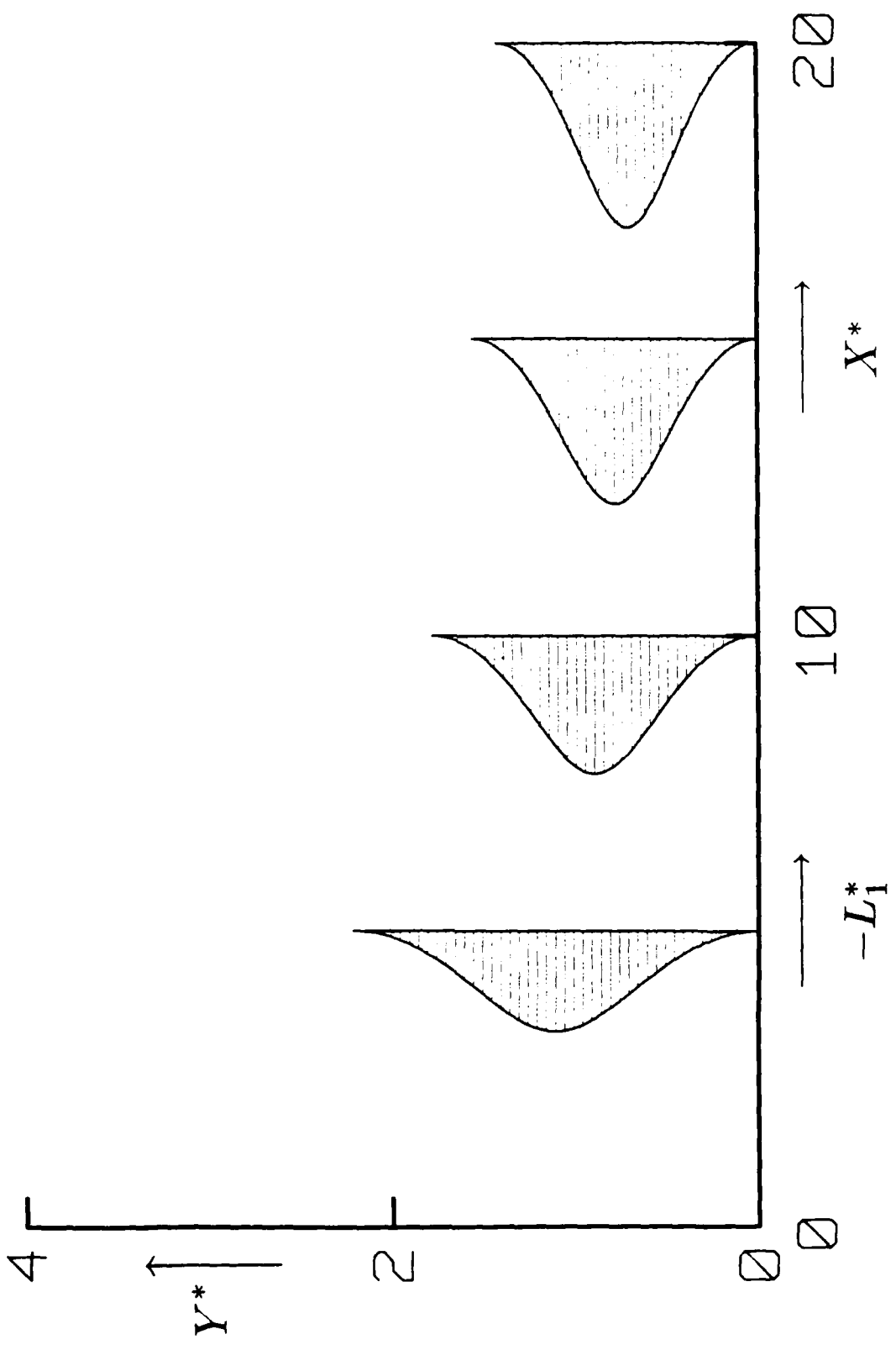
toward the wall

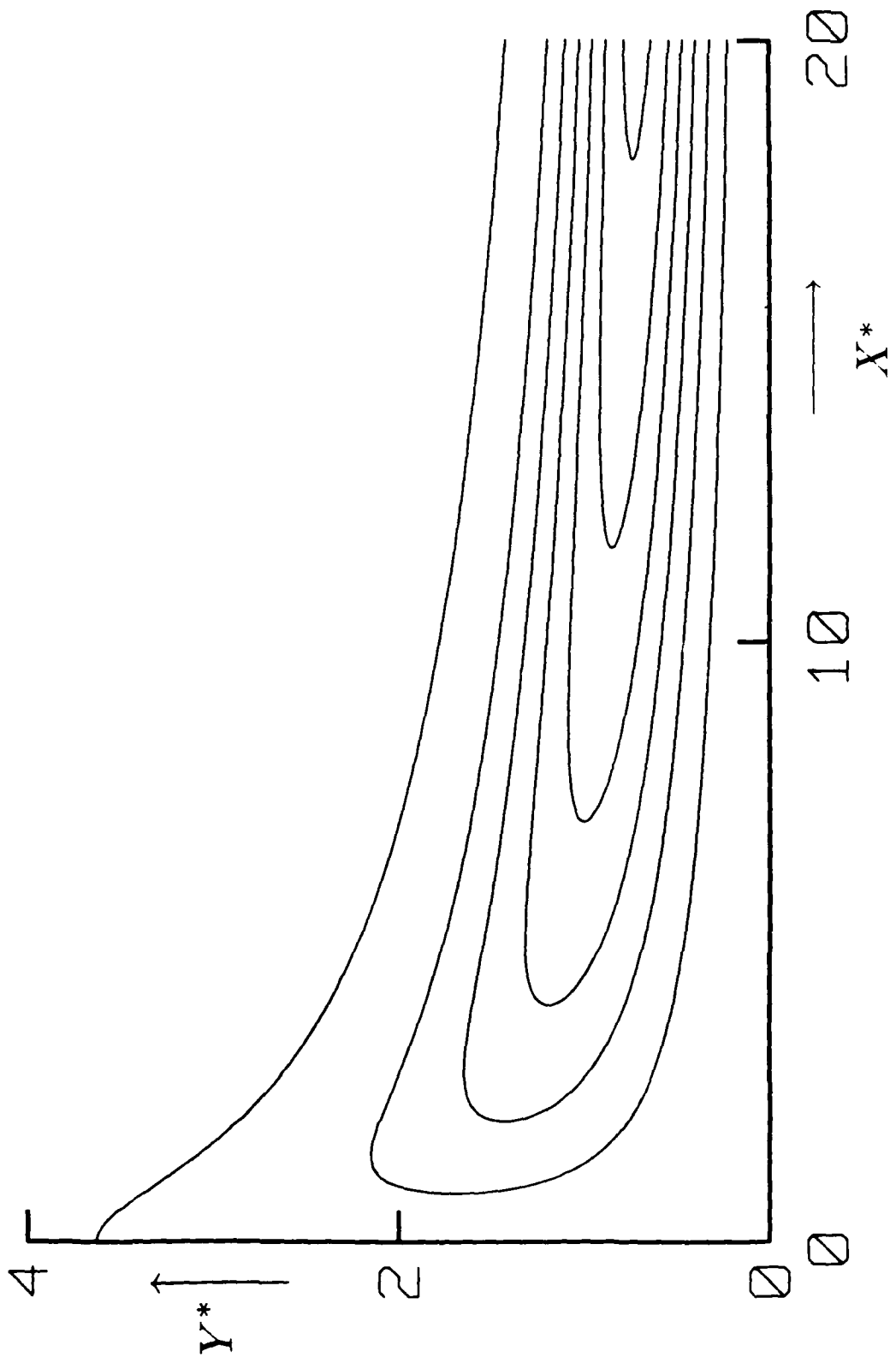
toward the
external flow

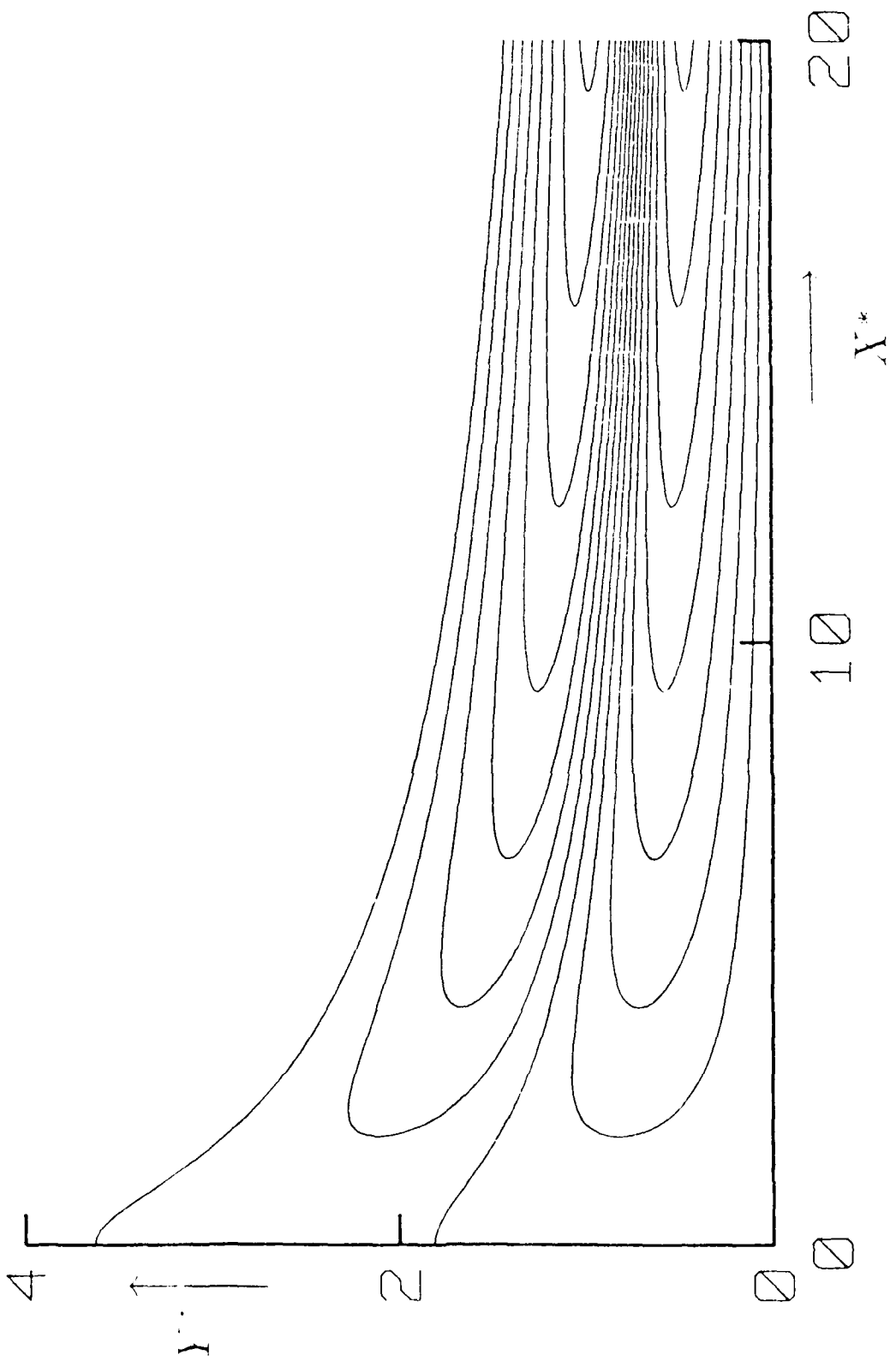


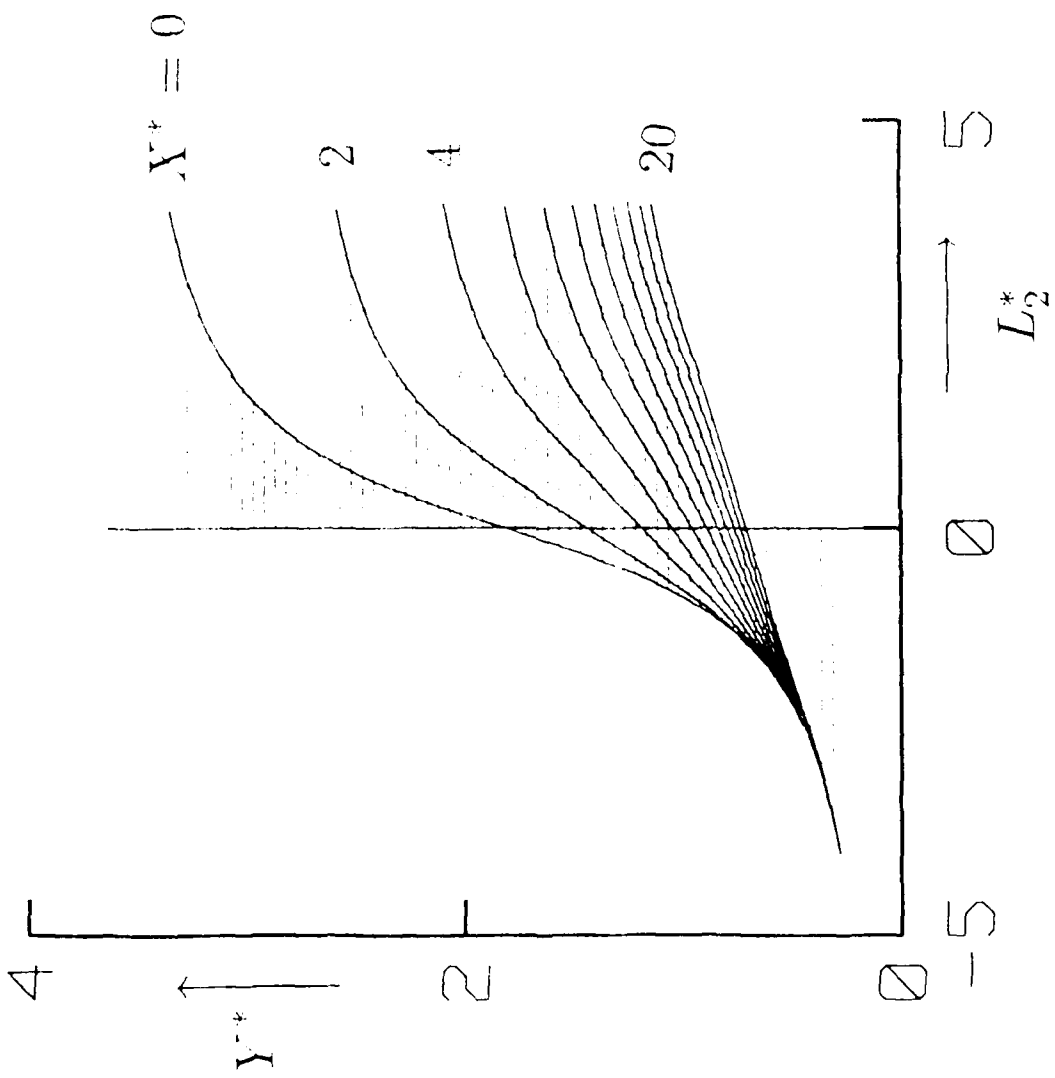
toward the wall

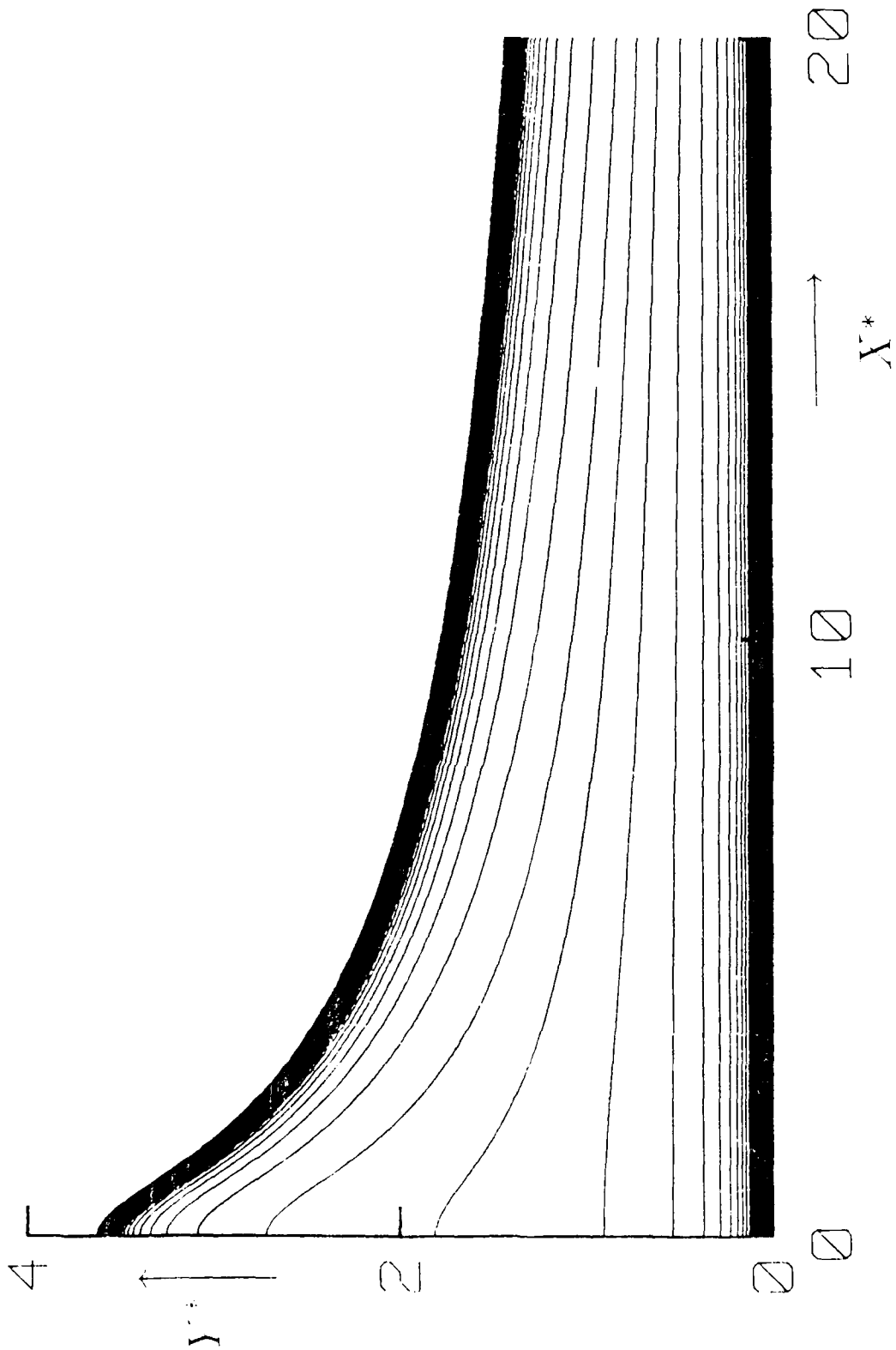


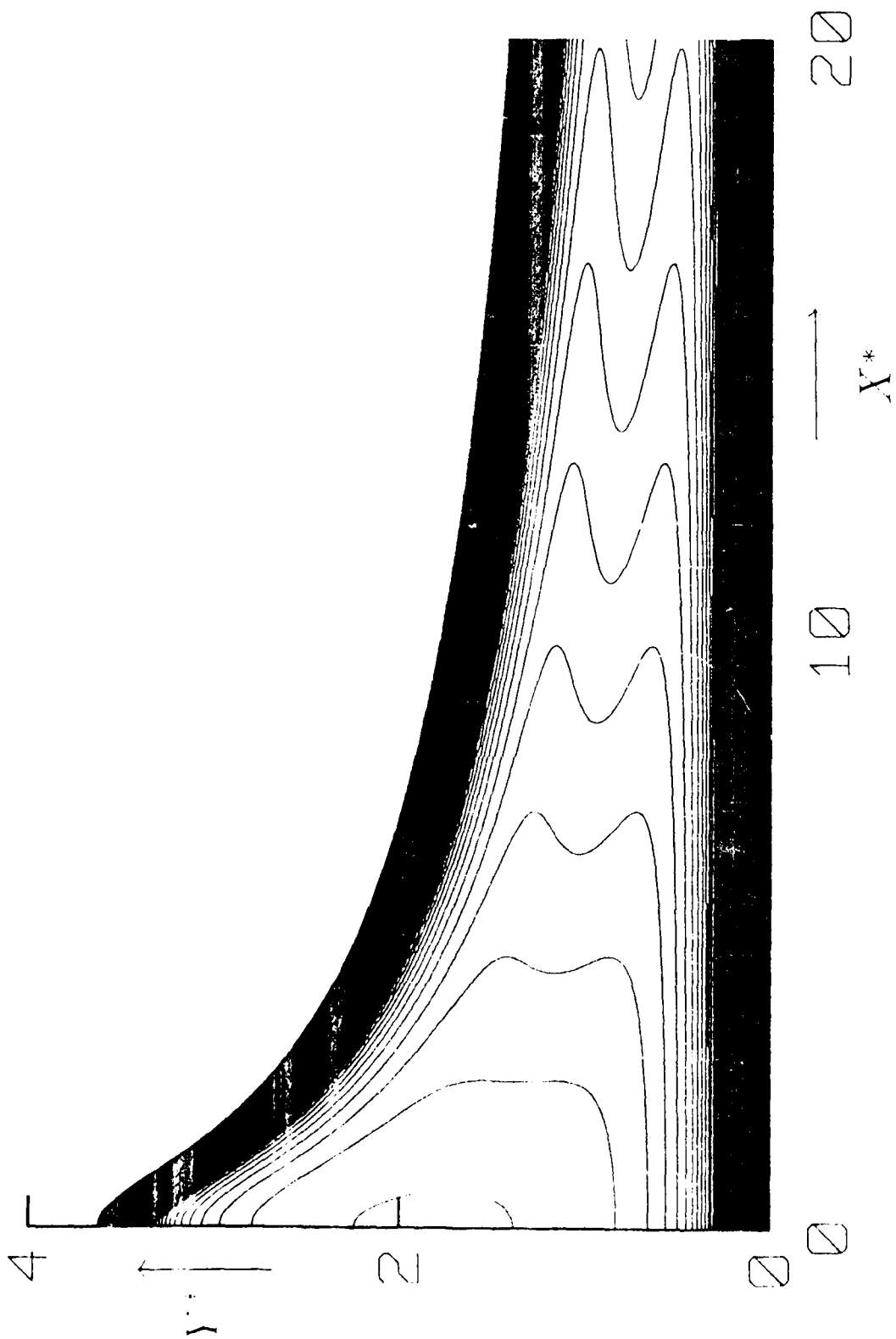


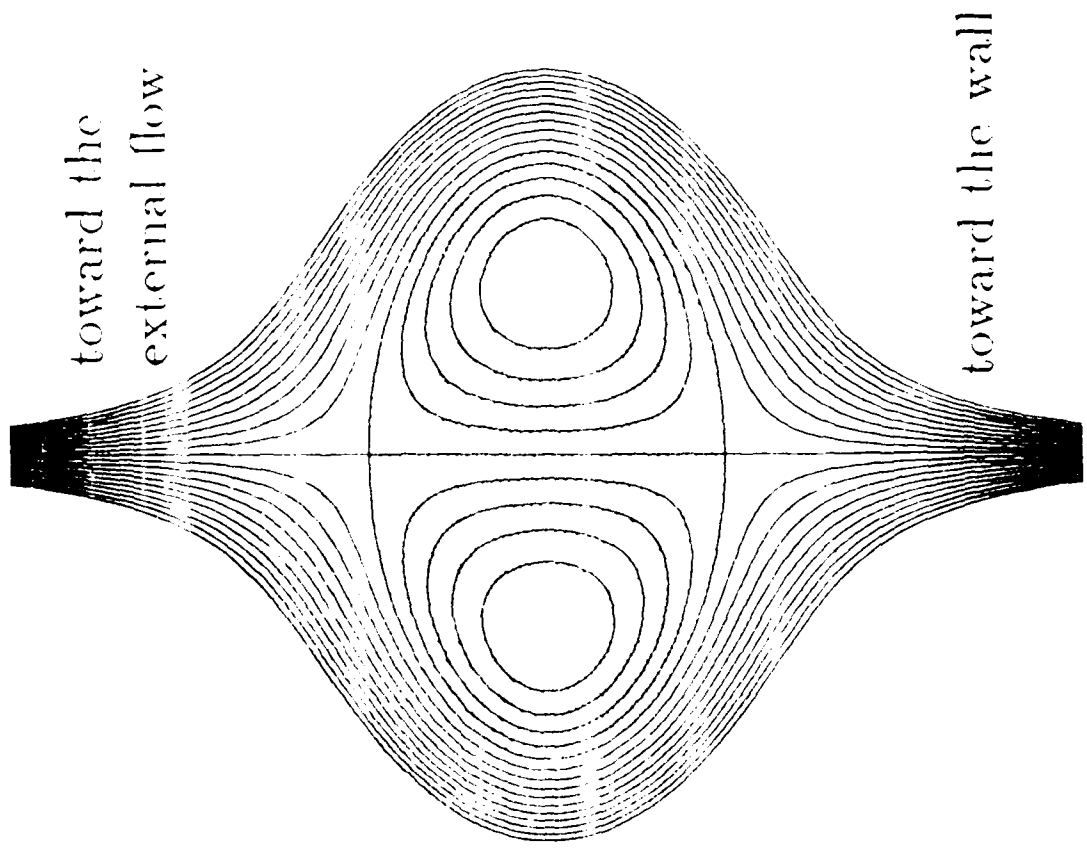






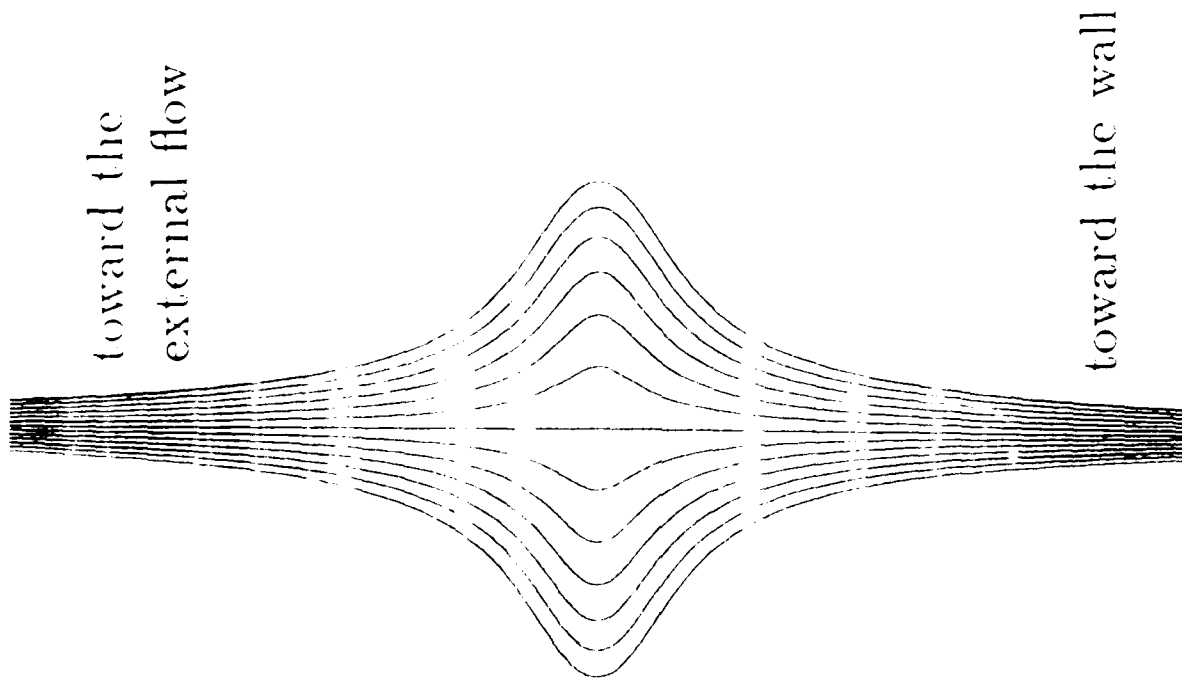


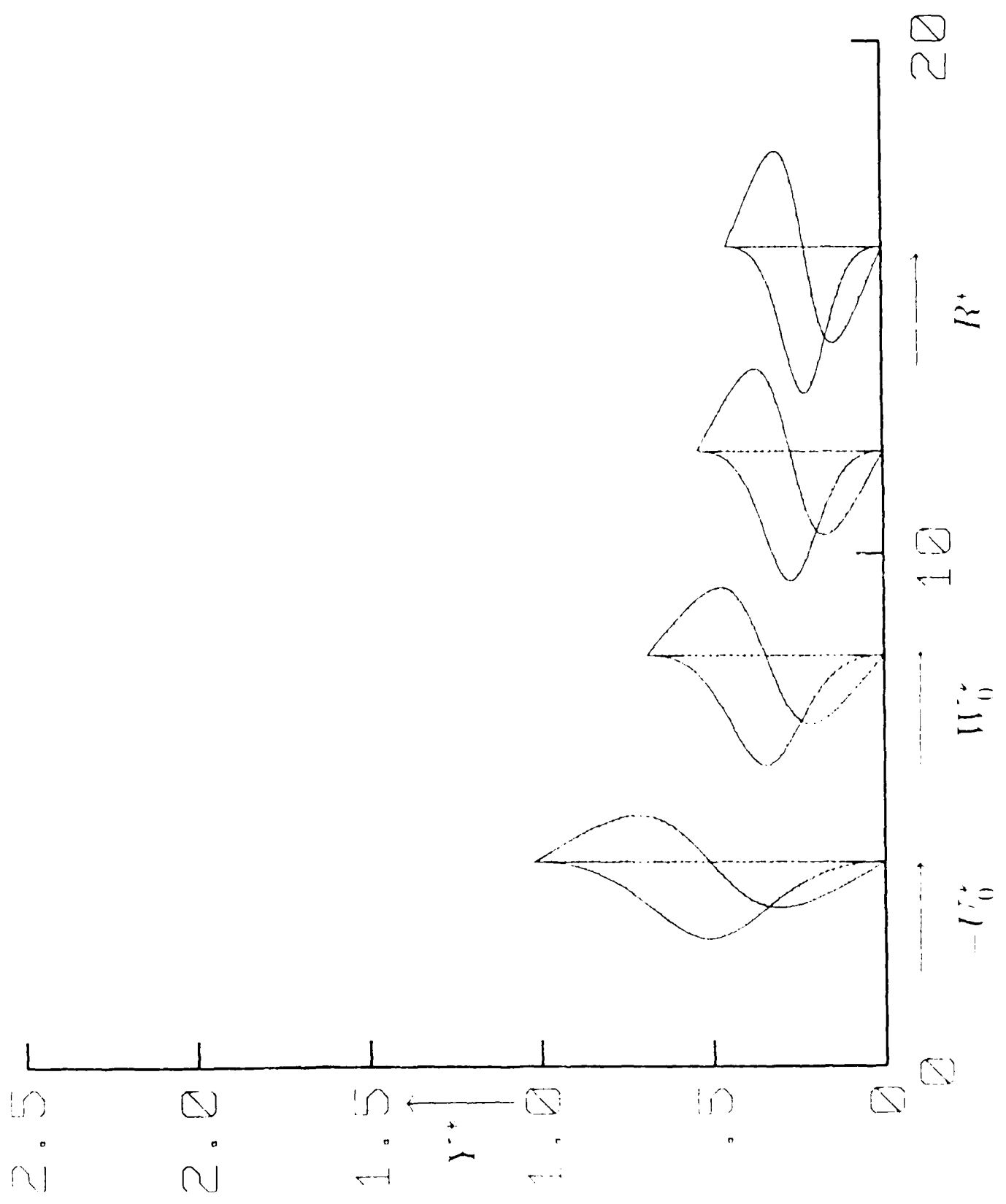




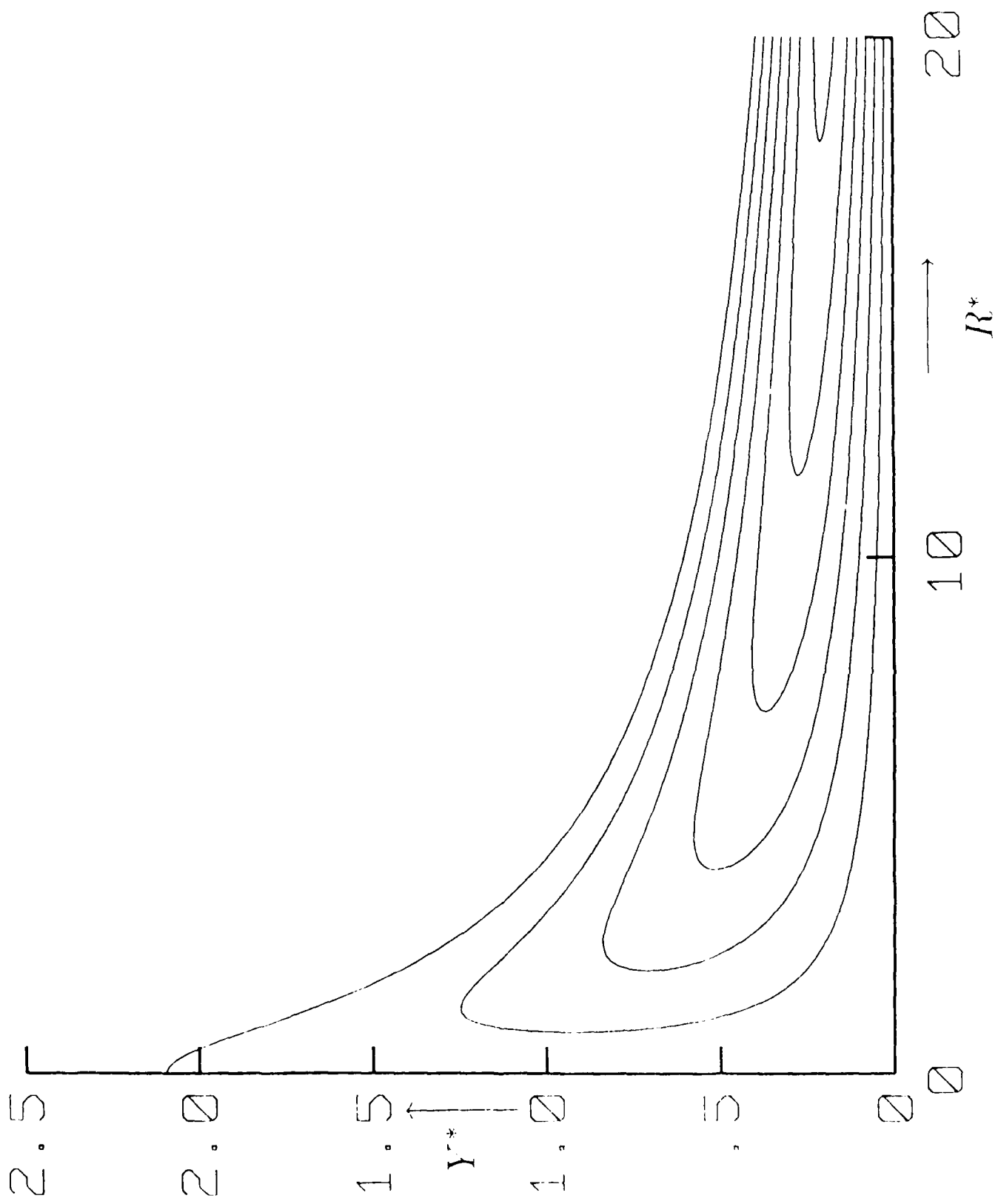
toward the
external flow

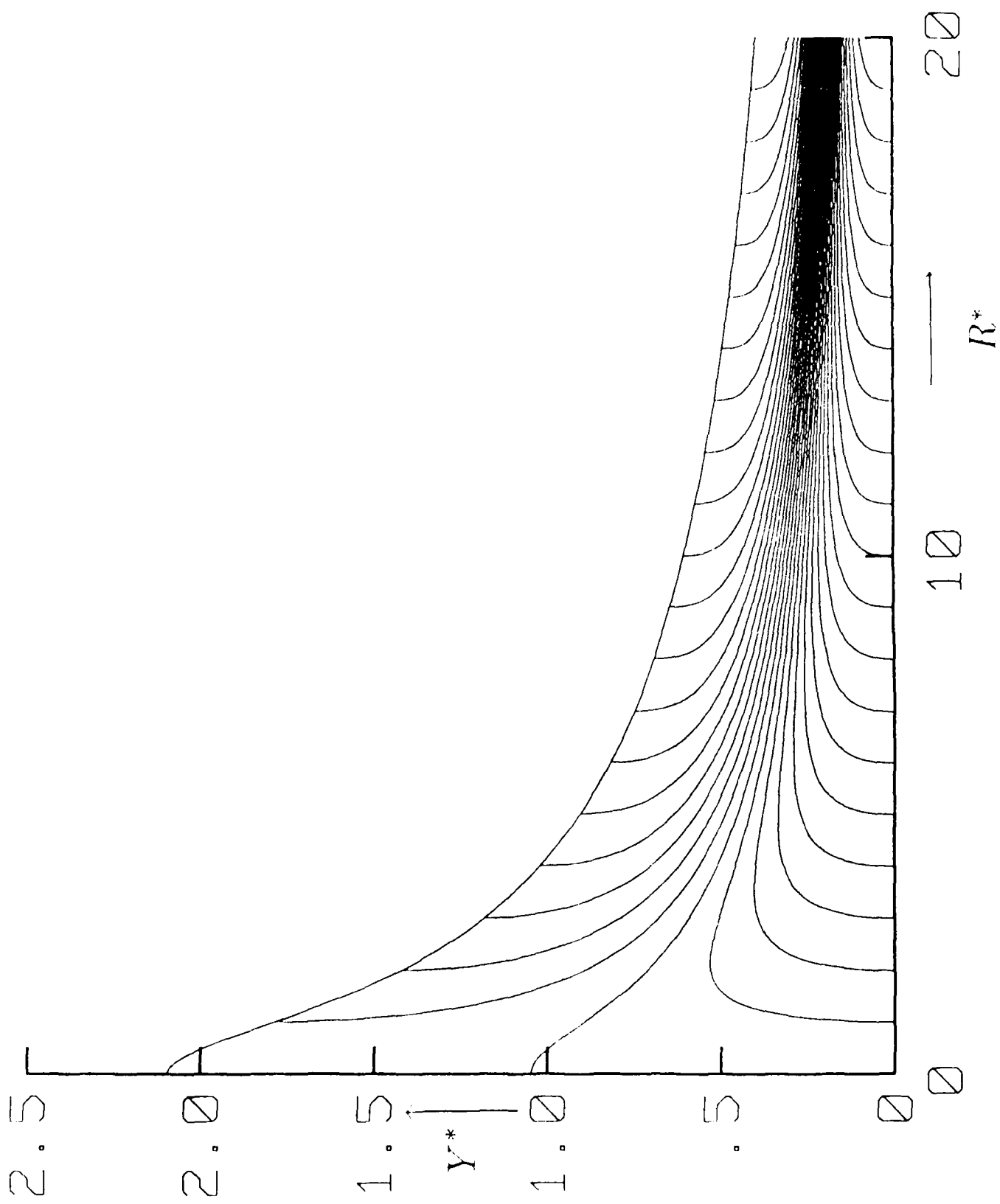
toward the wall

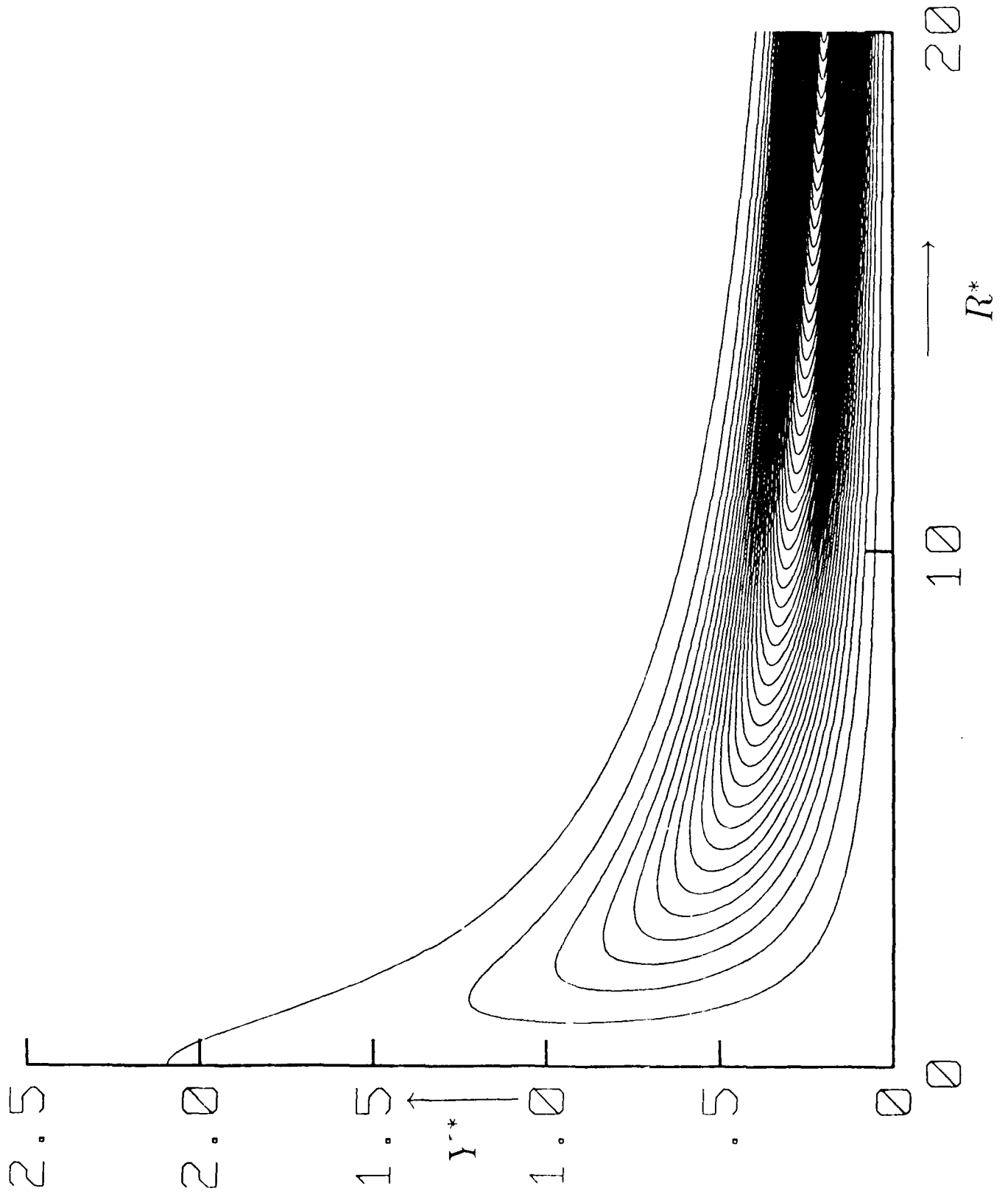




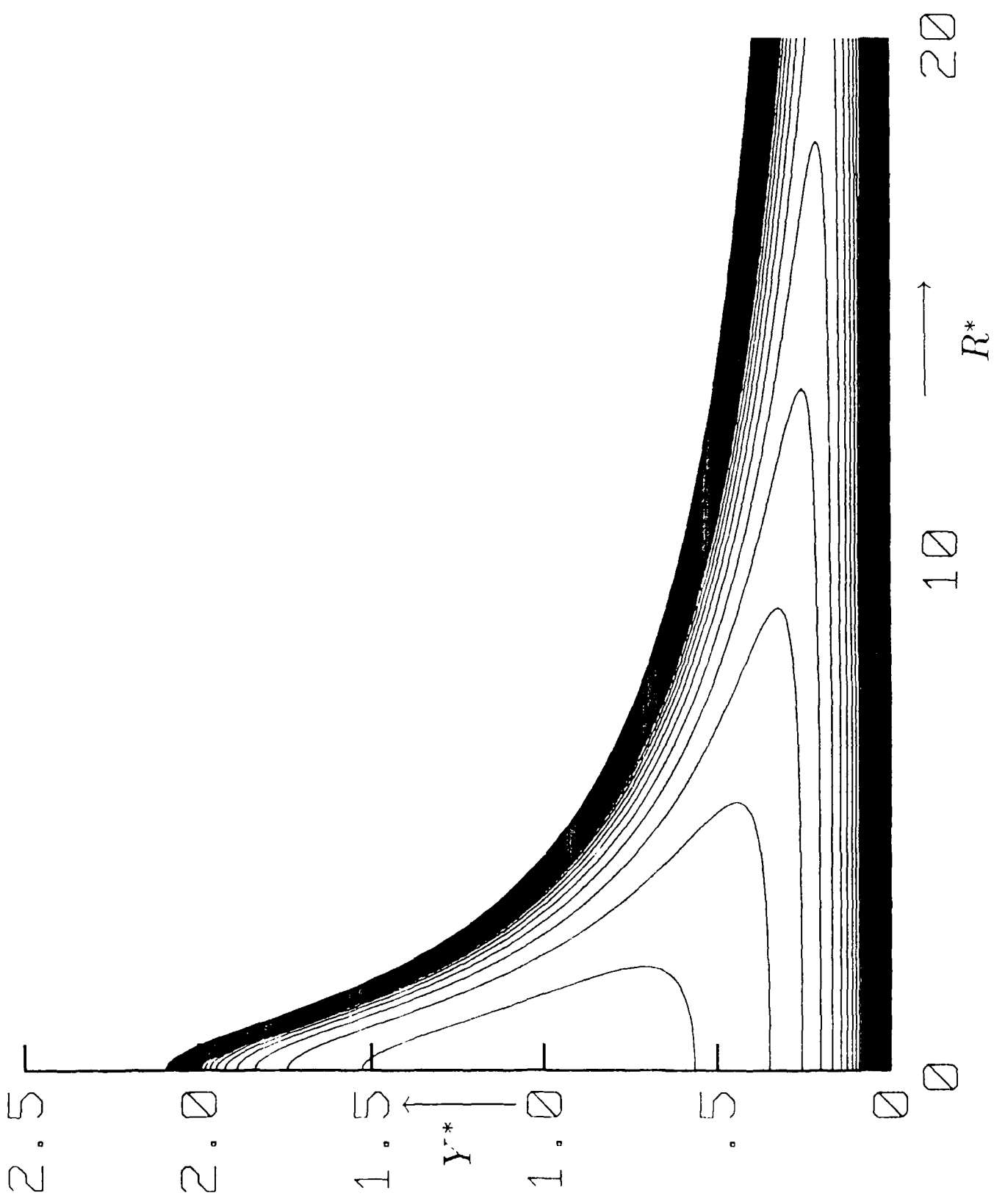
117





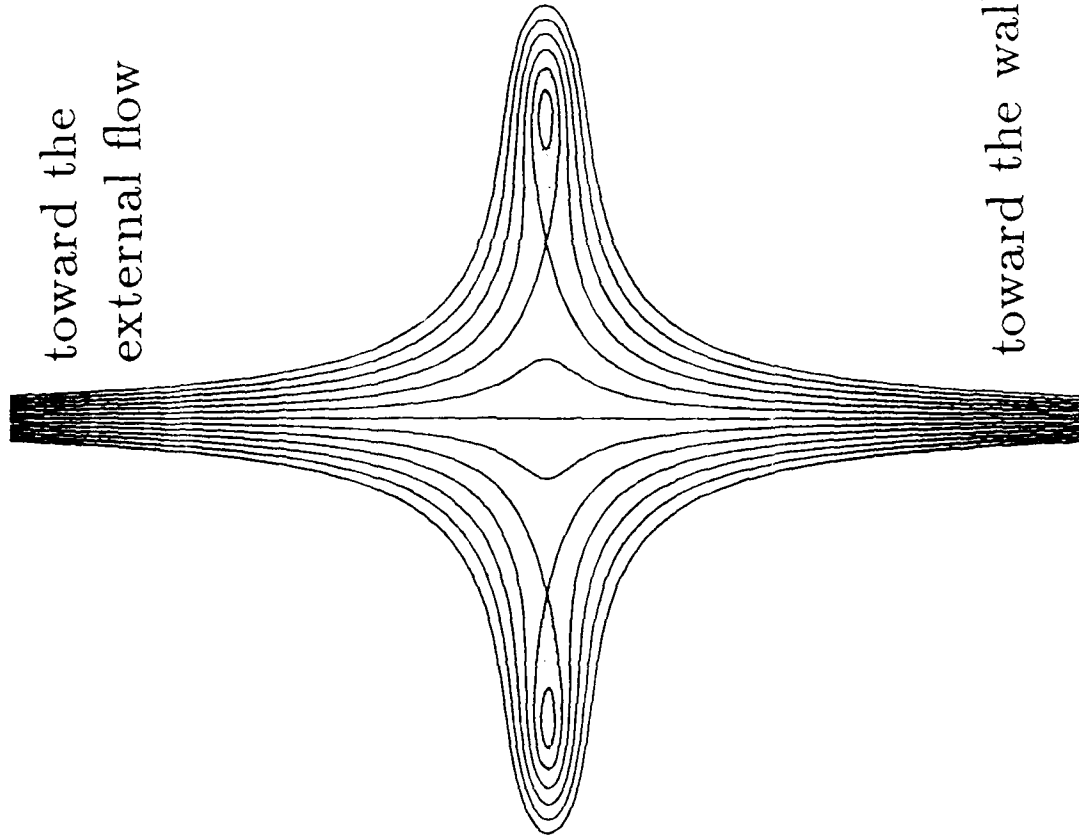


2.2

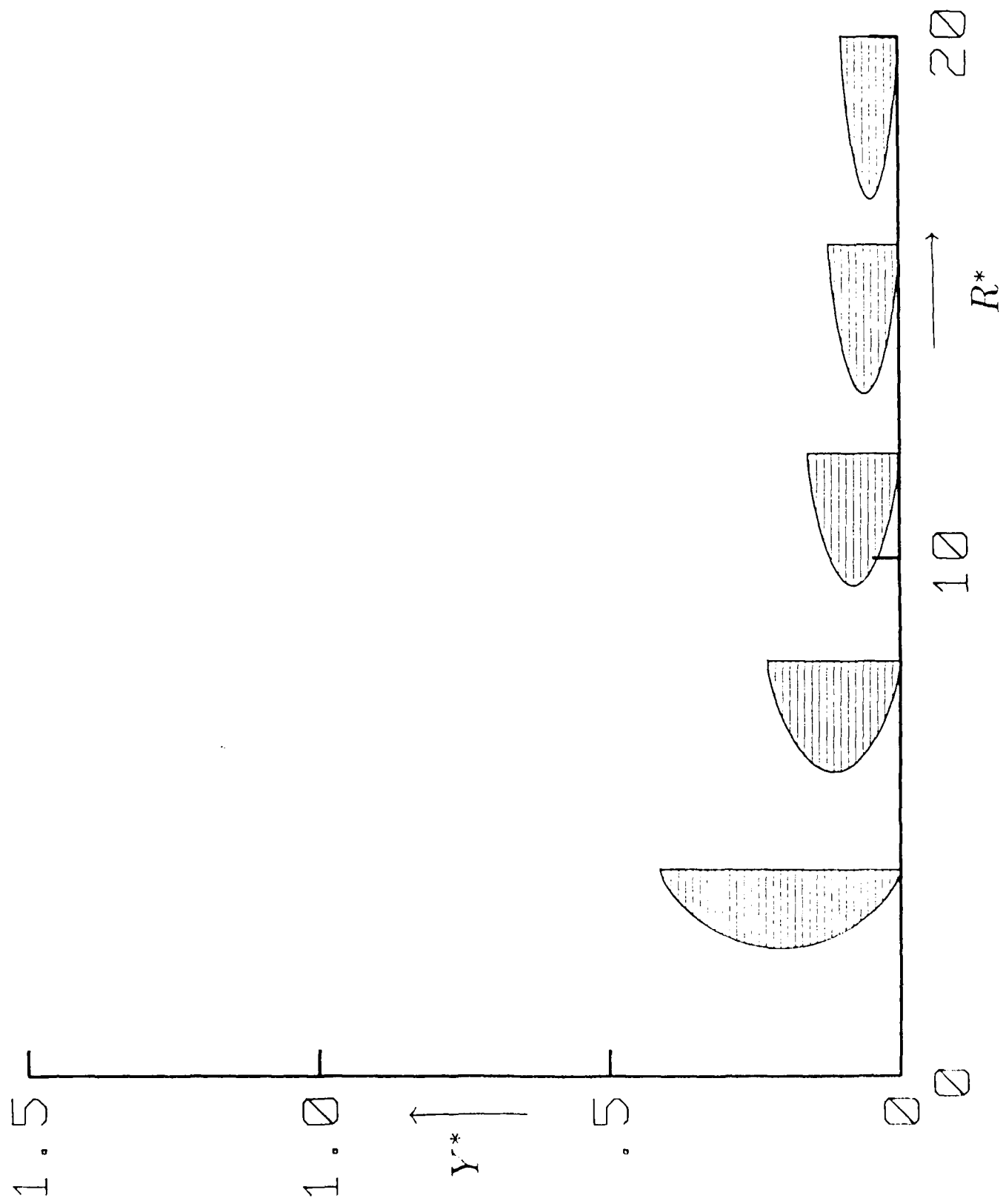


50

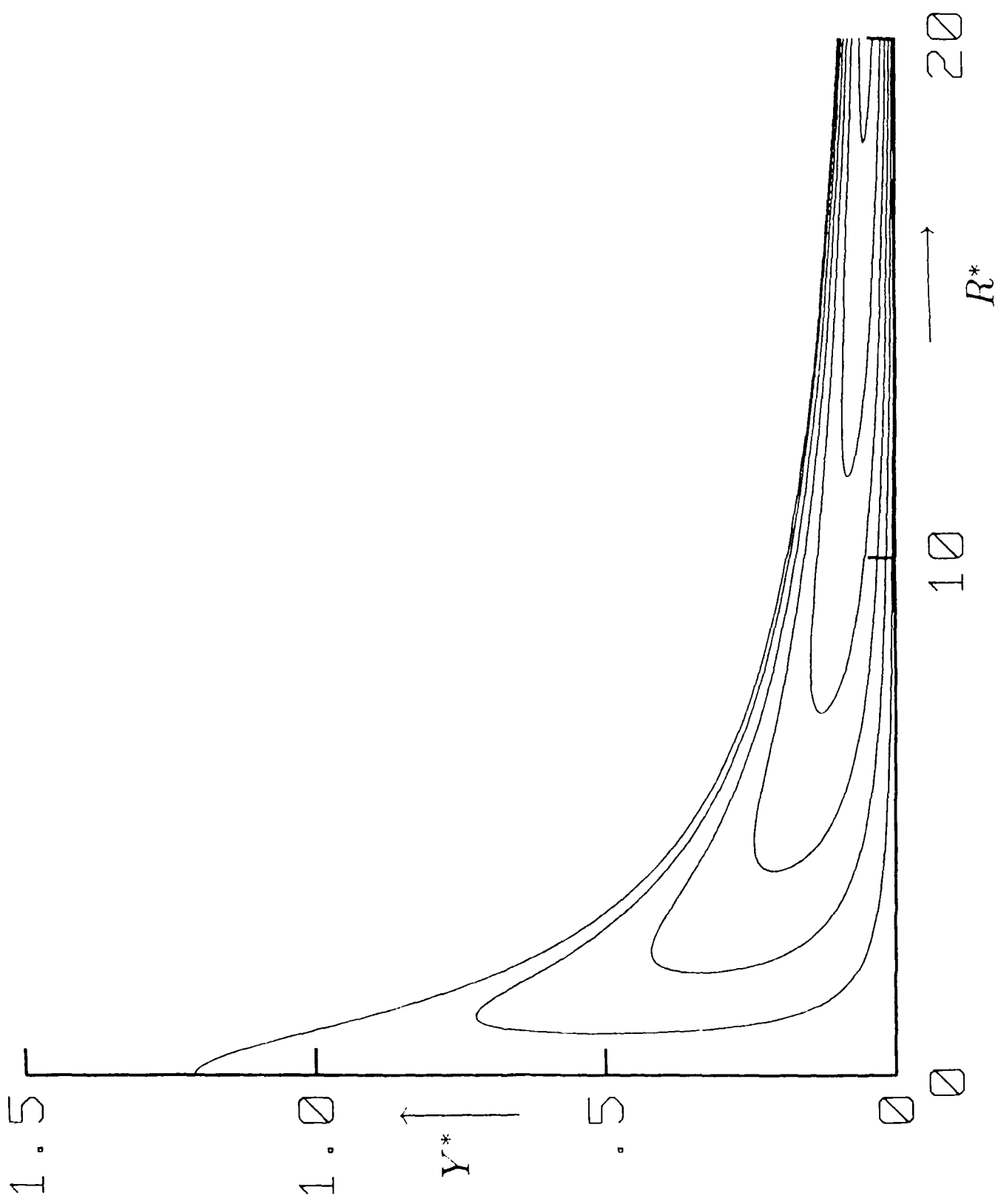
toward the
external flow



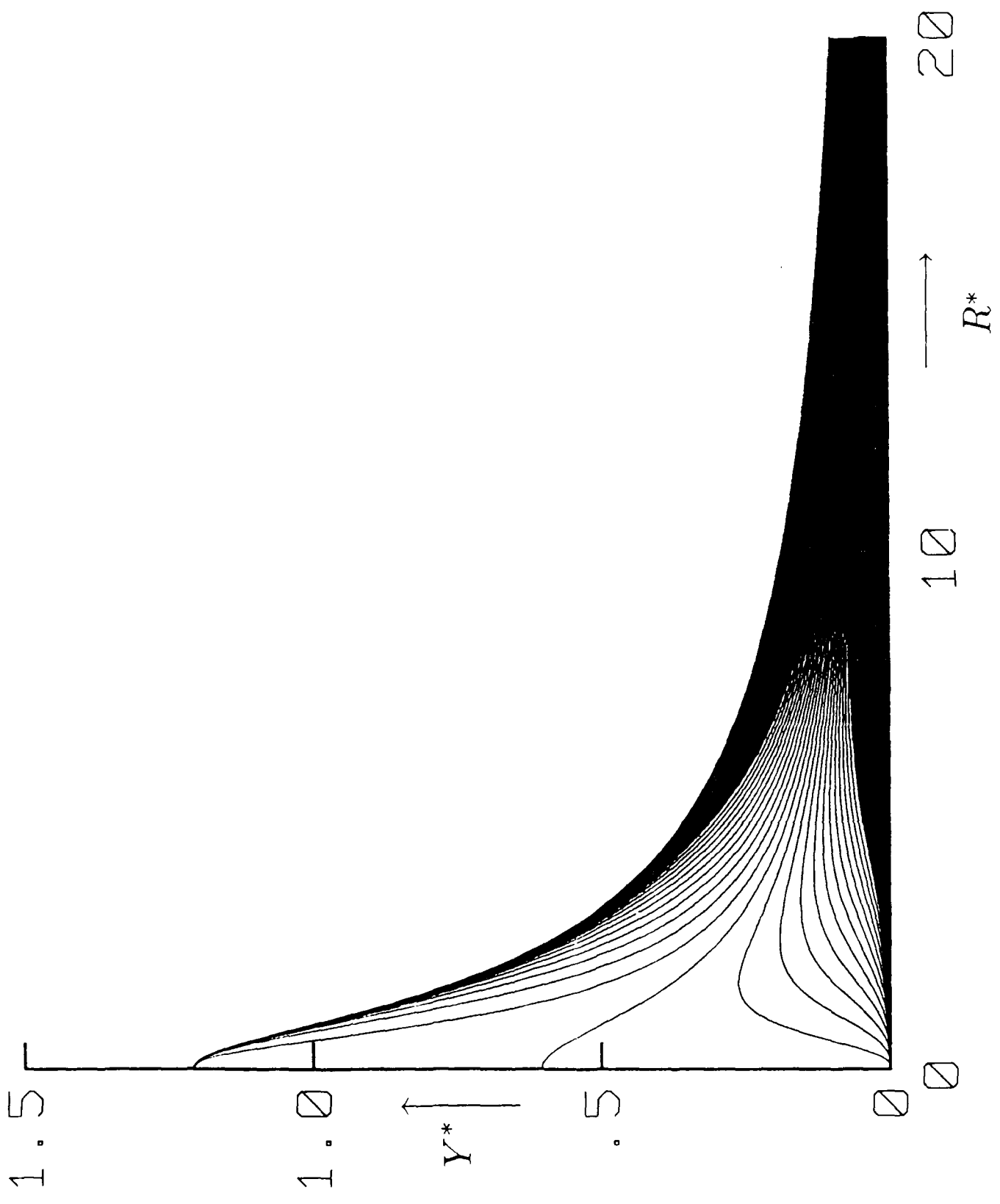
toward the wall



85



20



4

